Adaptive Cellular Layout in Self-Organizing Networks using Active Antenna Systems

von
M.Sc. Dereje Woldemedhin Kifle
geboren am 05.12.1983 in Addis Ababa

Acknowledgments

I would like to take a moment to express my sincere gratitude to everyone who supported me along the journey of my PhD.

First and foremost, my deepest gratitude goes to Prof. Dr.-Ing. Anja Klein for the opportunity I got to carry out this PhD research under her supervision. Her guidance, encouragement and support during the work was indispensable. I also express my warmest gratitude and respect for Dr.-Ing. Bernhard Wegmann and Dr.-Ing. Ingo Viering for their continuous support, guidance and valuable advice as well as for being inspirational through the course of the PhD. Their guidance in all the time of the work greatly helped me in shaping my research direction. Without them, this thesis could have hardly been completed. I could not have imagined having a better supervisors and mentor for my PhD. It was an amazing experience working with you. Besides, I would like to thank my thesis examiner Prof. Dr.-Ing. Thomas Kürner for generously taking time and providing insightful and valuable comments toward improving the PhD thesis.

I would like to send a special thanks to the research and innovation center of Nokia Bell Labs located in Munich for setting up this research in collaboration with the communication engineering Lab of Technical University of Darmstadt by funding my PhD program. In particular, my sincere thanks goes to Dr. Simone Redana, head of the Mobile Systems Architecture research group, and Peter Merz, head of the end-to-end Mobile network solutions, who offered me the opportunity to join their research team. It was a unique opportunity that helped me in defining my career path.

I owe a deep gratitude to colleagues at Nokia in Munich especially to Andreas Lobinger and Rüdiger Halfmann for their great support on the research tools and providing essential data, without that, it would not have been possible to conduct this research. It is also a pleasure to thank all other fellow PhD colleagues at Nokia for the great companion and for all the fun time we have had during the period of the PhD.

I am much grateful for having such friends and families: Ermias Asrat & Helen, Fasil Tessema and Tewodros Asmamaw, Bezunesh Alemu, Habtamu Yesigat& Azeb, Dr. Asdesach zena & Tizta, Dr. Amsalu and his family, Dr. Burcu Barla, Stephan, Dr. Ömer Bulakci, Anna, Dr. Abdallah Saleh, Dr. Ahmad Awada and his family, Girmaw Tadesse and Biruk Demissie who have been there together along the way by sharing feelings and celebrating each accomplishment. In particular, to Zenebework Zerefa and

Kurzfassung

Die rasch wachsende Nachfrage nach Mobilfunkkapazität stellt die Mobilfunkindustrie vor immer neue Herausforderungen und verlangt nach neuen Strategien hinsichtlich des Netzausbaus. Dabei gilt es gerade, das sowohl zeitlich wie auch räumlich sehr schwankende Verkehrsaufkommen in effizienter Weise zu bewältigen. Traditionell wird für Bereiche mit höherem Kapazitätsbedarf, als Maßnahme eine Verdichtung der zellularen Struktur in heterogener Weise vorgesehen. Dabei werden sogenannte Pico-Zellen oder "small cells" in eine Makrozelle eingebettet und erreicht so durch die dichtere räumliche Wiederverwendung der Funkressourcen eine Erhöhung der Netzkapazität. Die Funknetzplanung bedient sich dabei der "busy hour" Regel, d. h. man stellt so viele Funkressourcen bzw. so viele kleine Zellen an den entsprechenden Standorten auf, dass es in der "Stunde der höchsten Verkehrslast" nicht zu Engpässen kommt. Diese Überversorgungsstrategie ist jedoch nicht besonders effizient, da zu einem großen Teil der Betriebszeit viele Netzwerkressourcen ungenutzt bleiben, was für den Netzbetreiber hohe Investitionen in die Infrastruktur (CAPEX) sowie hohe Betriebskosten (OPEX) bedeutet. Wünschenswert wäre deshalb ein Netzwerk, dessen Kapazität sich flexibel an die dynamische Verkehrssituation anpasst und die teure "busy hour" Strategie mit maximaler und fixer Ressourcenbereitstellung umgeht.

Neue revolutionäre Basisstationsantennentechnologien, bei der jedes Antennenelement mit einer aktiven Komponente wie Verstärker kombiniert ist, aktive Antennensysteme (AAS) genannt, verspricht die nötige Flexibilität und gewünschte dynamische Bereitstellungsstrategie für die adaptive Kapazitätsversorgung. Durch die direkte Phasen- und Amplitudensteuerung jedes einzelnen Antennenelements unterstützt das AAS eine deutlich verbesserte Beamforming-Funktionalität, die eine neue Art der "Sektorisierung" mit dynamischer Zellverdichtung ermöglicht. Wird in einer konventionellen Zelle eine Überlastsituation festgestellt, lässt sich die Strahlungskeule der konventionellen Zelle in zwei neue, kleinere Beams aufteilen, welche als neue Zellen bzw. Sektoren dienen. Durch die weitere Zellaufteilung (Sektorisierung) werden die Funkressourcen in diesem Bereich durch die räumliche Wiederverwendung des Frequenzspektrums verdoppelt und so die Verkehrslast auf die beiden neuen Zellen verteilt.

Diese Art der dynamischen Gestaltung der zellularen Netzstruktur mittels AAS birgt aber auch einige Herausforderungen. Durch die zusätzlichen Zellen ergeben sich mehr Zellgrenzbereiche und somit zusätzlich Areale mit erhöhter Interzellinterferenz, die der erwarteten Systemkapazitätssteigerung durch Zellverdichtung entgegenwirken. Außerdem gilt es den sich zeitlich und räumlich ändernden Verkehr im Blick zu haben, um gezielt eine Zellverdichtung mittels Sektorisierung vornehmen zu können. Um dieser

Aufgabe gerecht zu werden und um mit dieser Methode eine Steigerung der System-leistung und Optimierung der Dienstgüte beim Endnutzer erreichen zu können, ist ein automatischer, sich selbstorganisierender Management- und Konfigurationsmechanis-mus notwendig. Mit einer solchen dynamischen Anpassung der Zellstruktur geht die Selbstorganisation der Netze in eine neue Dimension, da das zelluläre Netz inklusive der Funkausbreitungsbedingungen nicht mehr als stationär angesehen werden kann. Um dies gewährleisten und voll ausnutzen zu können, werden zuverlässige und realistische Ausbreitungsmodelle benötigt, die die Abhängigkeit der Funkkanalcharakteristik von der Veränderung der Strahlungskeule abbilden. Dies sowie die komplexen Beziehungen verschiedener Systemparameter bedingen ein umfassendes systemtheoretisches Model der AAS-basierten Sektorisierung, um detaillierte Untersuchungen und eine präzise Auswertung der erwarteten Systemleistungsgewinne zu ermöglichen.

Ein wesentlicher Aspekt der Arbeit ist die Entwicklung eines geeigneten SON Algo-rithmus, der die gesamte Prozedur der AAS-basierten Sektorisierung automatisiert. Er steuert die Aktivierung und Deaktivierung von Strahlungskeulen, welche die Zellen bzw. Sektoren repräsentieren, und ermöglicht somit die verkehrsadaptive Anpas-sung des sektorbasierten Zellaufbaus mittels Zellteilung und Verschmelzung. Um die dynamischen Kapazitätsanforderungen durch variierende räumliche Nutzerverteilun-gen effektiv bereitstellen zu können, überwacht der neu entwickelte SON Algorith-mus sowohl die Last wie auch die räumliche Verteilung des Datenverkehrs in einer Funkzelle und adaptiert die darunterliegende Funkzellenabdeckung durch autonome Sektorisierung in der horizontalen oder vertikalen Ebene. Der Algorithmus verwendet verschiedene Prozeduren, die von Echtzeitnetzdaten abhängen, welche wiederum aus Signalmessberichten der Endnutzerterminals gewonnen werden. Eine mögliche Ver-schlechterung der Systemleistung verhindert der Algorithmus dadurch, dass vor der Durchführung der Sektorisierung sichergestellt wird, dass die Gleichkanalinterferenz keinen negativen Einfluss auf die Nutzer hat. Dazu wurde eine Leistungsmetrik ent-wickelt, die den negativen Einfluss der Gleichkanalinterferenz den erwarteten Gewinnen durch die Zellverdichtung mit zusätzlichen Funkressourcen gegenüberstellt. Um das Interzellinterferenzproblem, das durch die AAS-basierte Sektorisierung an den neuen Zellgrenzen auftritt zu mildern, wird in dieser Arbeit eine weitere neue Methode ent-wickelt, welche die Datenübertragung in den benachbarten Funkzellen mit Hilfe des Prinzips der Übertragungsstummschaltung koordiniert. Um sicherzustellen, dass die partielle Stummschaltung von Ressourcen die Gesamtsystemleistung nicht verringert, wird der SON Algorithmus dahingehend erweitert, dass auch diese Methode in opti-maler Weise genutzt wird.

Um die Zellteilung mittels Änderung der Strahlungskeule richtig charakterisieren zu können, wurde ein neues erweitertes Funkausbreitungsmodell entwickelt, das ein nei-

gungsspezifisches Abschattungsmodel (Shadowing) enthält. Entgegen der bestehenden Shadowing-Modelle, welche eine stationäre neigungsunabhängige Ausbreitungseigenschaft in der Elevationsebene haben, wird nun ein neigungsabhängiges Shadowing Modell vorgeschlagen, das zudem in der Lage ist, die Variabilität des Funkkanals abhängig von der Höhe der Endnutzer statistisch zu charakterisieren. Für die simulationsbasierte Realisierung der unterschiedlichen Varianten der AAS-basierten Sektorisierung, d.h. die schnelle Änderung des Zelllayouts mittels dynamischer Konfiguration der AAS-Parameter, werden vereinfachte 3D-Beamforming Modelle und synthetische Strahlungsmuster entwickelt. Die horizontale und vertikale Sektorisierung sind die beiden Formen der AAS-basierten zellulären Netzlayoutänderung, die in dieser Arbeit betrachtet werden. Der ursprünglich Sektor wird durch Generierung von zwei neuen schmaleren Strahlungskeulen in zwei neue Sektoren aufgespalten, die von einem einzelnen AAS gleichzeitig erzeugt werden, was sowohl in der horizontalen wie auch in der vertikalen Domäne möglich ist.

Die Leistungsfähigkeit des entwickelten AAS-basierten dynamischen Zellverdichtungskonzepts und dessen SON-gesteuerte automatische Kontrolle wird mittels System-Level-Simulationen untersucht. Als Testszenarien werden makrozellulare Netzmodelle mit Basisstationen verwendet, die mit der Long Term Evolution-Advanced (LTE-A) Technologie betrieben werden. Die Simulationsergebnisse zeigen, dass der entwickelte SON Mechanismus das Netzlayout auf die unterschiedlichen Bedingungen anpassen kann, und sie machen deutlich, wann und wo die Sektorisierung Gewinn bringt bzw. sie sich nachteilig auf den Endnutzer auswirkt. Ebenfalls wurde die Wechselwirkung des neuen SON Mechanismus für die adaptive Zelladaptation mit bereits existierenden SON Funktionen, wie z.B. Mobility Robustness Optimization (MRO) erforscht, da diese bislang von einem stationären Zelllayout ausgingen. Die Untersuchungen ergaben, dass es einer Koordinierung der beiden SON Funktionalitäten bedarf, d.h. zwischen dem SON Mechanismus für die AAS-basierte Sektorisierung und dem MRO Betrieb, um unvorhersehbare Leistungseinbußen zu vermeiden und ein reibungsloses Endnutzererlebnis zu gewährleisten.

Die technischen Konzepte welche im Rahmen dieser Arbeit entwickelt wurden, sind außerdem in das SON Arbeitspaket für AAS-basierte Netzadaption innerhalb der Radio Access Network (RAN) Arbeitsgruppe 3 des 3rd Generation Partnership Project (3GPP) eingeflossen.

Abstract

The rapidly growing demand of capacity by wireless services is challenging the mobile industry with a need of new deployment strategies. Besides, the nature of the spatial and temporal distribution of user traffic has become heterogeneous and fluctuating intermittently. Those challenges are currently tackled by network densification and tighter spatial reuse of radio resources by introducing a heterogeneous deployment of small cells embedded in a macro cell layout. Since user traffic is varying both spatially and temporally, a so called busy hour planning is typically applied where enough small cells are deployed at the corresponding locations to meet the expected capacity demand. This deployment strategy, however, is inefficient as it may leave plenty of network resources under-utilized during non-busy hour, i.e., most of the operation time. Such over-provisioning strategy incurs high capital investment on infrastructure (CAPEX) as well as operating cost (OPEX) for operators. Therefore, optimal would be a network with flexible capacity accommodation by following the dynamics of the traffic situation and evading the inefficiencies and the high cost of the fixed deployment approach.

The advent of a revolutionizing base station antenna technology called Active Antenna Systems (AAS) is promising to deliver the required flexibility and dynamic deployment solution desired for adaptive capacity provisioning. Having the active radio frequency (RF) components integrated with the radiating elements, AAS supports advanced beamforming features. With AAS-equipped base station, multiple cell-specific beams can be simultaneously created to densify the cell layout by means of an enhanced form of sectorization. The radiation pattern of each cell-beam can be dynamically adjusted so that a conventional cell, for instance, can be split into two distinct cells, if a high traffic concentration is detected. The traffic in such an area is shared among the new cells and by spatially reusing the frequency spectrum, the cell-splitting (sectorization) doubles the total available radio resources at the cost of an increased co-channel interference between the cells.

Despite the AAS capability, the realization of flexible sectorization for dynamic cell layout adaptation poses several challenges. One of the challenges is that the expected performance gain from cell densification can be offset by the ensuing co-channel interference in the system. It is also obvious that a self-organized autonomous management and configuration is needed, if cell deployment must follow the variation of the user traffic over time and space by means of a sectorization procedure. The automated mechanism is desired to enhance the system performance and optimize the user experience by automatically controlling the sectorization process. With such a dynamic adaptation scheme, the self-organizing network (SON) facilities are getting a new dimension

in terms of controlling the flexible cell layout changes as the environment including the radio propagation characteristics cannot be assumed stationary any longer. To fully exploit the flexible sectorization feature in three-dimensional space, reliable and realistic propagation models are required which are able to incorporate the dependency of the radio channel characteristics in the elevation domain. Analysis of the complex relationship among various system parameters entails a comprehensive model that properly describes the AAS-sectorization for conducting detailed investigation and carrying out precise evaluation of the ensuing system performance.

A novel SON algorithm that automates the AAS-sectorization procedure is developed. The algorithm controls the activation/deactivation of cell-beams enabling the sectorization based cell layout adjustment adaptively. In order to effectively meet the dynamically varying network capacity demand that varies according to the spatial user distribution, the developed SON algorithm monitors the load of the cell, the spatial traffic concentrations and adapts the underlying cell coverage layout by autonomously executing the sectorization either in the horizontal or vertical plane. The SON algorithm specifies various procedures which rely on real time network information collected using actual signal measurement reports from users. The particular capability of the algorithm is evading unforeseen system performance degradation by properly executing the sectorization not only where in the network and when it is needed, but also only if the ensuing co-channel interference does not have adverse impact on the user experience. To guarantee the optimality of the network performance after sectorization, a performance metric that takes both the expectable gain from radio resource and impact of the co-channel interference into account is developed. In order to combat the severity of the inter-cell interference problem that arises with AAS-sectorization between the co-channel operated cells, an interference mitigation scheme is developed in this thesis. The proposed scheme coordinates the data transmission between the co-sited cells by the transmission muting principle. To ensure that the transmission muting is not degrading the overall system performance by blanking more data transmission, a new SON algorithm that controls the optimal usage the proposed scheme is developed.

To appropriately characterize the spatial separation of the cell beams being activated with sectorization, a novel propagation shadowing model that incorporates elevation tilt parameter is developed. The new model addresses the deficiencies of the existing tilt-independent shadowing model which inherently assumes a stationary propagation characteristics in the elevation domain. The tilt-dependent shadowing model is able to statistically characterize the elevation channel variability with respect to the tilt configuration settings. Simplified 3D beamforming models and beam pattern synthesis approaches required for fast cell layout adaptation and dynamic configuration of the AAS parameters are developed for the realization of various forms of AAS-based

sectorization. Horizontal and vertical sectorization are the two forms of AAS-based sectorization considered in this thesis where two beams are simultaneously created from a single AAS to split the underlying coverage layout in horizontal or vertical domain, respectively.

The performance of the developed theoretical AAS-sectorization concepts and models are examined by means of system level simulations considering the Long Term Evolution-Advanced (LTE-A) macro-site deployment within exemplifying scenarios. Simulation results have demonstrated that the SON mechanism is able to follow the different conditions when and where the sectorization delivers superior performance or adversely affects the user experience. Impacts on the performance of existing SON operations, like Mobility Robustness Optimization (MRO), which are relying on stationary cell layout conditions have been studied. Further investigations are carried out in combination with the cell layout changes triggered by the dynamic AAS-based sectorization. The observed results have confirmed that proper coordination is needed between the SON scheme developed for AAS sectorization and the MRO operation to evade unforeseen performance degradation and to ensure a seamless user experience.

The technical concepts developed in this thesis further have impacted the 3rd Generation Partnership Project (3GPP) SON for AAS Work Item (WI) discussed in the Radio Access Network (RAN)-3 Work Group (WG). In particular, the observed study results dealing with the interworking of the existing SON features and AAS sectorization have been noted in the standardization work.

Contents

Chapter 1

Introduction

1.1 Deployment Trends in Self-Organizing Cellular Networks

Cellular communication system has been going through a dramatic technological evolution in the past decades. Driven by the rapidly growing data demand and, variety of service quality and design requirements, different cellular network deployment strategies are being adopted. A macro cell coverage which is served by a high power transmitting base station antenna is employed to provision ubiquitous service coverage over a wide area. Initial macro base station site planing and network dimensioning are typically carried out to handle a busy hour traffic. Further tuning of different network parameters is performed to a provide the desired network coverage and to ensure the service quality targets [Hu16]. In practice, the number of network nodes and the site deployment pattern are highly dependent on the clutter type of the propagation environment and the spatial distribution of the traffic. For example, denser network deployment is adopted in urban areas than in sub-urban or rural environment.

Accommodating the influx of the data traffic and addressing the requested capacity are the key challenges of the mobile industry driving the evolution of various deployment strategies. Those challenges are currently tackled by denser network configuration and tighter spatial reuse of radio resources utilizing heterogeneous deployment of small cells embedded in a macro cell layout [HQ13]. To cope with the rapidly growing capacity demand, enhancing network capacity with efficient resource utilization has become the utmost strategy in cellular system design.

Cell sectorization which is realized by using directional antenna also called sector-antenna is extensively used to increase spectrum utilization efficiency by subdividing (splitting) a macro cell into smaller cells [Sta01, KC09, Hu16, Zet04]. The sectorization technique substantially boosts cellular capacity via space division multiplexing (SDM) scheme where frequency spectrum is heavily reused over the sub-divided cells [KC09, HOD+10, Cha92]. In the traditional sectorization approach, each cell is served by a fixed beam generated from a dedicated sector-antenna and the realization of a more densified cell layout is enabled by increasing the order of sectorization which needs a higher number sector-antennas to be deployed per site [Hu16]. The typical sector-antenna widely deployed in today's network is referred as passive antenna system where

vertically stacked antenna elements (array column) and the remote radio head (RRH) are decoupled in the architecture [Aut16, Ame11]. The conventional cell sectorization strategy widely deployed is a tri-sector cell layout where three co-sited sector-antennas are arranged 120° apart in the horizontal direction. It is also a common practice to further increase the number of cells in the horizontal direction within the base station serving area by using higher order sectorization, i.e. six-, or tweleve-order sectorizaiton. The order of sectorizaiton, in this thesis context, refers to the number of cells per site and the term higher order sectorizatation is used to describe when the number of cells per site is more than three [Hu16, Zet04].

Despite the increase in the amount available total radio resource, higher order sectorization does not proportionally multiply capacity as cell overlap increases and the ensuing co-channel interference becomes severe thereby limiting the system performance [Hu16, WLSSH99, Zet04, Sta01]. In addition, the interference impact can be exacerbated by the spatial distribution of the user as high traffic concentration around the cell border is detrimental. Detailed investigation results presented in [WLSSH99] demonstrated that cell sectorization can effectively increase system capacity if the azimuth beam pattern is carefully designed to mitigate the interference leakage between co-sited cells. The traditional sectorizaiton method yields cells having equal coverage width, hence, it is ideally suited for a uniform load distribution [NPK94]. Under highly nonuniform spatial distribution of the user load, however, the anticipated gain might not be achieved from such fixed sectorizaiton approach owing to the load imbalance in the system [NPK94, Cha92]. As indicated in [Zet04], the azimuth beam width of the employed sector-antenna is determining the shape of the cell layout and the coverage overlapping between the intra-site cells. Due to the fact that commercially available base station antennas are usually manufactured with a fixed beam width [Hu16, JMB+16], the flexibility in controlling the shape of cell layout is highly limited. As a consequence, conventional cell layout remains fixed after sectorization having static borders between the neighboring cells [LC10, Ame11]. Adapting the cell coverage layout and optimizing the system capacity requires to change the characteristics of the cell beam as desired [SAP99].

Base station equipped with multiple columns antenna array and advanced signal processing are promising to significantly enhance system capacity, compared to the single column antenna array transmission, by further exploiting the spatial dimension using a beamforming technique. With beamforming, a dedicated beam having a desirable beam characteristics can be formed [SAP99]. Even though the spatial domain is three dimensional in nature, the existing base station passive antenna supports beamforming only in the horizontal dimension, i.e. two-dimensional (2D). By reusing the spectral resources over several dedicated horizontal cell-specific beams, transmissions for multiple

users can be spatially multiplexed. However, for users spatially distributed at different elevation angle, passive base station antenna can not exploit the vertical spatial separation to multiplex transmission as beamforming is not supported in the elevation dimension. Passive base station antenna rather has only a single beam in the vertical plane whose boresight is adjusted by varying tilt configuration. Antenna tilt adaptation technique can be used to effectively control the shape the cell coverage and to reduce interference leakage to adjacent cells [XSKO03]. However, the supported flexibility in steering the beam direction in the elevation dimension is limited to a small range of antenna tilt settings which is supported by mechanical and remote electrical tilting (RET) operation [Aut16, Ame11].

Since the nature of real traffic distribution in cellular network is getting highly variable over time and space, it is challenging the traditional cellular deployment paradigm where the cell layout and system configurations remain fixed and assumed stationary. Addressing the variable capacity demand by following the dynamics of the traffic situation in a cost effective manner requires a flexible deployment solution that can provision capacity in adaptive manner. Moreover, the intermittent spatial and temporal variation of the traffic pattern makes system performance monitoring and related network parameter tuning operations more complex to be handled by manual process entailing an automated operation.

The co-existence of various cellular radio access technologies (RATs) and the heterogeneity of the deployment are increasing the complexity of cellular network making it impractical to manage the operation by manual intervention [HSS12]. Moreover, since the number of network parameters and configurations which must be monitored in multiple RAT network are significantly large, the manual operation will be highly error-prone and tedious incurring operators high operating cost (OPEX). To address those challenges, a Self-Organizing Network (SON) feature that can support automated network operation, configuration and optimization functionalities have been introduced [SOC08, HSS12]. In SON-enabled network, various types of network operations can be automated and system performance monitoring can be performed online based on reliable measurement statistics collected from the network itself.

1.2   Active Antenna Systems

Base station antenna technology has been evolving over years in order to support various cellular network deployment strategies. The increasing demand in capacity and the proliferation of new cellular access technologies are challenging the mobile industry

by requiring a higher system bandwidth and support for new frequency bands. Those challenges are driving the integration of advanced signal processing techniques and more functionality into the base station antenna architecture.

In passive base station antenna architecture, the radio functionality resides in the remote radio head (RRH) unit and is separated from the antenna array, and the signal at each column of the antenna array is controlled by only one active transceiver (TRX) [Ste09]. A typical passive base station antenna diagram comprising phase shifters, RRH, the RET module and connection with the base band unit (BBU) is illustrated in Figure 1.1(a). Even though beamforming is possible in such antenna configuration, it is not highly flexible as it is performed in RF-domain using analogue phase shifters [Ste09].
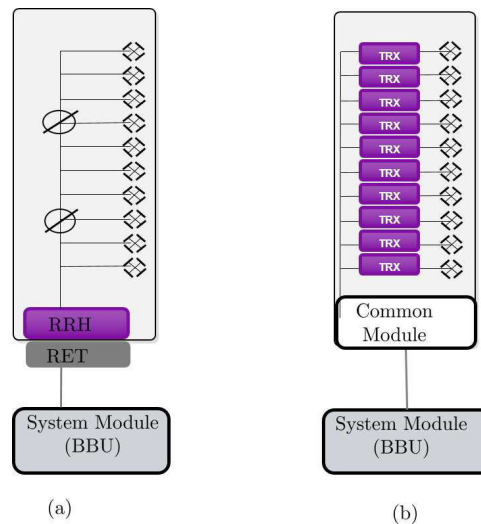
Figure 1.1. (a) Passive antenna, (b) Active Antenna Systems [Net]

Active Antenna Systems (AAS) is a revolutionized base station platform wherein the radio functionality is distributed across the antenna array. In AAS, each radiating element of the antenna array is connected to a separate active transceiver to allow independent base band control of the phase and amplitude of transmit/receive signal. Figure 1.1(b) shows a single column AAS configuration consisting of TRX and common module within the antenna radome. Having multiple distributed transceivers connected to the array elements enables to perform advanced beamforming in digital domain providing high flexibility in terms of controlling the shape and orientation of the generated beam. The 3D beamforming capability is the key components of the features supported by AAS. Applying 3D beamforming, multiple beams can be formed from the same AAS and the radiation pattern of each beam can be independently controlled both in the azimuth and elevation domain. Thus, with AAS-enabled cellular deployment, cell sectorization can be carried out flexibly in the vertical and horizontal

plane. The sectorization flexibility and the number of separate cell beams that can be simultaneously created depends on the antenna aperture and number of antenna array elements.

1.3   State of the Art

This section discusses the state of the art of automated cell sectorization strategies and adaptive cell layout changes. Previous works on adaptive sectorization concept and related research activities considering the legacy passive anetenna base station are presented first. Afterwards, available literatures on the flexible sectorization approach enabled by a more advanced and emerging base station antenna technology are explored.

In a non-uniform spatial user distribution scenario, automated cell sectorization can control the cell size and adapt the cell layout according to the distribution of users in the underlying coverage. With the conventional multi-antenna base station, this can particularly be achieved by switching different cell beams. In fact, adaptive sectorization has become an interesting research topic for many years driven by the advancement in spatial-time signal processing. The study on the feasibility of switched-beam smart antennas for cellular radio systems and related performance analysis are shown in [GMV01]. Various studies in [HW16, HSA98, GMV01, SY01] examine the performance of adaptive sectorization enabled by switched beam forming. The sectorization investigations discussed in these literatures relies on the 2D beamforming scheme carried out only in the horizontal dimension limiting the sectorization capability to the horizontal plane. In [LOp02], an adaptive sectorization algorithm is proposed to automate the deployment of horizontally sectorized cells. However, the algorithm focuses rather only on resizing the cell coverages within the conventional three-sector site configuration than dynamically switching between multiple cell-beams.

An emerging more advanced base station antenna platform which has the beamforming capability both in the horizontal and vertical domain is the enabler technology for the adaptive cell layout mechanisms this thesis focuses on. Such antenna promises to deliver a spatial multiplexing capability in the elevation domain supporting a new dimension for the cell sectorization with additional flexibility of adapting the cell layout. Since the sectorization in the vertical domain is a relatively new concept, the available literatures are very limited. Moreover, to the knowledge of the author, a flexible and automated cell sectorization mechanisms (horizontal and vertical) are not well investigated in the context of self-organizing networks. The available literatures known by the authors

which focus on fixed and SON based vertical sectorization aspects are summarized as follows.

In [YHH09], a system level performance analysis for vertical sectorization is carried out for LTE networks considering advanced base station antenna deployment. The work mainly focuses on the evaluation of the upper bound throughput performance study and the impact analysis of such novel sectorization strategy in a macro-cell deployment scenario for various antenna parameter configuration settings. In addition, However, only the non-realistic uniform user distribution assumption is considered in the simulation model. Moreover, despite being spatially separated in the elevation domain, the radio channel with respect to each vertical cell beam is assumed to be fully correlated and the existing two-dimensional propagation model is directly adopted. However, these assumptions might not be valid while considering a realistic scenario, hence, needs to be further examined.

The work in [FWZ+12] studies impact of vertical sectorizaiton on system capacity and coverage performance by incorporating a novel resource scheduling scheme for a uniformly distributed user scenario.

Furthermore, the performance of vertical sectorizaiton in real LTE network is evaluated by conducting a field trial test in [YZXZ14]. The paper does not only show the favorable system gains from the vertical sectorization, but also highlighted that the inter-cell interference issue is a critical factor in determining the system performance. In order to improve user experience, the paper forwards some practical suggestions to mitigate the impact of the resulting inter-cell interference.

A self-optimizing strategy for vertical sectorization have been explored within a SE-MAFOUR (self-Management for unified heterogeneous radio access networks) project where different SON functions and integrated SON management system are studied [sem17]. The study provides a SON controller for vertical sectorization by flexibly partitioning the available bandwidth and transmit power between the vertical cells [AZA15a]. However, the considered approach does not guarantee maximum frequency utilization as the spectrum is not fully reused all the time. Besides, changing the outer cell transmit power may undesirably shift the cell border resulting in unintended load imbalance between cells whose impact on the system performance is not analyzed. The study develops the SON framework based on realistic deployment scenario, however, the radio propagation conditions for both vertical beams are assumed to be identical in some cases when analyzing 3GPP based vertical sectorization scenarios [AZA15b]. In addition, the algorithm decision criteria do not explicitly deal with the impacts of the inter-cell interference for users when traffic hotpots are appearing

on the coverage area close to the new cells' borders. Therefore, for a realistic and appropriate SON decision, those issues needs to be properly taken into account.

1.4 Open Issues

Since AAS is an advanced and emerging base station antenna platform, the deployment options supported, the dynamic sectorization techniques and flexible cell layout design concepts are new topics and detail theoretical and technical analysis are not available in literatures. Hence, the thesis work outlines the open issues which are summarized as follows.

1. How to design a suitable radiation pattern and properly adapt the orientation of cell-specific beam to carry out the desired form of sectorization?

2. are there deficiencies with the existing two-dimensional propagation model in characterizing the radio channel to exploit the elevation beamforming capability of AAS? How does the elevation channel variation for various tilt configuration can be characterized using propagation shadowing model?

3. How to model enhanced AAS-based sectorization in vertical dimension, vertical sectorization? how to describe the complex relationship among various related system parameters?

4. How to combat the ensuing inter-cell interference challenge within the co-channel operated intra-site cells after AAS sectorization?

5. How to model enhanced AAS-based sectorization in horizontal dimension, horizontal sectorization? how to describe the complex relationship among various related system parameters?

6. How to design and model a Self-Organizing Network (SON) mechanism in order to automate the AAS-based sectorizaiton procedure in a self-organized manner and to provide an adaptive functionalities to support dynamic cell layout changes?

7. what are the impacts of the cell layout change introduced by AAS-sectorization on the existing automated network operations? does further enhancement required on the standardized SON use cases?

1.5 Contributions and Outline of the Thesis

This section provides the summary of the contributions of the thesis work which address the open issues described in Section 1.4.

The details of the system model and the description of the scenarios considered for the purpose of simulative investigation are presented in Chapter 2. This chapter answers open issue 1. In this chapter, the beamforming model and beam pattern design approaches required for fast cell layout adaptation and dynamic reconfiguration of the AAS parameters are provided. Moroever, the beam pattern designs developed to realize various forms of AAS-based sectorization are presented together with the design criteria including essential aspects specific to the different sectorization types considered in the thesis, i.e, conventional, horizontal and vertical sectorization.

In Chapter 3, a new propagation shadowing model is developed motivated by the deficiencies of the existing tilt-independent model addressing open issue 2 [KWVK13]. The current shadowing model is derived only to include a two dimensional propagation scatter behavior, mainly, in the azimuth direction, hence, assumes a stationary propagation characteristics in the elevation domain [Sin15, M.91]. The shadowing model developed in this thesis introduces elevation tilt angle parameter to capture the effect of the relative clutter variation that can be experienced while the elevation orientation of the cell beam is altered in a scatter-rich urban environment [KGW+14]. To ascertain tilt dependency of the shadowing process, a detailed investigation is carried out by means of statistical analysis of a ray-tracing (RT) based predicted radio propagation data for a realistic 3D urban environment. Despite being derived from specific scenario configuration, the irregular site locations within the considered 3D scenario are adopted from real network planning data. Hence, the employed RT propagation prediction are able to reflect various clutter experience of real-world propagation effects. The tilt-dependent model employs statistical correlation predictor function to approximate the variation of the random shadowing effect with respect to different tilt configuration. Owing to the diversified nature of the clutter considered in the scenario, the parameter values introduced in the developed model can be seen as valid and applicable to a wide range of case scenarios. Throughout the thesis, the tilt dependency of the propagation shadowing effect is accounted while studying the performance of AAS sectorization.

The overall system model developed for the AAS-based sectorization carried out in the vertical plane, i.e., vertical sectorization (VS), is presented in Chapter 4 answering open issue 3. In VS, two beams which are spatially separated in a vertical dimension using different elevation tilt configuration are created in order to split the conventional cell

vertically into two [KWVK14a, KWVK14b]. The presented model explains the factors determining the performance of VS and describes the complex relationship among various related system parameters. This provides a basis for the automated operation designed to control the corresponding sectorization procedure. Moreover, thorough analysis for the inter-cell interference problem that countermands the performance of AAS sectorization, particularly, in VS is carried out. The chapter further addresses open issue 4 by developing an adaptive interference coordination technique to tackle the severe impact of the co-channel interference within the intra-site vertical cells to maximize the system performance [KFW$^+$15].

In Chapter 5, the system model developed for the AAS-based sectorization carried out in the horizontal plane, i.e., horizontal sectorization (HS) is presented separately addressing open issue 5. Since the HS procedure completely replaces the wide conventional cell coverage with two narrow cells, it may introduce undesirable cell layout change considerably altering the border between the neighboring cells. Hence, additional performance impact analysis particularly focusing on the coverage size, interference issue and throughput performance are conducted.

Chapter 6 presents a novel SON mechanism developed to automate the AAS-sectorization enabling execution of the cell layout adaptation procedure dynamic. This chapter answers open issue 6. The SON framework for controlling the automated sectorization mechanism is developed by integrating the AAS-sectorization models described in Chapter 4 and 5. The framework specifies different procedures that relies on real time information collected using actual measurement reports from the network and defines analytical method for the evaluation of the system performance [KWVK16]. With the SON based automated AAS-sectorization, a controlled activation/deactivation of cell-beams enables to effectively meet dynamic network capacity demand by intelligently monitoring the spatial traffic concentrations and adapting the underlying cell coverage layout accordingly. The chapter, furthermore, presents the SON function developed to automate the developed adaptive interference-coordination mechanism, described in Chapter 4, with the context of SON.

In Chapter 7, the impacts of the cell layout change introduced by the automated sectorization is thoroughly investigated. This chapter answers open issue 7.The investigation mainly analyzes the impacts with respect to user mobility. Detail assessment have been carried out as well on the performance of the existing standardized automated Mobility Robustness Optimization (MRO) operation to identify any user Handover (HO) related problems and open issues that needs to be addressed to support the AAS-sectorization [KWVK15]. In this chapter, user mobility handling schemes and HO coordination strategies have been proposed to evade the abrupt connection failure

problems that can be experienced by both moving and stationary users while sector-
ization is executed. The proposed schemes and strategies address various open issues
highlighted by 3GPP in response to the request for a potential SON enhancements
that may be necessary to ensure interoperability within the existing features in Re-
lease (Rel.) 12 related to AAS-enabled deployments [3GP14b].

Chapter 2

System Model

2.1 Introduction

This chapter presents the system model and the description of the scenarios which are used to carry out an investigation on automated cell sectorization and adaptive cellular layout deployments.

A tri-sectorized macro cell layout is traditionally employed in system level simulations while investigating various system level aspects of a cellular network [3GP13a]. Accordingly, a cell is served by one of the three co-sited directional antennas using a fixed cell beam. As the traditional passive base station antenna supports a beamforming only in the horizontal domain, the study of conventional cell sectorizaiton is limited to the horizontal only [Hu16]. However, the cell sectorization strategies which this thesis deals with have got a new dimension by exploiting the elevation domain that has been omitted in the conventional approach. Therefore, the available system level simulation framework needs to be adapted to support the appropriate features that are required to carry out the investigation of such enhanced form of cell sectorization. The enabler technology that is considered in this thesis is an advanced base station antenna platform that supports a three-dimensional beamforming. This requires to have the description of the beam pattern designs and the basic design criteria that needs to be specified to achieve the desired particular type of sectorization.

Two types of cellular network scenarios are considered assuming the LTE-Advanced (LTE-A) macro-site deployment. The first type is the 3rd Generation Partnership Project (3GPP) defined generic and commonly used scenario which is described by a regular hexagonal cellular model [3GP13a]. This scenario, henceforth referred to as 3GPP-Scenario, is considered to develop the general framework and model for AAS-sectorization, and to perform baseline analysis of related system performance. The second one is a realistic scenario wherein a particular urban city area is modeled using a three dimensional topography map. In this scenario, a Ray-Tracing (RT) based propagation prediction model is utilized to characterize the corresponding propagation environment [God01], therefore, is referred to as RT-Scenario throughout the thesis. Since the ray-tracing model employed in the RT-Scenario inherently accounts various physical propagation phenomena, it captures and reflects the behavior of a real-world

propagation environment. Moreover, various studies in [EFL$^+$97, KGI$^+$99, CLW$^+$03] have demonstrated that ray-tracing prediction provides performance data comparable to field measurements. For this reason, the RT-Scenario is used as a validation platform where the developed AAS-sectorization model is applied for further system study and performance analysis.

This chapter is organized as follows. Details of the considered LTE-A network scenario and corresponding propagation models including path loss, shadowing and antenna radiation pattern are presented in Section 2.2. The beam pattern design approaches together with the description of the 3D beamforming techniques employed in the designing of the pattern suitable for the desired type of AAS-based sectorization are discussed in Section 2.3. The models for the average SINR and throughput performance of a user are presented in Section 2.4. The utilized traffic model and the applied radio resource allocation scheme are explained in Section 2.5. Section 2.6 introduces the definition for load and remaining available capacity of a serving cell. Section 2.7 provides the definitions of the performance evaluation metrics that are used through out the thesis.

2.2 Cellular Models of LTE-Advanced Network

2.2.1 3GPP Cellular Model

2.2.1.1 Regular Hexagonal Cellular Layout

In this section, the regular hexagonal cellular layout of the LTE-A network is presented as defined by the 3GPP.

The considered LTE-A network is comprised of sectorized sites where a sector-configuration refers to a physical partition of a coverage area served by a directional sector-antenna. The sites are deployed in a regular hexagonal grid where adjacent sites are separated by equal inter site distance (ISD) d_{ISD}. Each site has a base station (BS) equipped with AAS and in total there are N_{bs} BSs in the network. The index of a BS is $q \in \mathcal{Q} = \{1, 2, \ldots, N_{\text{bs}}\}$ and the position of each BS is described by a vector $\mathbf{P}_q$. The total number of AAS being supported by BS q is N_q and the index of each AAS is $a \in \mathcal{N}_{\text{a}} = \{1, 2 \ldots, N_{\text{a}}\}$ where N_{a} is the total number of AAS in the network, i.e. $N_{\text{a}} = \sum_{q \in \mathcal{Q}} N_q$. The typical tri-sectorized site and regular cell layout are illustrated in Figure 2.1 (a) where the index of each sector-antenna a is indicated.
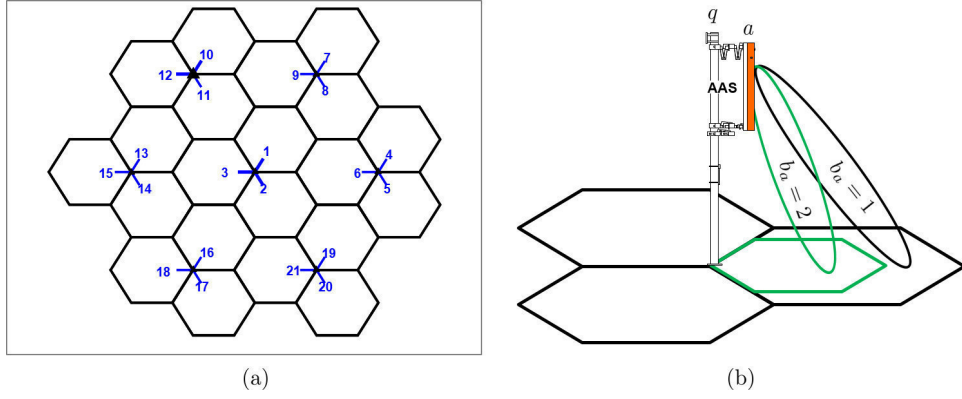
Figure 2.1. (a)Tri-sectorized regular hexagonal cell layout, (b) AAS-enabled BS Site

A cell is defined as a particular service-coverage area that is identified by a physical cell ID (PCI) in the network where the PCI is broadcast over the desired area using a cell-specific beam generated from the sector-antenna [HT12]. In the conventional macro-cell deployment, the sector-antenna supports a single cell called conventional-cell. However, since AAS provides the capability to flexibly and dynamically create more beams, the cell count served by a sector-antenna can be proportionally increased by further splitting the conventional-cell. This scheme is referred as Sectorization (Cell-splitting). Throughout the thesis, the term Sectorization-OFF is used to describe a situation where only one cell (conventional-cell) is active per sector-antenna whereas Sectorization-ON refers to when the conventional-cell is split into two distinct cells. In this thesis context, the maximum number of cells to be served by a sector-antenna is restricted to two. The Sectorization-OFF/ON status at sector-antenna a is designated by l_a such that $l_a = 0$ for Sectorization-OFF and $l_a = 1$ for Sectorization-ON. The index of the cell-specific beam at sector-antenna a is $b_a \in \{0, 1, 2\}$ where

$$b_a = \begin{cases} 0, & \text{for } l_a = 0 \\ 1, 2, & \text{for } l_a = 1. \end{cases} \tag{2.1}$$

One of the typical AAS-sectorization realized in vertical domain by activating two vertical beams is illustrated in Figure 2.1 (b).

The set of cells in the network is given by $\mathcal{C} = \{1, 2, \ldots, N_c\}$ where $N_c = 2 \cdot N_a$ is the total number of cells. The cell index $c \in \mathcal{C}$ is derived as

$$c = a + (b_a - 1) \cdot l_a \cdot N_a . \tag{2.2}$$

The corresponding index of the site and the sector-antenna to which cell c belongs is mapped by functions $Q(c)$ and $A(c)$ respectively, i.e. $q = Q(c)$ and $a = A(c)$. The location of UE u on the ground is given by a position vector $\mathbf{P}_u$. The association of

each UE u to its best serving cell is described by a connection function $s(u)$. The coverage of cell c designated by $\mathcal{A}_c$ is given by the set of all users associated to the cell, i.e. $\mathcal{A}_c = \{u|s(u) = c\}$. Furthermore, the total coverage area served by sector antenna a is described as the union of the coverage of all cells being served by the same antenna, i.e.

$$\mathcal{A}_a = \bigcup_{\forall c|A(c)=a} \mathcal{A}_c. \tag{2.3}$$

2.2.1.2   3GPP Radio Propagation Model

In this section, the path loss and the shadowing radio propagation models defined by 3GPP are presented. The discussion about the impact of fast fading is excluded from this section as it has a short-term effect and its impact averages out when observed over a long time scale. For this reason, it can be omitted while conducting a system level performance analysis over along period of time [Sin15, Gar07, Bau14, Tür07].

The path loss is the fraction of the loss of signal power in the coarse of propagation and it depends on the separation distance between the transmitter and receiver receiver. Given the distance between a BS site serving cell c and UE u by $d_{c,u} = |\mathbf{P}_{Q(c)} - \mathbf{P}_u|$ in km, path loss offset Υ in decibel (dB) scale and a path loss exponent ϱ, propagation path loss denoted by $L_\mathrm{p}(d_{c,u})$ is modeled as [3GP14a]

$$L_\mathrm{p}(d_{c,u}) = 10^{\frac{\Upsilon + 10 \cdot \varrho \cdot \log_{10}(d_{c,u})}{10}}. \tag{2.4}$$

Shadowing is a slow signal fading process which results from the presence of propagation obstacles causing a random fluctuation of signal power level in a long-term process [HZ02, M.91]. The value of the shadowing S_c^u experienced by a signal transmitted by cell c and received by UE u is modeled as a log-normally distributed random process, i.e. $S_c^u = 10^{\frac{\widehat{S_c^u}}{10}}$ where $\widehat{S_c^u}$ is the shadowing in dB scale and is normally distributed with mean μ_s and standard deviation σ_s. The hat sign ($\hat{}$) is used to indicate the variable is in dB. Shadow fading is determined by the propagation characteristics of the environment depending on where the UE is located with respect to the BS. Thus, $\widehat{S_c^u}$ is modeled as a combination of two independent random process components: the first component called UE-specific term denoted by χ_u represents the shadowing contribution due to the propagation obstacles in the vicinity of the UE and the second component χ_q called site-specific term used to include the effect of the obstacles surrounding the BS site serving cell c, i.e. $q = Q(c)$, [HZ02, M.91]. It has been confirmed in [M.91] that the shadowing values at u with respect to two different cells are not statistically

independent. The values exhibit some correlation due to the commonality of the UE-specific term. Therefore, it is essential to incorporate a non-zero cross-correlation coefficient in the shadowing model to properly include this correlation between any cell-pair [HZ02]. Given the cross-correlation coefficient by

$$\rho_{\mathrm{s}} = \frac{\mathrm{E}\left[\left(\widehat{S_{c1}^{u}} - \mu_{\mathrm{s}}\right) \cdot \left(\widehat{S_{c2}^{u}} - \mu_{\mathrm{s}}\right)\right]}{\sigma_{\mathrm{s}}^{2}}, \quad \text{for} \quad c1 \neq c2 \in \mathcal{C} \tag{2.5}$$

$$\rho_{\mathrm{s}} = 1 \quad \text{for} \quad Q(c1) = Q(c2), \tag{2.6}$$

the shadowing model is given by the sum of the UE and site-specific terms as

$$\widehat{S_{c}^{u}} = \sqrt{\rho_{\mathrm{s}}} \cdot \chi_{u} + \sqrt{\rho_{\mathrm{s}} - 1} \cdot \chi_{q} \tag{2.7}$$

where

$$\mathrm{E}[\chi_{u}] = \mathrm{E}[\chi_{q}] = 0, \tag{2.8}$$

$$\mathrm{Var}[\chi_{u}] = \mathrm{Var}[\chi_{q}] = \sigma_{\mathrm{s}}, \tag{2.9}$$

$$\mathrm{Cov}[\chi_{u}, \chi_{q}] = 0. \tag{2.10}$$

$\mathrm{E}[\cdot]$, $\mathrm{Var}[\cdot]$ and $\mathrm{Cov}[\cdot]$ are expectation, variance and covariance operators respectively.

Since shadowing is a slow fading process and its effect evolves over distance leading to a spatially correlated shadowing between any two adjacent UE locations [3GP13a]. The spatial correlation coefficient value drops over distance and is modeled with an exponential normalized autocorrelation function as

$$\mathcal{R}_{\mathrm{S}}(\Delta d) = e^{-\frac{\Delta d}{d_{\mathrm{cor}}}}, \tag{2.11}$$

where Δd is the distance between any two adjacent UE locations and d_{cor} is the de-correlation distance within which the autocorrelation falls to e^{-1} [CG03]. For $\Delta d \geq d_{\mathrm{cor}}$, shadowing values are loosely correlated and the shadowing values can be considered as statistically independent [M.91].

2.2.1.3 Antenna Gain and Beam Pattern

This section describes the antenna gain and 3D beam pattern model defined by 3GPP.

The gain of an antenna in any direction depends on how the antenna is radiating its energy using the directional beam serving a cell. Beam pattern describes the antenna radiation pattern using a three dimensional representation of the antenna gain compared to the maximum gain value. Given the boresight of the beam of cell c is tilted

by Θ_c in the elevation plane and steering to Φ_c in the azimuth plane, the antenna-gain in the direction of UE u is described by $G_c^u(\Phi_c, \Theta_c)$. The antenna gain is maximum in the boresight direction of the beam and is denoted by $G_c^{\max}$ expressed in dBi scale. $G_c^u(\Phi_c, \Theta_c)$ is computed from $G_c^{\max}$ by multiplying the value of the beam pattern which represents the relative gain reduction in the desired UE direction [Bal05]. The value of the beam pattern of cell c with respect to UE u located in the angular direction of ϕ_c^u and θ_c^u is described by $B_c(\Phi_c, \Theta_c, \phi_c^u, \theta_c^u)$. Thus, the general expression for $G_c^u(\Phi_c, \Theta_c)$ becomes

$$G_c^u(\Phi_c, \Theta_c) = 10^{\frac{G_c^{\max}}{10}} \cdot |B_c(\Phi_c, \Theta_c, \phi_c^u, \theta_c^u)|^2, \tag{2.12}$$

where

$$\phi_c^u = \angle(\mathbf{P}_q - \mathbf{P}_u) \tag{2.13}$$

$$\theta_c^u = \arctan(\frac{d_{\text{bs}}^q}{|\mathbf{P}_q - \mathbf{P}_u|}), \quad \text{for} \quad q = Q(c). \tag{2.14}$$

The ideal beam pattern model defined by 3GPP describes a 3D pattern for the main lobe of a desired cell beam by combining two cross-sectional 2D pattern components in the azimuth and the elevation plane. In addition, the model specifies the required side lobe level (SLL) and the attenuation level of the radiation in the backward direction and the corresponding values in dB scale are described by SLA_{o} and BA_{o} respectively [3GP13a]. The model allows to set the values of the essential beam parameters such as azimuth orientation Φ_c, elevation tilt Θ_c, half power (3dB) beam width (HPBW) Φ_{3dB}^c in azimuth and Θ_{3dB}^c in elevation plane. Accordingly, the 3D beam pattern is computed as a product of the 2D patterns: azimuth and elevation plane pattern components which are denoted by $B_c^{\text{h}}(\Phi_c, \Theta_c, \phi_c^u)$ and $B_c^{\text{v}}(\Theta_c, \theta_c^u)$ in linear scale and $\widehat{B_c^{\text{h}}}(\Phi_c, \Theta_c, \phi_c^u)$ and $\widehat{B_c^{\text{v}}}(\Theta_c, \theta_c^u)$ in dB scale, respectively,

$$B_c(\Phi_c, \Theta_c, \phi_c^u, \theta_c^u) = \min\{B_c^{\text{h}}(\Phi_c, \Theta_c, \phi_c^u) \cdot B_c^{\text{v}}(\Theta_c, \theta_c^u), 10^{BA_{\text{o}}}\}. \tag{2.15}$$

The azimuth and elevation plane beam pattern components in dB scale are described as [3GP13a]

$$\widehat{B_c^{\text{h}}}(\Phi_c, \Theta_c, \phi_c^u) = 20 \cdot \log_{10}(B_c^{\text{h}}(\Phi_c, \Theta_c, \phi_c^u)), \tag{2.16}$$

$$\widehat{B_c^{\text{v}}}(\Theta_c, \theta_c^u) = 20 \cdot \log_{10}(B_c^{\text{v}}(\Theta_c, \theta_c^u)), \tag{2.17}$$

and

$$\widehat{B_c^{\text{h}}}(\Phi_c, \Theta_c, \phi_c^u) = -\min\{12 \cdot \left(\frac{\phi_c^u - \Phi_c}{\Phi_{\text{3dB}}^c}\right)^2, SLA_{\text{o}}\}, \quad \forall \Theta_c \in [-90°, 90°],$$

$$\widehat{B_c^{\text{v}}}(\Theta_c, \theta_c^u) = -\min\{12 \cdot \left(\frac{\theta_c^u - \Theta_c}{\Theta_{\text{3dB}}^c}\right)^2, SLA_{\text{o}}\}. \tag{2.18}$$

2.2.1.4 LTE Link Budget

In this section, the LTE radio resource block definition and link budget calculation for LTE downlink is presented.

As LTE downlink employs Orthogonal Frequency Division Multiplexing (OFDM), a multi-carrier transmission over several narrow bands, the radio resource block is defined in a time-frequency grid [HT09]. The smallest LTE radio resource unit termed, known as as Resource Element (RE), is defined per a sub-carrier of $15 \cdot 10^3$ Hz bandwidth in frequency and a single OFDM symbol in time. The radio resource is allocated in small chunk of a group of REs called Physical Resource Block (PRB) where a single PRB spans 12 consecutive sub-carriers in frequency having a bandwidth of $\Omega_{\mathrm{PRB}} = 180 \cdot 10^3$ kHz and 1 ms wide in time which is also called Transmission Time Interval (TTI) [HT09, HT11].

LTE technology supports a wide range of operating bandwidths and assuming the total system bandwidth of Ω in [MHz], the the total number of available PRBs for each cell is

$$M_{\mathrm{PRB}} = \left\lfloor \frac{\Omega}{\Omega_{\mathrm{PRB}}} \right\rfloor. \tag{2.19}$$

$\lfloor \cdot \rfloor$ is floor operator.

Assuming fixed amount of power of P_a is available for transmission over a single PRB per sector-antenna a, the transmit power of cell c over a single PRB P_c^{tx} depends on the number of cells being simultaneously served by the sector-antenna. The fraction of P_a transmitted over cell-specific beam is described by $\alpha_c \in [0, 1]$,

$$P_c^{\mathrm{tx}} = \alpha_c \cdot P_a, \quad \text{where} \quad A(c) = a. \tag{2.20}$$

Assuming an LTE downlink signal transmission and $h_c^u(\Phi_c, \Theta_c)$ is the overall attenuation of the signal incorporating antenna gain, path loss, shadowing and additional loss experienced due to wall penetration for indoor user L_o given in dB scale where

$$h_c^u(\Phi_c, \Theta_c) = G_c^u(\Phi_c, \Theta_c) \cdot 10^{\frac{\widehat{S_c^u} + \Upsilon + 10 \cdot \varrho \cdot \log_{10}(d_{c,u}) + L_o}{10}}, \tag{2.21}$$

the signal power P_c^u received by UE u from cell c is

$$P_c^u = h_c^u(\Phi_c, \Theta_c) \cdot P_c^{\mathrm{tx}}. \tag{2.22}$$

The best serving cell of UE is selected based on the strength of the Reference Signal Received Power (RSRP) given by $RSRP_c^u$ measured in downlink by the UE over the

REs that carry cell-specific Reference Symbols (RSs) [HT09,HT11]. $RSRP_c^u$ is defined as a linear average of the signal powers measured from all cell-specific RSs within the considered measurement frequency bandwidth. Hence, the average $RSRP_c^u$ value is computed as the power received over a single RE that carries the RS,

$$RSRP_c^u = \frac{\Omega_{\mathrm{PRB}}}{15 \cdot 10^3} \cdot h_c^u(\Phi_c, \Theta_c) \cdot P_c^{\mathrm{tx}}. \tag{2.23}$$

Having the $RSRP_c^u$ measurements from all cells, the best serving cell of UE u which is described by a connection function $s(u)$ is the cell with the strongest RSRP measured value, i.e.

$$s(u) = \operatorname*{argmax}_{c \in \mathcal{C}} \ \{RSRP_c^u\}. \tag{2.24}$$

2.2.2   Ray-Tracing Based Three-Dimensional Cellular Model

2.2.2.1   Realistic Non-Regular Cellular Layout

This section presents non-regular cellular layout of a realistic macro-site deployment scenario utilized for ray-tracing based investigation. The index notations for BS site, sector-antenna, beam and cell as well as propagation variables defined in Section 2.2.1.1 are still valid and applicable as well for the RT-based cellular model in the same way unless stated otherwise.

Ray-tracing is a mechanism of approximating signal propagation loss using ray-based technique in a simplified three dimensional model of a particular environment representing the real-world clutter behavior. In this thesis work, a 3D-model of a typical European city is imported into a network-planning tool from available vector database of the city map and its 3D building structure. Non-regular cellular layout and an irregularly deployed LTE sectorized sites are considered. Due to the fact that each site locations in this scenario is based on realistic deployment data, the number of sector-antennas per site is not-necessarily one. Figure 2.2 clearly depicts the irregular pattern of the site-deployment and the 3D-model representation of the considered propagation environment.

2.2.2.2   Ray-Tracing Based Radio Propagation Model

This section discusses the type of RT-based propagation prediction technique employed to characterize the radio channel for the 3D-model scenario.
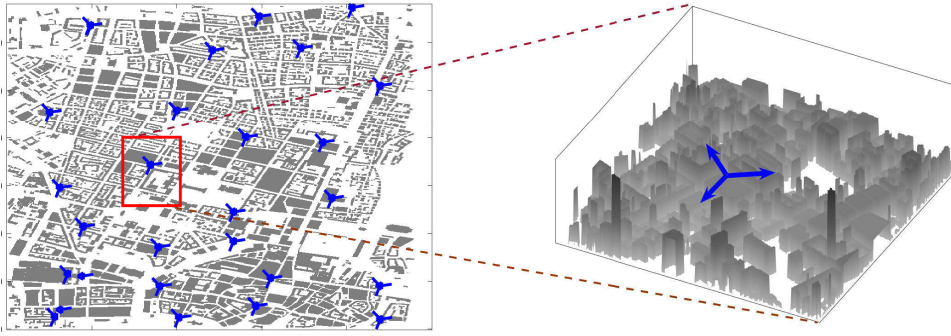
Figure 2.2. RT-scenario: Cellular layout in a 3D-model

The received signal power level at any point in the outdoor environment is predicted using a RT-technique. The prediction technique captures the real-world propagation effects by taking various propagation phenomenon such as reflections, diffractions, and diffuse scattering into account [YI15, VDEF+15]. Various studies in [EFL+97, KGI+99, CLW+03] have demonstrated that ray-tracing predictions provide reliable performance data comparable to field measurements. This makes the ray-tracing based emulators more suitable for studying radio channel characteristics. The employed ray tracing method utilizes Dominant Path Prediction Model (DPM) where the total propagation loss from a transmitting antenna to a desired receiver location is predicted in the direction of the path taken by single dominant ray which brings most of the energy to the point of prediction [WRPW, WL]. Despite the fact that employing several prediction-rays provides possibility to include the effects of multiple propagation paths, manipulation of huge data with respect to each ray and the resulting computational complexity hinder its wide application. DPM, on the other hand, provides acceptable performance comparable to the several-ray approach with a significantly reduced computational effort. Details of the DPM model and performance analysis can be referred in [Wah11].

Accurate prediction of the propagation loss using RT-approach requires knowing the radiation pattern of the transmit and receive antenna under consideration [Wah11]. Available measured radiation patterns of real-antennas are used in the RT-scenario at each BS sector-antenna.

The RT-based propagation prediction is performed in downlink for an LTE system. The typical conventional sectorization, single cell per sector-antenna, is considered in the prediction scenario. Each beam serving cell is configured with fixed Φ_c and variable Θ_c settings. The prediction is carried out cell-wise where only one sector-antenna is transmitting at a time. Each prediction is performed for a specific Θ_c in a pixel-based approach where a pixel is considered as a potential spatial location of UE u, i.e., $\mathbf{P}_u$.

The network area depicted in Figure 2.2 is divided into grid of pixels having equal spacing d_{pix}. The prediction coverage area denoted by $\mathcal{A}_{\text{P}}$ is defined as the set of those pixel points, i.e. $\mathcal{A}_{\text{P}} = \{u\}$. The value of the received signal power $\mathbf{P}_u$ at any outdoor pixel points is directly obtained using the RT using DPM whereas the indoor values are estimated from the outdoor values by applying additional post processing. The value of $\mathbf{P}_u$ at the indoor pixels are computed from the strongest ray detected at one of the outdoor pixels around the 3D model of the considered building. This is performed by adding a constant wall penetration loss L_o plus an additional attenuation of 0.6 dB/m for the distance traveled inside the building [KGW$^+$14, E.99, HKS09]. Based on these approaches, the RT-tool provides a set of tilt-specific received power map of $\mathcal{P}_c(\Theta_c)$ for each cell by collecting all the received power values from the entire grid-of pixels within the network, i.e., $\mathcal{P}_c(\Theta_c) = \{P_c^u | \forall u \in \mathcal{A}_{\text{P}}\}$.

2.3   Beam Pattern Design for Active Antenna Systems Based Sectorization

2.3.1   Introduction

In a sectorised cellular deployment, the radiation pattern of the sector-antenna determines the coverage size of each cell. Designing the radiation pattern of the cell-specific beam aims at achieving the desired beam width, borseight steering angle (Φ_c, Θ_c) of the main lobe and a suppressed side and back lobe levels. Beamfomring is a signal processing technique that enable to define the radiation pattern by controlling the relative phase and amplitude of the input signals at each antenna array element. WIth AAS, 3D beamforming feature is supported that exploits the spatial degree of freedom both in the azimuth and elevation domain [LC10, Net].

This section provides a simplified beamforming model and beam pattern design approach that allows to create cell-specific beams suitable for AAS-based dynamic sectorization. The beam pattern design criteria used to different types of sectorization, i.e, conventional, horizontal and vertical sectorization, are provided as well. Section 2.3.2 describes more generic 3D beamforming scheme that can be used to design a desirable beam pattern considering AAS consisting of planar array arrangement. The beam pattern design method and specific design criteria are presented for each types of sectorization in Section 2.3.3.

2.3.2 Beamforming Technique for Beam Pattern Design

This section presents the 3D beamforming technique and specification as a basis for designing a cell-specific beam pattern.

AAS consisting of a 2D planar array of identical antenna elements arranged in the Y and Z axis direction with array size of $N_Z \times N_Y$ is considered. The array elements are placed regularly with an inter-array-element spacing of r_y and r_z in Y and Z axis direction, respectively. As depicted in Figure 2.3(a), each antenna element in the array is indicated by (k,i) where $k = 1, \ldots, N_Z$ and $i = 1, \ldots, N_Y$. The Cartesian coordinate (x, y, z) of the (k,i) array element is given by a vector $\mathbf{r}_{k,i} = [x_{k,i},\ y_{k,i},\ z_{k,i}]^{\mathrm{T}}$ where $x_{k,i} = 0$, $y_{k,i} = (i-1) \cdot r_y$, $z_{k,i} = (k-1) \cdot r_z$. $[\cdot]^{\mathrm{T}}$ is vector transpose operator. Assuming large enough spacing between the array elements, the effect of mutual coupling is neglected [WJ04, Bal05]. Figure 2.3(a) shows a two column AAS array diagram where a cross polarized antenna element is placed at each (k,i) element position and connected to its own transceiver (TRX). For the sake of clarity, the spherical coordinate system adopted throughout the thesis is provided in Figure 2.3(b).
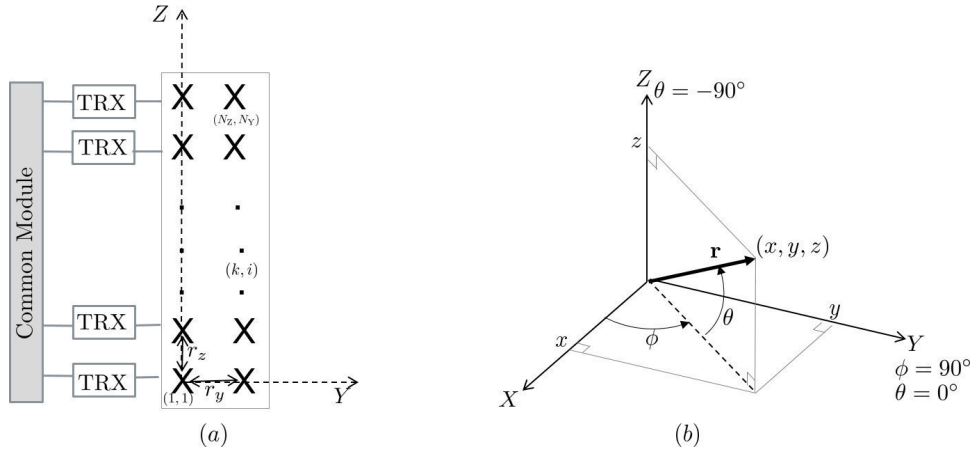
Figure 2.3. (a)Array diagram of AAS (b)Spherical coordinate system

Given the normalized stand-alone pattern of the array element by $\nu(\phi, \theta)$, the response of each antenna element when a plane wave of wave length λ impinges the array plane in the direction ϕ and θ is described by

$$V_{k,i}(\phi, \theta) = \nu(\phi, \theta) \cdot \frac{1}{\sqrt{N_{\mathrm{Z}} \cdot N_{\mathrm{Y}}}} \cdot \exp(j\mathbf{k}^{\mathrm{T}}\mathbf{r}_{k,i}), \qquad (2.25)$$

where $\mathbf{k} = \frac{2 \cdot \pi}{\lambda}\hat{\mathbf{r}}$ is the wave vector, and $\hat{\mathbf{r}}$ is a unit vector in the propagation direction of the incident plane wave, i.e. $\hat{\mathbf{r}} = -[\cos(\phi)\cos(\theta)\quad \sin(\phi)\cos(\theta)\quad \sin(\theta)]^{\mathrm{T}}$ [God04].

In beamforming, the responses of all array elements are combined to give the radiation pattern of the complete array also known as array beam pattern. Unless additional processing is applied to the input signal at each array element, the direction of the maximum of the beam pattern remains perpendicular to the 2D planar plane where the array elements are arranged [God04].

The beam pattern serving cell c whose maximum gain is desired to be in the (Φ_c, Θ_c) direction is formed by adjusting both the amplitude and phase of the input signal and this is digitally achieved by applying a complex beamforming weight $w_{k,i}(\Phi_c, \Theta_c)$ [MW99, LW10, Man05]. Thus, the beam pattern described by $B_c(\Phi_c, \Theta_c, \phi, \theta)$ is derived as superposition of the individual weighted element's response

$$B_c(\Phi_c, \Theta_c, \phi, \theta) = \sum_{k=1}^{N_Z} \sum_{i=1}^{N_Y} w_{k,i}^*(\Phi_c, \Theta_c) \cdot V_{k,i}(\phi, \theta). \tag{2.26}$$

The integration of active elements in the AAS allows dynamic and fast adaptation of the beam pattern using advanced 3D-beamforming by exploiting the azimuth and elevation spatial domain [Ame11, Net, LC10]. Besides different base band signals can be independently transmitted using each AAS array element as several several antenna input ports are supported with the AAS architecture. This enables to simultaneously create multiple beams with specific characteristic when it is intended to increase the number of cells served by a single sector-antenna [LC10].

Given the response of all array elements by array response vector $\mathbf{V}(\phi, \theta) \in \mathbb{C}^{N_Z \cdot N_Y \times 1}$ with elements $V_{k,i}(\phi, \theta)$ and the 3D beamforming weight vector $\mathbf{W}_c \in \mathbb{C}^{N_Z \cdot N_Y \times 1}$ with elements $w_{k,i}(\Phi_c, \Theta_c)$, the 3D beam pattern $B_c(\Phi_c, \Theta_c, \phi, \theta)$ is formulated as

$$B_c(\Phi_c, \Theta_c, \phi, \theta) = \mathbf{W}_c^{\mathrm{H}} \mathbf{V}(\phi, \theta), \tag{2.27}$$

where $[\cdot]^{\mathrm{H}}$ denotes the Hermitian transpose of a vector.

Since azimuth orientation Φ_c and elevation tilt Θ_c of a cell are essential parameters to adjust the coverage and tune system performance, steering the boresight of the beam towards the desired (Φ_c, Θ_c) direction is one of the design criteria of the optimal beamforming weight vector $\mathbf{W}_c$ of cell c [Mis15]. In addition, it is required to reduce the radiation of the antenna power outside the main lobe to mitigate inter-cell interference and this can be achieved by suppressing the level of the side lobes of the beam pattern [God04].

While executing sectorization, the 3D beamforming procedure is performed as a combination of horizontal and vertical beamforming applied on a sub-array group in order

to steer and shape the beam with respect to each array dimension. The steering angles (Φ_c, Θ_c) of each cell beam is usually determined a priori and the values can be taken either from a default or optimized network parameter set. The weight $w_{k,i}(\Phi_c, \Theta_c)$ applied at each array element is defined as a product of the horizontal and vertical components given by $\tilde{w}_i(\Phi_m)$ and $\tilde{w}_k(\Theta_m)$, respectively, [Ste09]. Thus, $w_{k,i}(\Phi_c, \Theta_c)$ is

$$w_{k,i}(\Phi_c, \Theta_c) = \tilde{w}_i(\Phi_c) \cdot \tilde{w}_k(\Theta_c). \tag{2.28}$$

Given the vertical beamforming weight vector applied at each array column by $\mathbf{W}_c^{\mathrm{v}} \in \mathbb{C}^{N_{\mathrm{Z}} \times 1}$ having elements $\tilde{w}_k(\Theta_c)$ and horizontal beamforming weight vector for each array row $\mathbf{W}_c^{\mathrm{h}} \in \mathbb{C}^{N_{\mathrm{Y}} \times 1}$ consisting of $\tilde{w}_i(\Phi_c)$, the 3D beamforming weight vector of the antenna array can be re-expressed as the Kronecker product of the horizontal and vertical beamforming vectors [LW10, HSKH13],

$$\mathbf{W}_c = \mathbf{W}_c^{\mathrm{h}} \otimes \mathbf{W}_c^{\mathrm{v}}. \tag{2.29}$$

The 2D array response vector defined in Equation (2.27) can as well be decomposed into components containing steering vectors in the azimuth and elevation array dimension.described by $\mathbf{V}^{\mathrm{v}}(\theta) \in \mathbb{C}^{N_{\mathrm{Z}} \times 1}$ and $\mathbf{V}^{\mathrm{h}}(\phi, \theta) \in \mathbb{C}^{N_{\mathrm{Y}} \times 1}$ composed of elements $\tilde{V}_k(\theta)$ and $\tilde{V}_i(\phi, \theta)$ respectively, i.e.,

$$\mathbf{V}(\phi, \theta) = \mathbf{V}^{\mathrm{h}}(\phi, \theta) \otimes \mathbf{V}^{\mathrm{v}}(\theta), \tag{2.30}$$

where

$$\tilde{V}_i(\phi, \theta) = \tilde{\nu}(\phi) \cdot \exp(-j(i-1) \cdot r_y \cdot \sin(\phi) \cdot \cos(\theta)) \tag{2.31}$$

$$\tilde{V}_k(\theta) = \tilde{\nu}(\theta) \cdot \exp(-j(k-1) \cdot r_z \cdot \sin(\theta)), \tag{2.32}$$

The element pattern is also can be described in the same manner as the product of its azimuth and elevation components, i.e, $\nu(\phi, \theta) = \tilde{\nu}(\phi) \cdot \tilde{\nu}(\theta)$ [Bal05]. By incorporating the vertical and horizontal components of the weight and steering vectors shown in Equation 2.29 and Equation 2.30, a compact expression for Equation (2.26) is redefined as

$$\begin{aligned} B_c(\Phi_c, \Theta_c, \phi, \theta) &= (\mathbf{W}_c^{\mathrm{h}} \otimes \mathbf{W}_c^{\mathrm{v}})^{\mathrm{H}} (\mathbf{V}^{\mathrm{h}}(\phi, \theta) \otimes \mathbf{V}^{\mathrm{v}}(\theta)) \\ &= ([\mathbf{W}_c^{\mathrm{h}}]^{\mathrm{H}} \mathbf{V}^{\mathrm{h}}(\phi, \theta)) \otimes ([\mathbf{W}_c^{\mathrm{v}}]^{\mathrm{H}} \mathbf{V}^{\mathrm{v}}(\theta)) \\ &= B_c^{\mathrm{h}}(\Phi_c, \phi, \theta) \cdot B_c^{\mathrm{v}}(\Theta_c, \theta). \end{aligned} \tag{2.33}$$

Therefore, the 3D beam pattern value at any angle (ϕ, θ) can be computed as the product of its horizontal $B_c^{\mathrm{h}}(\Phi_c, \phi, \theta)$ and vertical $B_c^{\mathrm{v}}(\Theta_c, \theta)$ components.

The HPBW of the cell beam main lobe is the other characteristics of that determines the coverage of a cell. The flexibility in achieving a desirable HPBW values in the azimuth

and elevation plane, Φ^c_{3dB} and Θ^c_{3dB} respectively, are mainly determined by the size of the antenna aperture in the respective dimension. This is defined by the size of the array and the inter-array-element spacing [Rud83]. A single column antenna array configuration is suitable and widely employed to create the typical wide-beam used in the conventional macro-cell in the traditional tri-sectored site deployment [HH15, LN01]. A higher order sectorization implementation in the horizontal dimension, however, requires creating minimally-overlapped narrower beams having smaller Φ^c_{3dB} in order to split the conventional-cell horizontally in to two. Such type of sectorization, as a result, demands more number of antenna columns approximately proportional to the desired reduction factor of the HPBW in the azimuth dimension [HH15, FJNC].

2.3.3 Beam Pattern Design for Different Types of Sectorization

2.3.3.1 Conventional Sectorization

This section describes the beam pattern design approach for conventional sectorization where a sector-antenna serves only a single cell.

In conventional sectorization mode, cell coverage is maintained by creating a beam having azimuth beam with the same as that of the with of the individual array element pattern while the boresight is steered to an intended tilt angle in the elevation plane. In the traditional macro-cell deployment, the conventional cell type is served by a BS antenna equipped with one column array configuration [HH15, LN01]. Thus, a single column array sub-group is chosen from the 2D-array of the AAS for the conventional-cell beamforming. With such arrangement, having a one-dimensional array sub-group provides the degree of freedom that allows controlling the beam pattern only in the array dimension. As a result, only beamforming processing on the vertical antenna elements is carried out to get the suitable elevation pattern component of the cell beam whereas the azimuth pattern is solely determined by the azimuth plane pattern behavior of the array element, i.e. $\tilde{\nu}(\phi)$. Therefore, the 3D weight vector required to synthesize the conventional cell beam becomes the same as the vertical beamforming weight component, i.e,

$$\mathbf{W}_c = \mathbf{W}^v_c, \qquad \text{for} \quad b_{Q(c)} = 0. \qquad (2.34)$$

Steering the boresight of the beam main lobe (ML) to a desired orientation angle of Θ_c, and reducing the SLL to a minimum level are considered as sufficient beamforming criteria for designing the cell beam pattern. The beamforming optimization problem is,

therefore, defined as a minimization problem that aims at reducing the total radiated power at the side lobes (SLs) to achieve a minimum SLL level under SLA_o as specified in the 3GPP model [3GP13a]. The ML region in the elevation plane which determines the width of the desired cell coverage is represented by set of elevation angles $\Theta_c^\mathrm{ML} = \{\forall\theta : \theta \in \{\Theta_c + [-\theta_c^\mathrm{ML}, \theta_c^\mathrm{ML}]\}\}$ where $\pm\theta_c^\mathrm{ML}$ are offset angles from Θ_c at which the beam pattern attains its first minimum point, equivalent to first null of a beam. The set of the SL angles Θ_c^SL is defined as well by excluding Θ_c^ML as $\Theta_c^\mathrm{SL} = \{\forall\theta : \theta \in [-90°, 90°] \wedge \theta \notin \Theta_c^\mathrm{ML}\}$. $\pm\theta_c^\mathrm{ML}$ values are computed based on the beam pattern specification defined in Equation 2.18 by evaluating the ML beam pattern value to SLA_o,

$$\theta_c^\mathrm{ML} = \pm\sqrt{\frac{SLA_\mathrm{o}}{12}} \cdot \Theta_\mathrm{3dB}^c. \tag{2.35}$$

Matrix of array response vectors $\mathbf{V}_\mathrm{ML}^\mathrm{v}(\Theta_c^\mathrm{ML}) \in \mathbb{C}^{N_\mathrm{Y} \times N_\mathrm{ML}}$ and $\mathbf{V}_\mathrm{SL}^\mathrm{v}(\Theta_c^\mathrm{SL}) \in \mathbb{C}^{N_\mathrm{Y} \times N_\mathrm{SL}}$ associated to the ML and SL regions, respectively, are created for the set of sampled angle values of Θ_c^ML and Θ_c^SL as

$$\mathbf{V}_\mathrm{ML}^\mathrm{v}(\Theta_c^\mathrm{ML}) = [\mathbf{V}^\mathrm{v}(\theta_1), \ldots, \mathbf{V}^\mathrm{v}(\theta_{t_\mathrm{ML}})], \quad \text{for } \theta_{t_\mathrm{ML}} \in \Theta_c^\mathrm{ML} \quad \text{and} \quad t_\mathrm{ML} = 1, \ldots, \mathrm{N}_{ML} \tag{2.36}$$

$$\mathbf{V}_\mathrm{SL}^\mathrm{v}(\Theta_c^\mathrm{SL}) = [\mathbf{V}^\mathrm{v}(\theta_1), \ldots, \mathbf{V}^\mathrm{v}(\theta_{t_\mathrm{SL}})], \quad \text{for } \theta_{t_\mathrm{SL}} \in \Theta_c^\mathrm{SL} \quad \text{and} \quad t_\mathrm{SL} = 1, \ldots, N_\mathrm{SL} \tag{2.37}$$

where $N_\mathrm{ML} = |\Theta_c^\mathrm{ML}|$ and $N_\mathrm{SL} = |\Theta_c^\mathrm{SL}|$.

Including the constraint of maintaining a unity gain at Θ_c, the beamforming optimization problem is defined as

$$\underset{\mathbf{W}_c^\mathrm{v}}{\mathrm{argmin}} \quad || [\mathbf{W}_c^\mathrm{v}]^\mathrm{H}\mathbf{V}_\mathrm{SL}^\mathrm{v}(\Theta_c^\mathrm{SL}) ||_2^2 , \quad \text{subject to:} \quad [\mathbf{W}_c^\mathrm{v}]^\mathrm{H}\mathbf{V}^\mathrm{v}(\Theta_c) = 1 \tag{2.38}$$

where $|| \cdot ||_2$ is a 2-norm operator. Equation (2.38) is a linearly constrained quadratic optimization problem having the same form as a minimum variance beamformer (MVB) [VGL03, JL15, LJLL13]. The optimization problem can be solved efficiently with Lagrange multiplier technique using the objective function

$$F(\mathbf{W}_c^\mathrm{v}, \omega) = [\mathbf{W}_c^\mathrm{v}]^\mathrm{H}X\mathbf{W}_c^\mathrm{v} + \omega \cdot ([\mathbf{W}_c^\mathrm{v}]^\mathrm{H}\mathbf{V}^\mathrm{v}(\Theta_c) - 1)$$

$$\text{where} \quad X = \mathbf{V}_\mathrm{SL}^{(\mathrm{v})}(\Theta_c^\mathrm{SL})[\mathbf{V}_\mathrm{SL}^{(\mathrm{v})}(\Theta_c^\mathrm{SL})]^\mathrm{H} \tag{2.39}$$

where ω is the Lagrangian multiplier used with respect to the constraint. The solution of Equation (2.39) has a well known closed form of solution [LJLL13, J.C05],

$$\mathbf{W}_c^\mathrm{v} = \frac{X^{-1}\mathbf{V}^\mathrm{v}(\Theta_c)}{[\mathbf{V}^\mathrm{v}(\Theta_c)]^\mathrm{H}X^{-1}\mathbf{V}^\mathrm{v}(\Theta_c)} \tag{2.40}$$

The performance of the applied beamforming is illustrated in Figure 2.4. The elevation plane beam pattern generated using the optimized beamforming weights $B_c^\mathrm{v}(\Theta_c, \theta)$ are
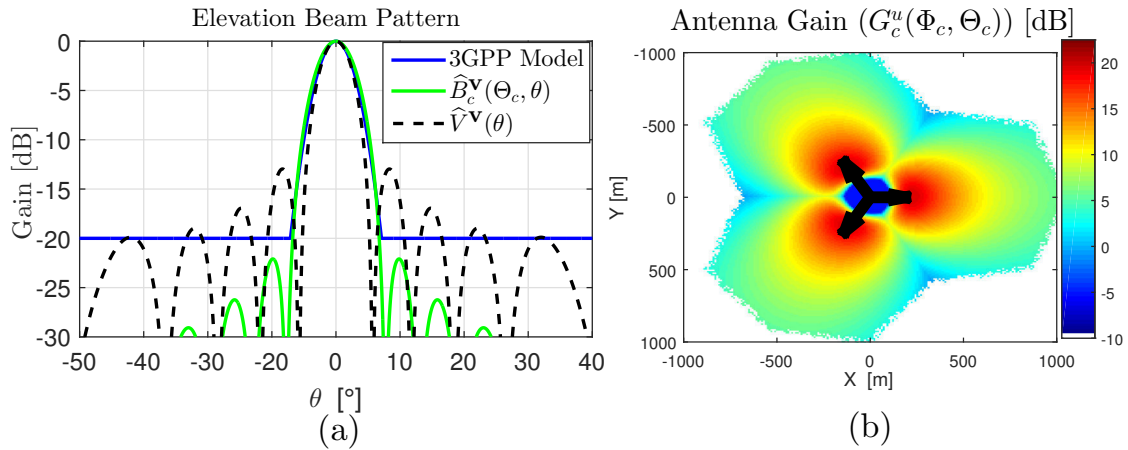
Figure 2.4. Conventional-cell: (a) Elevation beam pattern, (b) Antenna gain at ground level

depicted together with the elevation component of the array response $V^{\mathrm{v}}(\theta)$ and the reference pattern obtained using the 3GPP model for $\Theta_c = 0°$ and $SLA_{\mathrm{o}} = 20$ dB. The diagram shows the gain values in dB scale, i.e. $\widehat{B_c^{\mathrm{v}}}(\Theta_c, \theta) = 20 \cdot \log(B_c^{\mathrm{v}}(\Theta_c, \theta))$ and $\widehat{V}^{\mathrm{v}}(\theta) = 20 \cdot \log(V^{\mathrm{v}}(\theta))$, respectively. As depicted in Figure 2.4(a) effective SLL suppression is achieved by applying by applying the optimized beamforming weight with a trade-off of slight broadening of the ML compared to the $\widehat{V}^{\mathrm{v}}(\theta)$ (without beam forming weight). However, this can be adjusted to some extent by using the ML angular range as defined in Equation 2.35 via reducing the offset values of θ_c^{ML} while monitoring the SLL. The total antenna gain value, including both horizontal and vertical pattern effect as defined in Equation 2.33, on the ground plane of down-tilted beams serving co-sited conventional cells is illustrated in Figure 2.4(b).

2.3.3.2 Vertical Sectorization

This section presents beam pattern design approach for Vertical sectorization (VS) where the conventional-cell is split into two cells and the sector-antenna serves the two cells using dedicated vertical beams as demonstrated in Figure 2.1 (b).

In VS realization, two beams $b_a = 1$ and $b_a = 2$ with different elevation tilt angles Θ_{c1} and Θ_{c2}, respectively, are simultaneously created from sector-antenna a where each beam broadcasts its own PCI corresponding to the cell $c1, c2 \in \mathcal{C}$ and $A(c1) = A(c2)$. The azimuth HPBW of the vertical beam is configured to be the same as the beam employed for the conventional cell, i.e., $\Phi_{3\mathrm{dB}}^{c1} = \Phi_{3\mathrm{dB}}^{c2}$. Such HPBW configuration aims at minimizing the impacts the VS may introduce on the coverage of the other co-sited or

surrounding neighbor cells. To fulfill this requirement, a single column sub-array group is maintained for the VS beamforming. This leads to a beam pattern design performed by applying vertical beamforming on the selected single column array sub-group to achieve the following design targets.

One of the challenges in VS is the risk of the overlap between the vertical beams in the elevation plane. The amount of beam overlap determines the severity of the inter-cell interference problem that may occur. This overlap can be dramatically minimized by spatially isolating the beams with a higher elevation tilt offset and reduced elevation HPBW θ_{3dB}^{c1} configurations. However, θ_{3dB}^c and θ_c are sensitive parameters in controlling the size of the cell coverage as the performance trade-offs between the coverage and interference level is highly limiting. Achieving the minimum beam overlap while maintaining a balanced coverage between the vertical cells is a key aspect that is considered in the beamforming design criteria, in addition to what is defined by Equation (2.38).

One approach to deal with the interference in the overlap region is to suppress the SLL peak at the angle $\Theta_c^{\mathrm{I}}, c \in \{c1, c2\}$ where the interferer beam has maximum gain. Enforcing those constraints, the vertical beams are formed by a joint beamforming scheme combining the optimization problem and beam-specific design criteria. The joint optimization problem is described by

$$\underset{\mathbf{W}_{c1}^{\mathrm{v}}, \mathbf{W}_{c2}^{\mathrm{v}}}{\operatorname{argmin}} \quad || \, [\mathbf{W}_{c1}^{\mathrm{v}}]^{\mathrm{H}} \mathbf{V}_{\mathrm{SL}}^{\mathrm{v}}(\Theta_{c1}^{\mathrm{SL}}) \, ||_2^2 + || \, [\mathbf{W}_{c2}^{\mathrm{v}}]^{H} \mathbf{V}_{\mathrm{SL}}^{\mathrm{v}}(\Theta_{c2}^{\mathrm{SL}}) \, ||_2^2 \tag{2.41}$$

$$\text{subject to:} \quad [\mathbf{W}_{c1}^{\mathrm{v}}]^{\mathrm{H}} \mathbf{V}^{\mathrm{v}}(\Theta_{c1}) = [\mathbf{W}_{c2}^{\mathrm{v}}]^{\mathrm{H}} \mathbf{V}^{\mathrm{v}}(\Theta_{c2}) = 1, \tag{2.42}$$

$$[\mathbf{W}_{c1}^{\mathrm{v}}]^{\mathrm{H}} \mathbf{V}^{\mathrm{v}}(\Theta_1^I) = [\mathbf{W}_{c2}^{\mathrm{v}}]^{\mathrm{H}} \mathbf{V}^{\mathrm{v}}(\Theta_c^I) = \zeta \tag{2.43}$$

$$\Theta_c^{\mathrm{I}} = \Theta_{t_c}, \quad c, t_c \in \{c1, c2\} \quad \text{and} \quad t_c \neq c, \tag{2.44}$$

where the constraint at Equation (2.43) is included to ensure that the beam pattern at the selected angle Θ_c^{I} in the overlapped region of the vertical beams is suppressed to ζ level. Equation (2.41) can be reformulated to derive a combined minimization problem having the same form as shown in Equation (2.38). Combining the weights, array response vectors and constraint matrix as described below,

$$\mathbf{W}^{\mathrm{v}} = [\mathbf{W}_{c1}^{\mathrm{v}} \quad \mathbf{W}_{c2}^{\mathrm{v}}]^{\mathrm{T}}, \tag{2.45}$$

$$\mathbf{V}_{\mathrm{SL}}^{\mathrm{v}}(\Theta^{\mathrm{SL}}) = \begin{bmatrix} \mathbf{V}_{\mathrm{SL}}^{\mathrm{v}}(\Theta_{c1}^{\mathrm{SL}}) & 0_{N_z \times N_{\mathrm{SL}},} \\ 0_{N_z \times N_{\mathrm{SL}}} & \mathbf{V}_{\mathrm{SL}}^{(\mathrm{v})}(\Theta_{c2}^{\mathrm{SL}}) \end{bmatrix}. \tag{2.46}$$

$$\mathbf{V}^{\mathrm{v}}(\Theta) = \begin{bmatrix} \mathbf{V}^{\mathrm{v}}(\Theta_{c1}) & 0_{N_{\mathrm{z}} \times 1} & \mathbf{V}^{\mathrm{v}}(\Theta_{c1}^{\mathrm{I}}) & 0_{N_{\mathrm{z}} \times 1} \\ 0_{N_{\mathrm{z}} \times 1} & \mathbf{V}^{\mathrm{v}}(\Theta_{c2}) & 0_{N_{\mathrm{z}} \times 1} & \mathbf{V}^{\mathrm{v}}(\Theta_{c2}^{\mathrm{I}}) \end{bmatrix} \text{ and } \mathbf{C} = \begin{bmatrix} 1 & 1 & \zeta & \zeta \end{bmatrix}^{\mathrm{T}}. \quad (2.47)$$

The combined joint optimization problem expressed with a well known general form [VGL03]

$$\underset{\mathbf{W}^{\mathrm{v}}}{\operatorname{argmin}} \quad || \, [\mathbf{W}^{\mathrm{v}}]^{\mathrm{H}} \mathbf{V}^{\mathrm{v}}_{\mathrm{SL}}(\Theta^{\mathrm{SL}}) \, ||_2^2 \,,$$

$$(2.48)$$

$$\text{subject to:} \quad [\mathbf{W}^{\mathrm{v}}]^{\mathrm{H}} \mathbf{V}^{\mathrm{v}}(\Theta) = \mathbf{C}^{\mathrm{T}}.$$

Since Equation 2.48 is in a form of a linearly constrained quadratic optimization problem, Lagrangian multiplier technique can be applied as shown in Equation (2.39) [VGL03, JL15, LJLL13] and the solution for the combined optimized weight vector becomes

$$\mathbf{W}^{\mathrm{v}} = \frac{\mathrm{X}^{-1}\mathbf{V}^{\mathrm{v}}(\Theta)\mathbf{C}}{[\mathbf{V}^{\mathrm{v}}(\Theta)]^{\mathrm{H}}\mathrm{X}^{-1}\mathbf{V}^{\mathrm{v}}(\Theta)}$$

$$(2.49)$$

$$\text{where} \quad X = \mathbf{V}^{\mathrm{v}}_{\mathrm{SL}}(\Theta^{\mathrm{SL}})[\mathbf{V}^{\mathrm{v}}_{\mathrm{SL}}(\Theta^{\mathrm{SL}})]^{\mathrm{H}}.$$
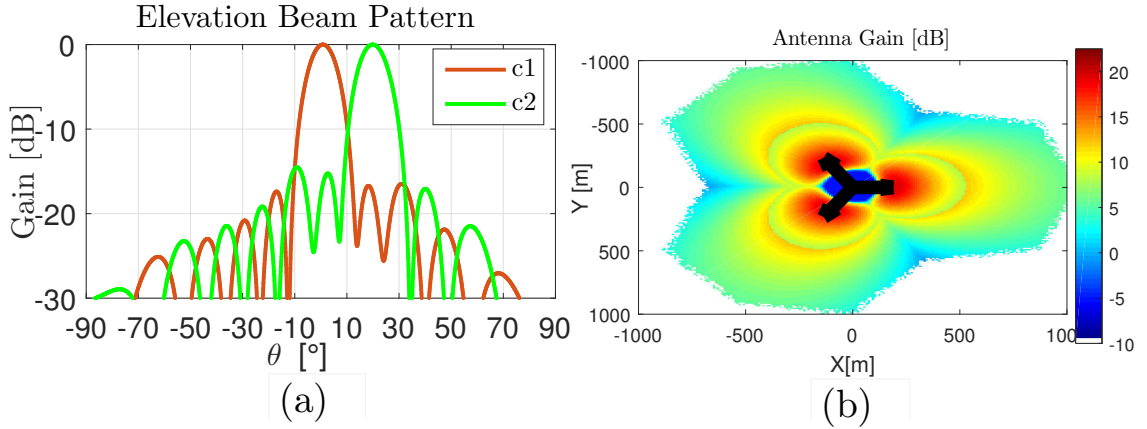
Figure 2.5. Vertical Beams: (a) Elevation beam pattern, (b) Antenna gain at ground level

Figure 2.5(a) depicts the elevation patterns of two vertical cell beams. It can be observed that adding additional constraint in the overlap region provides a better suppression of SL peak in the direction of the boresight of the interferer. Figure 2.5(b) illustrates the total antenna gain map for the co-sited cells after vertical sectorization.

2.3.3.3   Horizontal Sectorization

In this section, a beam pattern design approach is presented for the horizontal sectorization (HS) where the conventional-cell is replaced by two new cells which are served by a dedicated narrow horizontal beams emitted from a single sector-antenna.

The two narrow horizontal beams are created when it is desired to split the conventional-cell in the azimuth dimension. The HS deals with achieving considerably narrower azimuth HPBW $\Phi_{3\mathrm{dB}}^c$ configuration for the beams $b_a = 1$ and $b_a = 2$ serving cell $c \in \{c1, c2\} \subset \mathcal{C}$, $a = A(c)$ compared to the conventional cell beam. Due to the fact that creating a beam with reduced azimuth HPBW requires wider antenna aperture, an array of more than one column is needed [FJNC]. For the HS considered in this thesis, two columns of the array sub-group are utilized. The parameters of each horizontal beam are specified as a dedicated azimuth orientation and elevation tilt settings, Φ_c and Θ_c, respectively, in addition to the desirable minimal beam overlap criteria. Having a two-dimensional sub-array group provides the capability to exploit the degree of freedom in three-dimensional space enabling flexible adaptation of the beam pattern by applying 3D-beamfomring technique. The 3D-beamforming procedure, is therefore, performed as a combination vertical and horizontal components as discussed in Equation 2.29 and the resulting 3D weight vector is computed as

$$
\begin{aligned}
\mathbf{W}_c &= \mathbf{W}_c^{\mathrm{h}} \otimes \mathbf{W}_c^{\mathrm{v}} \\[2mm]
&= \begin{bmatrix} \widetilde{w}_1(\Phi_c) \cdot [\mathbf{W}_c^{\mathrm{v}}]^{\mathrm{T}} & \widetilde{w}_2(\Phi_c) \cdot [\mathbf{W}_c^{\mathrm{v}}]^{\mathrm{T}} \end{bmatrix}^{\mathrm{T}}.
\end{aligned}
\tag{2.50}
$$

The vertical beamforming weight component allows to adjust the orientation of the horizontal beams in the elevation plane to the desired respective tilt Θ_c. In the case of HS, since the elevation component of the pattern of both beams is not intended to be affected, it is maintained identical to what is defined for the conventional cell beam, hence, the beamforming weight solution defined by Equation 2.40 can be directly adopted.

The general approach of designing the horizontal component of the beam patterns deals with a joint optimization problem which minimizes the total radiated power over the SLs with constraints of maintaining the required boresight oreintation and supresed SL peak at Φ_c^{I} in the overlapped region of the beams where $\Phi_c^{\mathrm{I}} = \Phi_{t_c}$ and $t_c \neq c \in \{c1, c2\} \subset \mathcal{C}$. The approach employed for VS in Section 2.3.2.1 is applicable for HS by constructing and replacing the array response vectors and constraints by the

corresponding values defined in the horizontal array dimension in Section 2.3.1. The resulting joint cost function for the optimization of the combined horizontal beamforming weight vectors, i.e. $\mathbf{W}^{\mathrm{h}} = [\mathbf{W}^{\mathrm{h}}_{c1} \quad \mathbf{W}^{\mathrm{h}}_{c2}]^{\mathrm{T}}$, is expressed as

$$\underset{\mathbf{W}^{\mathrm{h}}}{\mathrm{argmin}} \quad \| \, [\mathbf{W}^{\mathrm{h}}]^{H} \mathbf{V}^{\mathrm{h}}_{\mathrm{SL}}(\Phi^{\mathrm{SL}}) \, \|_2^2 \, , \tag{2.51}$$

$$\text{subject to:} \quad [\mathbf{W}^{\mathrm{h}}]^{H} \mathbf{V}^{\mathrm{h}}(\Phi) = \mathbf{C}^{\mathrm{T}}.$$

The array response vectors' matrix are constructed as

$$\mathbf{V}^{\mathrm{h}}_{\mathrm{SL}}(\Phi^{\mathrm{SL}}) = \begin{bmatrix} \mathbf{V}^{\mathrm{h}}_{\mathrm{SL}}(\Phi^{\mathrm{SL}}_{c1}) & 0_{N_{\mathrm{Y}} \times N_{\mathrm{SL}}} \\ \\ 0_{N_{\mathrm{Y}} \times N_{\mathrm{SL}}} & \mathbf{V}^{\mathrm{h}}_{\mathrm{SL}}(\Phi^{\mathrm{SL}}_{c2}) \end{bmatrix} \tag{2.52}$$

$$\mathbf{V}^{\mathrm{h}}(\Phi) = \begin{bmatrix} \mathbf{V}^{\mathrm{h}}(\Phi_1, \Theta_{c1}) & 0_{N_{\mathrm{Y}} \times 1} & \mathbf{V}^{\mathrm{h}}(\Phi^{\mathrm{I}}_{c1}, \Theta_{c2}) & 0_{N_{\mathrm{Y}} \times 1} \\ \\ 0_{N_{\mathrm{Y}} \times 1} & \mathbf{V}^{\mathrm{h}}(\Phi_{c2}, \Theta_{c2}) & 0_{N_{\mathrm{Y}} \times 1} & \mathbf{V}^{\mathrm{h}}(\Phi^{\mathrm{I}}_{c2}, \Theta_{c2}) \end{bmatrix} \tag{2.53}$$

and $\mathbf{C} = [1 \quad 1 \quad \zeta \quad \zeta]^{\mathrm{T}}$. The set of angles defining the SL region, Φ^{SL}_c, and the corresponding array response vectors' matrix with respect to each beam, $\mathbf{V}^{\mathrm{h}}_{\mathrm{SL}}(\Phi^{\mathrm{SL}}_c)$, are expressed the same way as explained in Equation 2.35. The ML angular range $\pm\phi^{\mathrm{ML}}_c$ of the horizontal pattern is computed from the corresponding ideal 3GPP model horizontal pattern formula described by Equation 2.18

$$\phi^{\mathrm{ML}}_c = \pm\sqrt{\frac{SLA_{\mathrm{o}}}{12}} \cdot \Phi^c_{\mathrm{3dB}}, \quad \text{where:} \quad \Phi^{\mathrm{ML}}_c = \{\forall \phi : \phi \in \{\Phi_c + [-\phi^c_{\mathrm{ML}}, \ \phi^{\mathrm{ML}}_c]\}\} \tag{2.54}$$

$$\Phi^{\mathrm{SL}}_c = \{\forall \phi : \phi \in [-180°, 180°] \wedge \phi \notin \Phi^{\mathrm{ML}}_c\}, \tag{2.55}$$

and

$$\mathbf{V}^{\mathrm{h}}_{\mathrm{SL}}(\Phi^{\mathrm{SL}}_c) = [\mathbf{V}^{\mathrm{h}}(\phi_1, \Theta_c), \dots, \mathbf{V}^{\mathrm{h}}(\phi_{t_{\mathrm{SL}}}, \Theta_c)], \quad \text{for } \phi_{t_{\mathrm{SL}}} \in \Phi^{\mathrm{SL}}_c, \quad t_{\mathrm{SL}} = 1, \dots, \mathrm{N}_{\mathrm{SL}}, \tag{2.56}$$

Where $N_{\mathrm{ML}} = |\Phi^{\mathrm{ML}}_c|$ and $N_{\mathrm{SL}} = |\Phi^{\mathrm{SL}}_c|$. Solving Equation 2.51 applying Lagrangian technique, the solution takes the same closed form as shown in Equation 2.49 and it is given by

$$\mathbf{W}^{\mathrm{h}} = \frac{\mathrm{X}^{-1} \mathbf{V}^{\mathrm{h}}(\Phi) \mathbf{C}}{[\mathbf{V}^{\mathrm{h}}(\Phi)]^{H} \mathrm{X}^{-1} \mathbf{V}^{\mathrm{h}}(\Phi)} \tag{2.57}$$

$$\text{where} \quad X = \mathbf{V}^{\mathrm{h}}_{\mathrm{SL}}(\Phi^{\mathrm{SL}})[\mathbf{V}^{\mathrm{h}}_{\mathrm{SL}}(\Phi^{\mathrm{SL}})]^{\mathrm{H}}.$$

The designed azimuth pattern for the horizontal beams are depicted in Figure 2.6(a) where each beams are oriented with $\Phi_{c1} = -30°$ and $\Phi_{c2} = 30°$. Moreover, the combined 3D-beam pattern effect is well illustrated using the antenna gain values over the ground for all co-sited horizontally split cells in Figure 2.6(b).
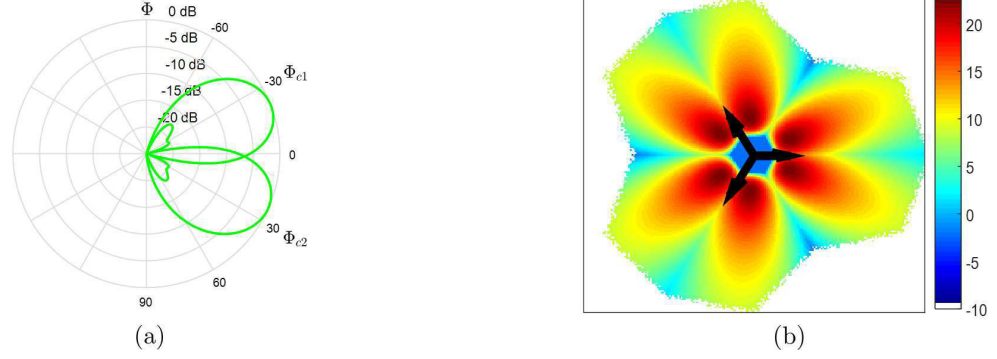
Figure 2.6. Horizontal Beams: (a)Azimuth Beam Pattern, (b)Antenna gain at ground level

2.4   Models of Average SINR and Throughput

This section describes the models used to compute the SINR and throughput performances.

The average Signal to Interference plus Noise Ratio (SINR) performance of UE u in the downlink defined over a single PRB when the UE is being served by a conventional-cell is described by γ_u,

$$\gamma_u = \frac{P^u_{s(u)}}{\sum\limits_{\substack{\forall c \in \mathcal{C} \\ c \neq s(u)}} \varsigma_c \cdot P^u_c + P_{\mathrm{N}}}, \qquad \text{for} \ \ l_{A(s(u))} = 0, \tag{2.58}$$

where P_{N} is the power of noise in dBm and $\varsigma_c \in [0, 1]$ is the interference load of cell c representing the fraction of spectrum being used for data transmission and as a result is interfering the system.

SINR threshold γ_{thr} is defined below which the instantaneous bit error probability (BEP) is higher than a specified tolerable level, in such cases, the corresponding UE is declared as in service outage [SA00].

When the conventional-cell is split in to two with either of the sectorization procedure, VS or HS, the underlying UEs will have to update their association to one of the new cells. The SINR of UE u after cell-splitting is described by γ'_u and its general expression including the co-channel interference between the new cells served by the same AAS, i.e.

$$\gamma'_u = \frac{P^u_{s(u)}}{\sum\limits_{\substack{\forall c \in \mathcal{C} \\ c \neq s(u) \land l_{A(c)} = 0}} \varsigma_c \cdot P^u_c \quad + \sum\limits_{\substack{\forall c \in \mathcal{C} \\ c \neq s(u) \land l_{A(c)} = 1}} \varsigma_c \cdot P^u_c \quad + \quad P_{\mathrm{N}}}, \qquad \text{for} \ \ l_{A(s(u))} = 1. \tag{2.59}$$

The achievable spectral efficiency of LTE downlink is approximated by means of a modified Shannon capacity formula incorporating additional correction factors attributed to the effective bandwidth Ω_{eff} used for data transmission. The signaling overhead related to the control channels and the SINR efficiency correction factor γ_{eff} that results from the applied Adaptive Coding and Modulation (ACM) scheme are taken into account [MNK+07]. Accordingly, the expression for the spectral efficiency denoted by $\mathcal{F}(\gamma_u)$ is

$$\mathcal{F}(\gamma_u) = \Omega_{\text{eff}} \cdot \log_2(1 + \frac{\gamma_u}{\gamma_{\text{eff}}}) \quad [\text{bits/s/Hz}] \tag{2.60}$$

The data throughput achieved in the downlink over a single PRB of bandwidth Ω_{PRB} given in kHz can, therefore, be expressed as τ_u^{PRB}

$$\tau_u^{\text{PRB}} = \Omega_{\text{PRB}} \cdot \mathcal{F}(\gamma_u) \quad [\text{bps}]. \tag{2.61}$$

Since the radio resource allocation granularity in LTE is on a PRB base, the downlink throughput performance of UE u designated by τ_u is determined by the fraction of resource share assigned to the user, i.e. R_u.

$$\tau_u = R_u \cdot M_{\text{PRB}} \cdot \tau_u^{\text{PRB}} \quad [\text{bps}]. \tag{2.62}$$

2.5 Models of User Traffic and Radio Resource Allocation

In this section, the type of user traffic model assumed and the employed resource allocation strategy is discussed.

A full buffer traffic model where the base station have always data to transmit for all users in the cell is adopted for this study [CLW+15]. With this traffic model assumption, the whole PRB of a cell is used when there is at least one UE, hence, the load used for interference calculation is

$$\varsigma_c = \begin{cases} 1, & \{\exists u | s(u) = c\} \\ 0, & \text{otherwise}. \end{cases} \tag{2.63}$$

In addition, this traffic model is characterized by having on average a constant number of UEs in the serving cell where the UEs are competing each other for the radio resource during scheduling [AWNO+12, CLW+15]. The resource allocation at each cell is performed in a proportional fair (PF) manner. The PF allocation strategy is applied in such away that it maximizes the sum of the logarithmic average data rate of

all users being served by the cell, i.e. $\sum_u \log(\tau_u)$ [KH05]. Thus, the resource fraction set $\mathcal{R}_c = \{R_u\}$ of the PF scheduler at cell c is obtained from the following resource allocation problem:

$$R_u = \underset{R_u}{\operatorname{argmax}} \sum_{\substack{u \\ s(u)=c}} \log(R_u \cdot M_{\text{PRB}} \cdot \tau_u^{\text{PRB}}), \qquad \text{subject to :} \qquad \sum_{\substack{u \\ s(u)=c}} R_u = 1. \quad (2.64)$$

Solving Equation 2.64 [KH05] [RC09] yields a resource fair allocation strategy that guarantees equal fraction of resource for each UE. As a result, R_u becomes:

$$R_u = \frac{1}{N_c^{\text{u}}}, \qquad \{\forall u | s(u) = c\} \tag{2.65}$$

where $N_c^{\text{u}} = |\mathcal{A}_c|$ is the total number of users connected to serving cell c. It has been demonstrated in [HT09] that a proportional fair allocation, from throughput perspective, with equal resource scheduling maximizes both the cell and average user throughput performance.

2.6 Definition of Cell Load and Available Capacity

This section presents the definitions used to describe the load situation of a cell and the remaining available capacity.

In this thesis, the cell load definition is associated to the percent PRB utilization. Therefore, the load of cell c $\Lambda_c \in [0, 1]$ is defined as the sum of the fraction of resources required to satisfy all the connected UEs with a minimum acceptable target throughput performance τ_{target}. In fact the actual PRB utilization of a cell, if there is at least one UE connected, is always 100% (assuming worst case scenario) and τ_u defined by Equation 2.62 is the maximum achievable throughput. This is due to the fact that the resource-fair based PF scheduler assigns all the available PRBs to the connected UEs under service. Assuming the minimum fraction of PRB required by UE u to achieve the defined τ_{target} is R_u^{min}, Λ_c is expressed as

$$\Lambda_c = \sum_{\substack{u \\ s(u)=c}} \min\{R_u, R_u^{\text{min}}\}, \quad \text{where} \quad R_u^{\text{min}} = \frac{R_u \cdot \tau_{\text{target}}}{\tau_u}. \tag{2.66}$$

Λ_c will be used only to describe the capacity of the cell to figure out whether it can still accommodate additional load while on average satisfying the minimum target performance.

Having the Λ_c value, the amount of the remaining cell capacity available at the cell is evaluated assuming a certain peak load threshold Λ_c^{peak} above which cell load should

not be exceeded, i.e. $\Lambda_c^{\text{peak}} \leq 1$, is termed as the available capacity (AC) of the cell that can be used to handle additional traffic [3GP10]. The AC of cell c denoted by AC_c is described as the underutilized fraction of the radio resource and is computed as

$$AC_c = \max\{0, \Lambda_c^{\text{peak}} - \Lambda_c\}. \tag{2.67}$$

2.7   Definitions of Performance Evaluation Metrics

This section discusses the definitions of the performance evaluation metrics used through out the thesis.

The throughput achieved by a UE or the cell throughput are the key performance indicators utilized in the analysis of the sectorization performance. In general, the performance evaluation is carried out based on the analysis of UE throughput (TP) statistics collected from a particular coverage area $\mathcal{A} = \{u\}$ described by $\mathcal{T}_\mathcal{A}$, i.e. $\mathcal{T}_\mathcal{A} = \{\tau_u | u \in \mathcal{A}\}$. Given the probability density function (PDF) of τ_u in $\mathcal{T}_\mathcal{A}$ by $f_\mathcal{A}^{\text{TP}}(\tau_u)$ and its corresponding cumulative distribution function (CDF) by $F_\mathcal{A}^{\text{TP}}(\tau_u)$, the ϖ percentile value of the CDF ($\text{TP}_\mathcal{A}^{\varpi\%}$) where $\varpi \in [0, 100]$, arithmetic mean ($\text{TP}_\mathcal{A}^{\text{mean}}$) and harmonic mean ($\text{TP}_\mathcal{A}^{\text{HM}}$) of the UE throughput metrics are evaluated as

$$\text{TP}_\mathcal{A}^{\varpi\%} = \inf\{\tau_u \in \mathcal{T}_\mathcal{A} | F_\mathcal{A}^{\text{TP}}(\tau_u) > \frac{\varpi}{100}\}, \tag{2.68}$$

$$\text{TP}_\mathcal{A}^{\text{avg}} = \frac{1}{|\mathcal{T}_\mathcal{A}|} \cdot \sum_{\substack{u \\ u \in \mathcal{A}}} \tau_u, \quad \text{and} \quad \text{TP}_\mathcal{A}^{\text{HM}} = \frac{|\mathcal{T}_\mathcal{A}|}{\sum_{\substack{u \\ u \in \mathcal{A}}} \frac{1}{\tau_u}}. \tag{2.69}$$

2.8   Scenario Description and Simulation Parameters

This section presents the description of the scenarios used for system level simulation and the parameter settings used in the considered 3GPP and RT-3D cellular models.

A Matalb based discrete event system level simulator is used for the analysis and evaluation of the system performance. The LTE downlink transmission is studied considering uniform and non-uniform spatial user distribution cases. The deployment layout and BS site positioning are as shown in Figure 2.1 and 2.2. In the simulation scenarios,

Table 2.1. Simulation parameter settings

Description	Parameter	Value
Site	ISD	1732 m
	# Site	7 Tri-sectored
	Height [m]	Antenna =30, UE = 1.5
Antenna	Gain[dBi]	19.5/16
	$\Phi_{3\text{dB}}$	62°
	$\Theta_{3\text{dB}}$	5°/10°
	Side and Backward Attenuation	2o dB
Propagation	Pathloss	$128.1 + 37.6 \cdot \log_{10}(d_{c,u})$
	Shadowing Std.	8 dB
	Shadowing corr. b/n horizontal cells.	0.5
	Shadowing corr. b/n vertical cells.	0.5
	Penetration Loss	20 dB
User Traffic	UE Distribution	Uniform/Non-uniform
	Traffic-type	Full buffer
	UE speed: Fast/Slow	60 / 3 km/h
	Target data rate (τ_{target})	1000 Kbps
Resource allocation	Scheduler	proportional-resource fair
	Max PRB utilization (Λ_c^{peak})	0.8
	Target data rate (τ_{target})	1000 Kbps
System Setting	RAT-Type	LTE
	Frequency	2 GHz
	Bandwidth	10 MHz
	Operating Mode	Down-Link
MRO Settings	MRO Optimization	Intra-RAT,Intra-Frequency
	Simulation time-step	50 ms
	KPI collection period	90 s
	Ping-Pong weight	0.2
Algorithm thresh-olds	load (Λ_c^{thr})	0.8
	δ_a	2.5
	δ_{c1}, δ_{c2}	-1
	Time window (t_{w})	100 time-steps

both stationary and moving users are considered to properly capture the impact of dynamic load variation in the network and investigate mobility related handover aspects. Two kinds of user mobility are assumed. Some of the users are traveling randomly in the network while others are moving on streets along a specified path with different speeds. The street design and traveling paths for the 3GPP model can be referred in [KWVK15] where as for the RT-scenario, the streets in the 3D model as illustrated in Figure 2.2 are applied. The employed simulation parameters and the corresponding settings are summarized and presented in Table 2.1.

Chapter 3

Tilt Dependent Shadowing Model

3.1 Introduction

Motivated by the deficiencies of the existing 2D propagation model which assumes a stationary propagation characteristics in the elevation domain, a new shadowing model is developed [Sin15]. Considering dynamic beam steering as one of the case-scenarios of AAS-based deployment, the new shadowing model incorporates elevation tilt angle to capture the effect of the relative clutter variation that can be experienced while the elevation orientation of the serving beam is altered in a scatter-rich urban environment. The investigation to ascertain the tilt dependency of the shadowing is carried out by means of statistical analysis of RT-based based predicted radio propagation data from a realistic 3D-urban clutter model described in Section 2.2.2. Based on the analysis, tilt-dependent shadowing model has been developed which is required for the detailed studies of dynamic AAS-based deployments.

The organization of this chapter is as follows. The motivation for studying the shadowing model is discussed briefly in Section 3.2. In Section 3.3, the RT-propagation data analysis and the essential propagation parameter extraction procedures are presented. The impact of tilt variation on the statistical behavior of the the shadowing effect is explored and related analysis are provided in Section 3.4. The modeling of the new tilt-dependent shadowing is presented in Section 3.4.1. The last section of the chapter, Section 3.5, compares and evaluates the performance of the developed model.

3.2 Motivation

This section discusses the motivation for the study presented in this chapter of the thesis.

Figure (3.1) illustrates different propagation paths of the dominant (strongest) signal from a cell beam for two tilt configuration settings assuming a 3D propagation scattering objects. Although the channel between BS and UE is three-dimensional in nature, as shown in Figure (3.1), the existing propagation shadowing model omits the channel
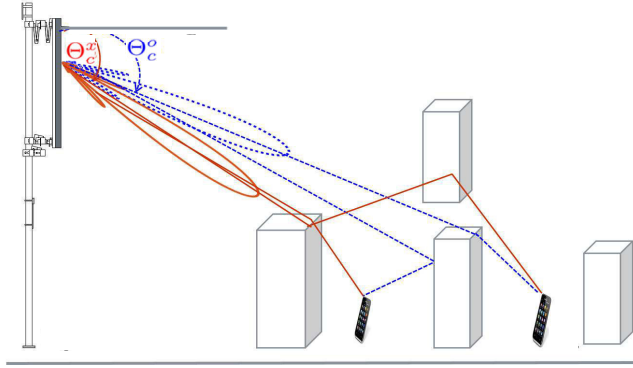
Figure 3.1. Elevation tilt changes and dominant signal paths in 3D model

behavior in the elevation dimension, as shown in Equation (2.7). In Equation (2.7), the impact of the propagation obstacles in the vicinity of the BS and the user terminal are considered only as a function of their relative 2D spatial location. Hence, when the elevation tilt setting Θ_c of a beam serving cell $c \in \mathcal{C}$ is changed, the value of the distance dependent path loss $L_\mathrm{p}(d_{c,u})$ as well as the shadowing $\widehat{S_c^u}$ with respect to UE u are assumed to remain constant. The effect of the tilt change is accounted by the impact of the modified beam pattern orientation changing the antenna gain value in the respective UE direction, $G_c^u(\Phi_c, \Theta_c)$ [G.11, 3GP13a]. Given $\vartheta_c = \{\Theta_c^x, x = 1, \ldots, N_{\Theta_c}\}$ is a set of N_{Θ_c} different tilt settings of cell c where $N_{\Theta_c} = |\vartheta_c|$, and $\Theta_c^o \in \vartheta_c$ is a reference tilt setting, the overall signal attenuation $h_c^u(\Phi_c, \Theta_c^x)$ after the tilt is altered from Θ_c^o to Θ_c^x, according to Equation (2.21), is expressed as

$$h_c^u(\Phi_c, \Theta_c^x) = G_c^u(\Phi_c, \Theta_c^x) \cdot L_\mathrm{p}(d_{c,u}) \cdot 10^{\frac{\widehat{S_c^u}}{10}}, \tag{3.1}$$

$$= h_c^u(\Phi_c, \Theta_c^o) \cdot \frac{G_c^u(\Phi_c, \Theta_c^x)}{G_c^u(\Phi_c, \Theta_c^o)}. \tag{3.2}$$

Being modeled only as a location dependent, $\widehat{S_c^u}$, in Equation (2.7) assumes that the behavior of the radio channel with respect to the same UE location is invariant and the shadowing fading values before and after the tilt change are statistically fully correlated. As can be seen in Figure (3.1), the assumption of shadowing invariability with respect to tilt change might be valid in propagation environment characterized by a low-scattering behavior or in a transmission having a Line-Of-Sight (LOS) situation. However, this assumption is rather questionable in a typical urban clutter case where LOS probability is very low. In order to procure certainty whether the shadowing fading maintains full statistical correlation or not with tilt change $\Delta\Theta_c^x = |\Theta_c^x - \Theta_c^o|$, an analysis has been carried out on tilt-specific propagation maps generated in the RT-based 3D model. Characterizing the shadowing behavior with respect to antenna tilt

variation is essential in this thesis for the upcoming detailed investigation of network capacity in AAS-enabled deployments.

3.3 Ray-Tracing Data Analysis and Propagation Parameter Extraction

3.3.1 Introduction

This section presents the details of the analysis carried out on the tilt-specific propagation maps, $\mathcal{P}_c(\Theta_c^x)$, obtained from the RT-scenario and the procedures employed to extract propagation parameters from the respective maps.

Given P_c^{tx} is the transmitted power from each sector-antenna to serve cell c during the prediction in Section 2.2.2, with post-prediction processing on the elements of the set $\mathcal{P}_c(\Theta_c^x)$, the overall signal attenuation $h_c^u(\Phi_c, \Theta_c^x)$ with respect to each prediction pixel location u for specific tilt setting Θ_c^x is computed to obtain the set $\mathcal{H}_c(\Theta_c^x)$ of $h_c^u(\Phi_c, \Theta_c^x)$ from the total prediction area,

$$\mathcal{H}_c(\Theta_c^x) = \{h_c^u(\Phi_c, \Theta_c^x) : h_c^u(\Phi_c, \Theta_c^x) = \frac{P_c^u}{P_c^{\mathrm{tx}}} \wedge P_c^u \in \mathcal{P}_c(\Theta_c^x)\}. \tag{3.3}$$

The signal power loss in free space and LOS propagation is determined only by distance it traveled. In non-LOS (NLOS) case, however, the distance dependent path loss underlays additional variation owing to the presence of propagation obstacles between the transmitter and the receiver. In case of beamforming, the radio signal power is concentrated in a specific direction to achieve additional antenna gain $G_c^u(\Phi_c, \Theta_c^x)$. Since $G_c^u(\Phi_c, \Theta_c^x)$ which is defined by the beam pattern, its effect should be excluded from the $h_c^u(\Phi_c, \Theta_c^x)$ value. Accordingly, the total tilt-specific propagation loss excluding the antenna gain effect, henceforth, described by $L_{\mathrm{T}}^u(d_{c,u}, \Theta_c^x)$ is computed as

$$L_{\mathrm{T}}^u(d_{c,u}, \Theta_c^x) = \frac{h_c^u(\Phi_c, \Theta_c^x)}{G_c^u(\Phi_c, \Theta_c^x)}. \tag{3.4}$$

Various studies on propagation channel characterization and modeling based on real measurement statistics have confirmed that the $L_{\mathrm{T}}^u(d_{c,u}, \Theta_c^x)$ values for UEs located at equal distance $d_{u,c} = d$ from the BS serving cell c are randomly fluctuating around a distance dependent local mean value the same as the path loss [E.99, G.11]. This signal fluctuation is having a log-normal statistical variation and is attributed to the shadowing phenomenon [G.11]. In the considered RT-scenario, the impact of fast fading

is not included as multi-path effect does not exist with the employed DPM model and the prediction pixel points are stationary. The value of $L_{\mathrm{T}}^u(d_{c,u}, \Theta_c^x)$ in dB scale, i.e. $\widehat{L_{\mathrm{T}}^u}(d_{c,u}, \Theta_c^x) = 10 \cdot \log_{10}(L_{\mathrm{T}}^u(d_{c,u}, \Theta_c^x))$ for all UEs located at distance $d_{u,c} = d$, therefore, follows normal statistical distribution with a mean value the same as the clutter-specific distance dependent path loss $\widehat{L_{\mathrm{p}}^u}(d_{c,u}) = 10 \cdot \log_{10}(L_{\mathrm{p}}^u(d_{c,u}))$ and standard deviation equal to that of the shadowing fading. Hence, the PDF of $\widehat{L_{\mathrm{T}}^u}(d_{c,u}, \Theta_c^x)$ is expressed as

$$f_{\mathrm{PL}}(\widehat{L_{\mathrm{T}}^u}(d, \Theta_c^x)) = \frac{1}{\sigma_{\mathrm{s}} \cdot \sqrt{2 \cdot \pi}} \cdot \exp - \left(\frac{\widehat{L_{\mathrm{T}}^u}(d_{c,u}, \Theta_c^x) - \widehat{L_{\mathrm{p}}^u}(d)}{\sqrt{2} \cdot \sigma_{\mathrm{s}}} \right)^2, \text{where} \tag{3.5}$$

$$\widehat{L_{\mathrm{p}}^u}(d) = \mathrm{E}\Big[\mathcal{L}_c(d, \Theta_c^x) \Big], \tag{3.6}$$

$$\sigma_{\mathrm{s}}^2 = \mathrm{Var}\Big[\mathcal{L}_c(d, \Theta_c^x) \Big], \tag{3.7}$$

$$\mathcal{L}_c(d, \Theta_c^x) = \left\{ \widehat{L_{\mathrm{T}}^u}(d, \Theta_c^x) : \forall u \in \mathcal{A}_{\mathrm{P}} \wedge d_{u,c} = d \right\}. \tag{3.8}$$

Based on the general PDF expression shown by Equation (3.5), and the relationship defined in Equation (3.1) and Equation (3.4), the tilt-specific shadowing component of $\widehat{L_{\mathrm{T}}^u}(d_{c,u}, \Theta_c^x)$ described by $\widehat{S_c^u}(\Theta_c^x)$ is extracted by excluding the distance dependent path loss component, i.e.

$$\widehat{S_c^u}(\Theta_c^x) = \widehat{L_{\mathrm{T}}^u}(d_{c,u}, \Theta_c^x) - \widehat{L_{\mathrm{p}}^u}(d_{c,u}). \tag{3.9}$$

3.3.2   Empirical Path loss Model

In this section, the modeling of the site-specific path loss to be used to extract the shadowing fading values from the $\widehat{L_{\mathrm{T}}^u}(d_{c,u}, \Theta_c^x)$ statistics is presented.

Extracting $\widehat{S_c^u}(\Theta_c^x)$ as specified in Equation (3.9) requires accurate approximation of the distance dependent path loss component. Empirical path loss modeling involves prediction of the coefficients described by the general path loss model expression in Equation (2.4). Since the path loss coefficients Υ and ϱ are characteristics of the propagation environment, they reflect the clutter behavior observed between the BS and the UE [E.99, G.11]. Having a one dimensional distance dependent projection of $\widehat{L_{\mathrm{T}}^u}(d_{c,u}, \Theta_c^x)$, the values of Υ and ϱ can be predicted empirically by employing a linear regression technique. Figure (3.2) illustrates $\widehat{L_{\mathrm{T}}^u}(d_{c,u}, \Theta_c^x)$ values for $\forall u \in \mathcal{A}_{\mathrm{P}}$ as a function of the logarithm of the path loss distance, $10 \cdot \log_{10}(d_{c,u})$, for an exemplary cell c. Υ and ϱ are computed as parameters of a best-fitting linear curve to the set of
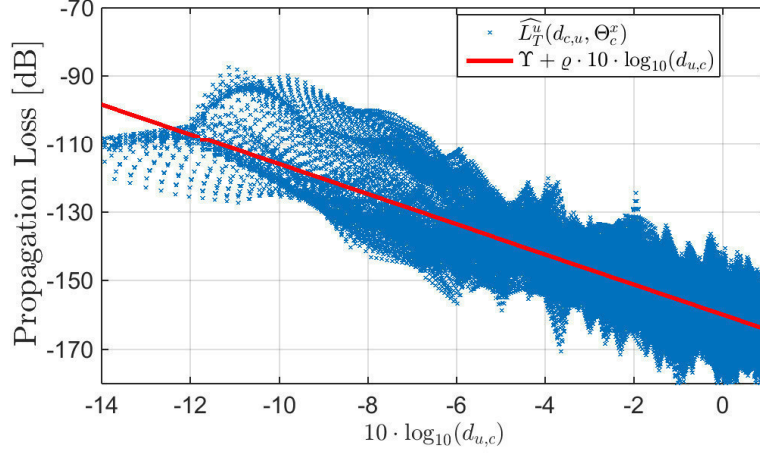
Figure 3.2. Total propagation loss statistics and path loss coefficients prediction

$\widehat{L_{\mathrm{T}}^u}(d_{c,u}, \Theta_c^x)$ values. The optimal coefficient values minimize the sum of the squares of the offsets of the points from the fitting curve and the fitting criteria is expressed as

$$\underset{\Upsilon,\ \varrho}{\mathrm{argmin}} \sum_{\substack{\Theta_c^x \\ \Theta_c^x \in \vartheta_c}} \sum_{\substack{u \\ u \in \mathcal{A}_{\mathrm{P}}}} \left(\widehat{L_{\mathrm{T}}^u}(d_{c,u}, \Theta_c^x) - \left(\Upsilon + \varrho \cdot 10 \cdot \log_{10}(d_{u,q}) \right) \right)^2. \tag{3.10}$$

The clutter-specific path loss coefficients Υ and ϱ are determined based on the assumption that they depend only on the path loss distance $d_{u,c}$, hence, are valid for the same cell irrespective of the tilt setting.

3.3.3 Extraction of Shadowing Fading Statistics

This sections explains the shadowing fading statistics extraction scheme and the joint optimization technique employed to predict the path loss coefficients and antenna radiation pattern parameters.

Having the appropriate path loss characterization model described by Equation (3.10), the extraction of tilt-specific shadowing fading component, as discussed in Equation 3.9, needs to exclude the 3D antenna gain pattern effect from $h_c^u(\Phi_c, \Theta_c^x)$ as shown by Equation (3.4) so that the normal statistical distribution assumption of $\widehat{L_{\mathrm{T}}^u}(d_{c,u}, \Theta_c^x)$ described by Equation (3.5) remains valid. Combining Equation (3.4), Equation (3.9) and Equation (3.10), the shadowing fading statistics extraction is reformulated. Given $\widehat{h_c^u}(\Phi_c, \Theta_c^x)$ and $\widehat{G_c^u}(\Phi_c, \Theta_c^x)$ are the total propagation loss and antenna gain pattern in dB scale, the tilt-specific shadowing $\widehat{S_c^u}(\Theta_c^x)$ is extracted as

$$\widehat{\underset{\sim}{S_c^u}}(\Theta_c^x) = \widehat{h_c^u}(\Phi_c, \Theta_c^x) - \widehat{G_c^u}(\Phi_c, \Theta_c^x) - (\Upsilon + \varrho \cdot 10 \cdot \log_{10}(d_{u,q})), \tag{3.11}$$

A tilt-specific shadow map denoted by $\widehat{\mathcal{S}}_c^u(\Theta_c^x)$ is created for each cell as a set of the extracted $\widehat{S_c^u}(\Theta_c^x)$ values from the whole prediction area, $\mathcal{A}_\mathrm{P}$, i.e.,

$$\widehat{\mathcal{S}}_c^u(\Theta_c^x) = \{\widehat{S_c^u}(\Theta_c^x) : \forall u \in u \in \mathcal{A}_\mathrm{P}\}. \tag{3.12}$$

The antenna gain term, $\widehat{G_c^u}(\Phi_c, \Theta_c^x)$, in Equation (3.11), is determined by the respective 3D beam pattern value. As demonstrated in [3D09], the ML pattern can be modeled analytically using the conventional approach provided by the 3GPP beam pattern model explained in Section 2.2.1.3. However, the antenna gains in the direction of the side and back lobes, which in reality are highly impacted by the rooftop or the surroundings where the BS antenna is mounted, are difficult to predict, hence, typically approximated with a fixed backward attenuation (BA) factor [EL00]. As a consequence, it is hardly possible to derive accurate analytical expression of the antenna gain pattern effect outside the ML region.

3GPP beam pattern model proposes to use average BA value BA_o to characterize this effect as explained in Equation (2.15). Hence, the prediction of the path loss coefficients from in Equation (3.10) heavily depends on the value of BA_o as well, see Equation (3.4). Furthermore, following the condition that $\widehat{S_c^u}(\Theta_c^x)$ is normally distributed, the beam pattern parameters should yield a shadowing with a mean around zero and minimum standard deviation, as described in Equation (3.5) and Equation (3.9) [G.11]. Therefore, a joint optimization of $BA_\mathrm{o}, A_\mathrm{L}, \Upsilon$ and ϱ parameters is applied based on Equation (3.10) with target of extracting shadowing fading statistics with minimum standard deviation. The cost function for the optimization problem is described by $F_{\sigma_\mathrm{s}}(BA_\mathrm{o}, \Upsilon, \varrho)$, where

$$F_{\sigma_\mathrm{s}}(BA_\mathrm{o}, \Upsilon, \varrho) = \sqrt{\mathrm{Var}[\widehat{\mathcal{S}}_c^u(\Theta_c^x)]}, \tag{3.13}$$

$$\underset{BA_\mathrm{o}, \Upsilon, \varrho}{\mathrm{argmin}} \quad F_{\sigma_\mathrm{s}}(BA_\mathrm{o}, \Upsilon, \varrho). \tag{3.14}$$

Even though the value of BA_o widely used in system level simulation is 20 dB [3GP13a], in reality, its different to specific site and the value can vary within ranges depending on the clutter type between BS and UE.

For the joint optimization, a set of possible values of $BA_\mathrm{o} \in \mathcal{B}$ is considered. The size of the search space in $\mathcal{B}$ is limited and very small,hence, a brute-force approach is employed to determine the global optimal values of BA_o, Υ, and ϱ using Algorithm 1. The algorithm iteratively predicts the path loss coefficients for different BA_o settings with the objective of extracting the shadowing values where $F_{\sigma_\mathrm{s}}(BA_\mathrm{o}, \Upsilon, \varrho)$ is evaluated. The optimal values of $(BA_\mathrm{o}, \Upsilon, \varrho)$ are the tuples for which $F_{\sigma_\mathrm{s}}(BA_\mathrm{o}, \Upsilon, \varrho)$ is minimum.

Algorithm 1 :Path loss coefficients prediction and Shadowing fading statistics extraction

---

1: `Initialize:` $\iota \leftarrow 1$
2: **while** $\iota \leq |\mathcal{B}|$ **do**
3:     Compute Gain: $\widehat{G_c^u}(\Phi_c, \Theta_c^x)$ using $\mathcal{B}(\iota)$
4:     Exclude Gain : $\widehat{L_T^u}(d_{c,u}, \Theta_c^x) \leftarrow \widehat{h_c^u}(\Phi_c, \Theta_c^x) - \widehat{G_c^u}(\Phi_c, \Theta_c^x)$
5:     Regression on $\bigcup\limits_{\forall \Theta_c^x | \Theta_c^x \in \vartheta_c} \mathcal{L}_c(d_{u_c}, \Theta_c^x)$ and find $(\Upsilon^\iota, \text{ and } \varrho^\iota)$
6:     Extract Shadow Map: $\widehat{\mathcal{S}_c^u}(\Theta_c^x)$
7:     Compute Shadowing standard deviation: $\sigma_\iota = \sqrt{\text{Var}[\widehat{\mathcal{S}_c^u}(\Theta_c^x)]}$
8:     **if** $\iota = 1$ **then**
9:         $\underline{\sigma}_s \leftarrow \sigma_\iota$
10:    **else**
11:        **if** $\sigma_\iota < \underline{\sigma}_s$ **then**
12:            $\underline{\sigma}_s \leftarrow \sigma_\iota$
13:            $\Upsilon \leftarrow \Upsilon^\iota$
14:            $\varrho \leftarrow \varrho^\iota$
15:        **end if**
16:    **end if**
17: **end while**

In order to validate the proposed path loss coefficients prediction approach and to rely on the statistical behavior of the extracted shadowing data, the same procedure has been carried out on propagation map data generated by 3GPP-scenario using path loss offset and exponent value of 128.1 and 3.76, respectively. As demonstrated in Figure

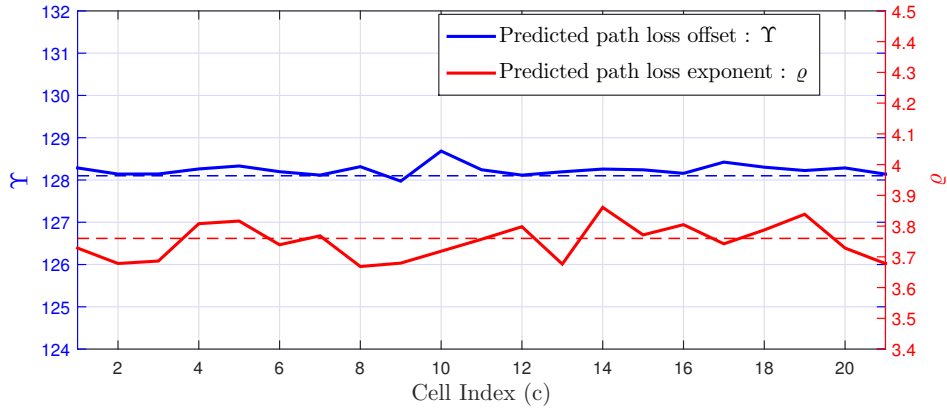Figure 3.3. 3GPP-Scenario: Predicted Path loss Coefficients

3.3, the applied path loss prediction method has been able to predict the actual values of the path loss coefficients which have been used to generate the shadowing map. This can be used as a proof of the concept of the applied path loss parameter prediction method and shadowing extraction technique. The corresponding predicted values of Υ,

and ϱ for the RT-scenario using Algorithm 1 are depicted in Figure 3.4 for all cells. It has been observed the predicted coefficients are considerably different even for co-sited cells depending on the clutter behavior observed in the orientation of the beam serving the cell.
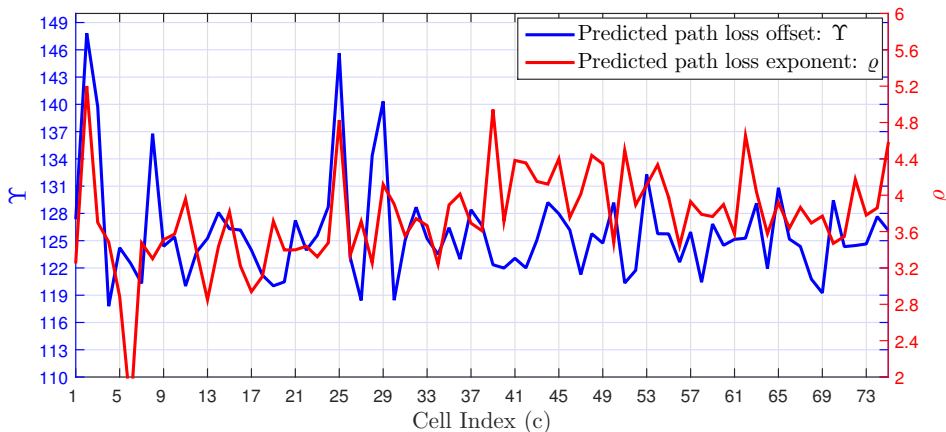

Figure 3.4. RT-Scenario: Predicted Path loss coefficients

3.4 Analysis of Impact of Tilt on Shadowing

In this section, the impact of tilt setting variation on the statistical behavior of the shadowing fading is analyzed based on the tilt-specific shadowing maps $\widehat{\mathcal{S}}_c^u(\Theta_c^x)$ extracted using Algorithm 1.

As depicted in Figure 3.16 and Figure 3.5, the extracted shadowing values for different tilt setting seem to remain the same having identical distribution evincing invariable mean and variance. This is evident that the statistical distribution only is not able to clearly reflect the impact of the tilt setting change on the shadowing behavior, i.e,

$$\mathrm{E}\!\left[\widehat{\mathcal{S}}_c^u(\Theta_c^x)\right] = \mathrm{E}\!\left[\widehat{\mathcal{S}}_c^u(\Theta_c^o)\right] \approx 0 \quad \text{and,} \tag{3.15}$$

$$\mathrm{Var}\!\left[\widehat{\mathcal{S}}_c^u(\Theta_c^x)\right] = \mathrm{Var}\!\left[\widehat{\mathcal{S}}_c^u(\Theta_c^o)\right] \approx \sigma_{\mathrm{s}}^2. \tag{3.16}$$

In fact, the shadowing effect is not deterministic in its nature rather random. Therefore, any disparity between the shadowing values with respect to a dedicated UE location at two different tilt settings can be captured by investigating their statistical inter-dependency. Extensive analysis and study results presented by the thesis author in [KGW⁺14, KWVK13] reveal that the shadowing values are indeed altered when tilt
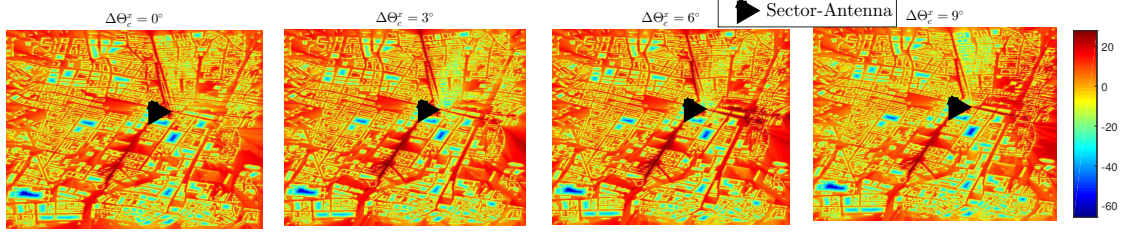
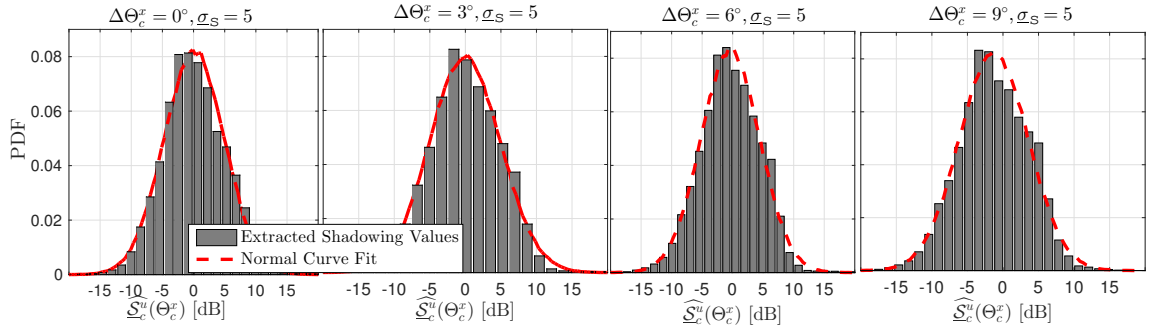Figure 3.5. Extracted tilt-specific shadowing map

Figure 3.6. Extracted shadow fading statistical distribution

configuration is varied. Moreover, the statistical inter-dependency between the shadowing values is found to decrease and becomes loose when the applied tilt difference gets higher. Such shadowing variability behavior with respect to tilt change $\Delta\Theta_c^x = \Theta_c^x - \Theta_c^o$ can be measured and characterized by analyzing the statistical cross-correlation property of two tilt-specific shadowing maps. Accordingly, for the tilt setting change from Θ_c^o to Θ_c^x, the cross-correlation coefficient $\rho_c^{\Theta_c^x, \Theta_c^o}$ of $\widehat{\mathcal{S}_c^u}(\Theta_c^x)$ and $\widehat{\mathcal{S}_c^u}(\Theta_c^o)$ is utilized

$$\rho_c^{\Theta_c^x, \Theta_c^o} = \frac{\mathrm{E}\left[\widehat{\mathcal{S}_c^u}(\Theta_c^x) \cdot \widehat{\mathcal{S}_c^u}(\Theta_c^o)\right]}{\underline{\sigma}_{\mathrm{s}}^2} \tag{3.17}$$

In addition to $\rho_c^{\Theta_c^x, \Theta_c^o}$, the difference of the shadowing values $\Delta\widehat{\mathcal{S}_c^u}(\Theta_c^x, \Theta_c^o)$ evaluated at each UE location is of interest for further characterization of the shadowing variability. $\Delta\widehat{\mathcal{S}_c^u}(\Theta_c^x, \Theta_c^o)$ is computed as

$$\Delta\widehat{\mathcal{S}_c^u}(\Theta_c^x, \Theta_c^o) = \widehat{\mathcal{S}_c^u}(\Theta_c^x) - \widehat{\mathcal{S}_c^u}(\Theta_c^o). \tag{3.18}$$

The values of $\widehat{\mathcal{S}_c^u}(\Theta_c^x, \Theta_c^o)$ over network wide area are illustrated in Figure (3.7) where the existence of shadowing variability is evident. The statistical distribution curves of $\widehat{\mathcal{S}_c^u}(\Theta_c^x, \Theta_c^o)$ are shown in Figure (3.8) for different $\Delta\Theta_c^x$ where different mean and variance are reported. Since the distribution of a linearly combined normally distributed random variables remains normal [Hay12], $\Delta\widehat{\mathcal{S}_c^u}(\Theta_c^x, \Theta_c^o)$ expressed in Equation (3.18)

can be modeled as normally distributed whose mean and variance depends on the amount of the introduced $\Delta\Theta_c^x$. This is demonstrated in Figure (3.8).
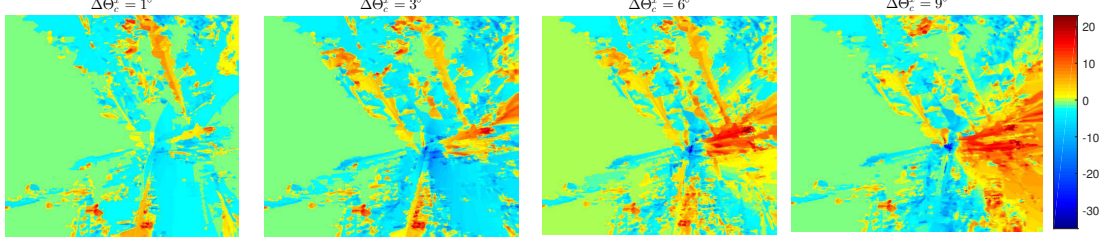
Figure 3.7. Extracted shadow fading difference values
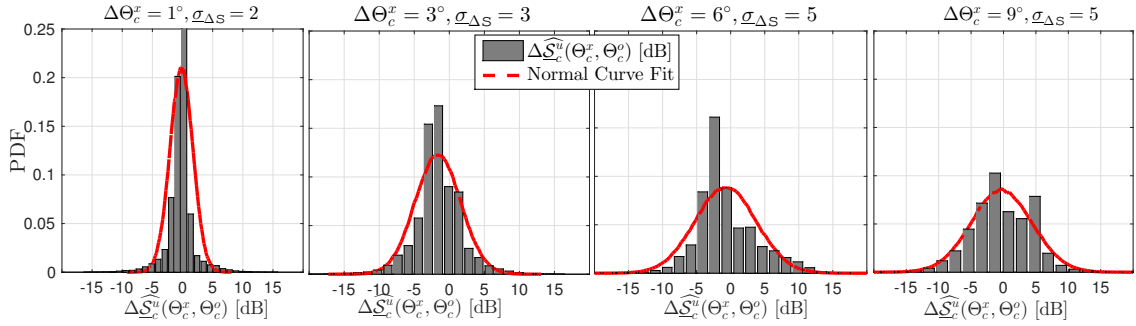
Figure 3.8. Extracted shadow fading difference distribution

The variance $\sigma_{\Delta s}^2(\Delta\Theta_c^x)$ of $\Delta\widehat{S_c^u}(\Theta_c^x, \Theta_c^o)$ can be used to measure the local variation the random shadowing effect or the de-correlation of the shadowing with respect to $\Delta\Theta_c^x$. For $0 < \rho_c^{\Theta_c^x, \Theta_c^o} \leq 1$, $\sigma_{\Delta s}^2(\Delta\Theta_c^x)$ value depends not only on the variance of the shadowing difference itself but also on the covariance property of the shadowing statistics before and after the tilt change. This is illustrated in Figure 3.8 where the statistical distribution of $\Delta\widehat{S_c^u}(\Theta_c^x, \Theta_c^o)$ confirms a normal distribution with a mean around zero and a variance that increases proportional to the applied $\Delta\Theta_c^x$, i.e. as the statistical inter-dependency decreases. This can be justified with the following relationship

$$\sigma_{\Delta s}^2(\Delta\Theta_c^x) = \mathrm{E}\left[\ (\widehat{S_c^u}(\Theta_c^x) - \widehat{S_c^u}(\Theta_c^o))^2\right] \tag{3.19}$$

$$= 2 \cdot (\sigma_s^2 - \mathrm{E}\left[\widehat{S_c^u}(\Theta_c^x) \cdot \widehat{S_c^u}(\Theta_c^o)\right]) \tag{3.20}$$

then,

$$\sigma_{\Delta s}(\Delta\Theta_x) = \sigma_s \cdot \sqrt{2 \cdot (1 - \rho_c^{\Theta_c^x, \Theta_c^o})} \tag{3.21}$$

Based on Equation (3.21), when statistical correlation level decreases, i.e. higher $\rho_c^{\Theta_c^x, \Theta_c^o}$, the variance value increases. Apart from the correlation coefficient, the severity of the

shadowing variability mainly depends on the propagation environment itself which is characterized by a typical shadowing standard deviation, $\underline{\sigma}_s$. Consequently, $\underline{\sigma}^2_{\Delta s}(\Delta\Theta^x_c)$ that describes the shadowing variation with $\Delta\Theta^x_c$ becomes more critical in a dense urban scenario which is intrinsically characterized by high $\underline{\sigma}_s$. This is explained by Equation (3.21) and clearly illustrated in Figure (3.9). For this reason, the parameters $\underline{\sigma}_{\Delta s}(\Delta\Theta_x)$ and $\rho^{\Theta^x_c,\Theta^o_c}_c$ build the basis for the measure of the statistical variability of the shadowing fading with respect to tilt setting change.
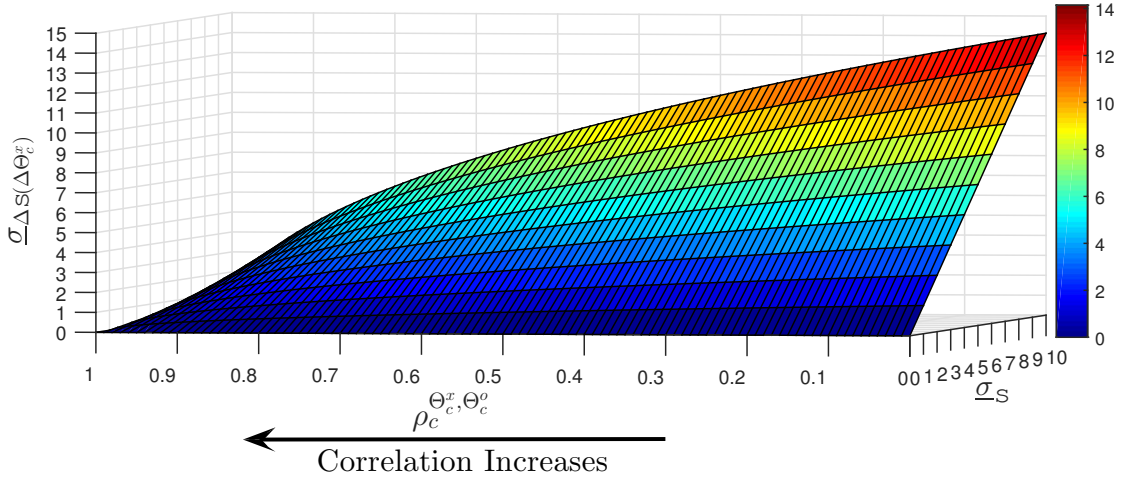
Figure 3.9. Standard deviation of shadow fading difference

3.4.1 Modeling Tilt Dependent Shadowing

3.4.2 Introduction

Based on the detail analysis carried out in Section 3.43, a new tilt dependent dependent shadowing model is developed by employing statistical approach. The tilt-dependent shadowing model, henceforth, described by $\widehat{S^u_c}(\Theta^x_c)$ notation predicts the random shadowing variable at any new tilt setting $\Theta^x_c = \Theta^o_c + \Delta\Theta^x_c$ fulfilling the statistical correlation with respect to the shadowing at the reference tilt Θ^o_c, i.e. $\widehat{S^u_c}(\Theta^o_c)$. This requires to to know the desired $\rho^{\Theta^x_c,\Theta^o_c}_c$ level after $\Delta\Theta^x_c$ is introduced. Hence, a cross-correlation coefficient predictor function, to be used in the shadowing modeling, is derived empirically to approximate the statistical dependency of the shadowing only as a function of $\Delta\Theta^x_c$ and this is presented in Section 3.4.3. The shadowing model and tilt-dependent shadowing map generation procedure is discussed in Section 3.4.4

3.4.3   Modeling Shadowing Correlation

This section presents a function that provides a shadowing cross-correlation coefficient $\rho_c^{\Theta_c^x,\Theta_c^o}$ that represents the desirable statistical correlation level that has to be maintained when a new shadowing value is computed using the proposed tilt-dependent shadowing model.

The dependency of $\rho_c^{\Theta_c^x,\Theta_c^o}$ with $\Delta\Theta_c^x$ is derived based on extensive analysis of the extracted shadowing data. An empirical model for a correlation-coefficient predictor function described by $F_\rho(\Delta\Theta_c^x)$ is developed to account the tilt-dependent shadowing variation with a general expression. The model is used to incorporate an estimate of a statistical correlation drop of the shadowing values with an average $\rho_c^{\Theta_c^x,\Theta_c^o}$ that can be applied for all sites, i.e.,

$$\rho_c^{\Theta_c^x,\Theta_c^o} = F_\rho(\Delta\Theta_c^x). \tag{3.22}$$
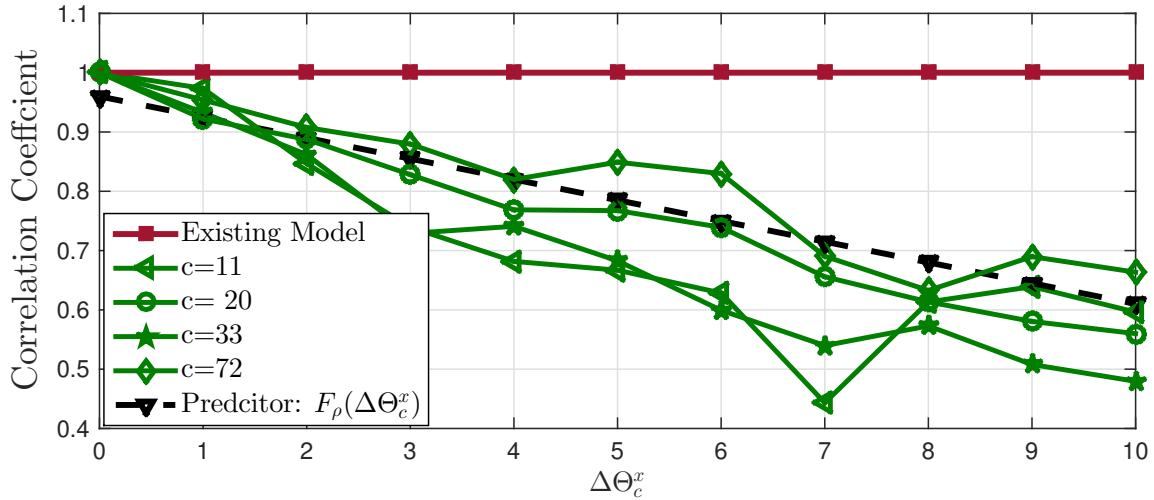
Figure 3.10. Shadowing statistics correlation for various $\Delta\Theta_c^x$

Figure (3.10) depicts selected plots of the shadowing-correlation as a function of $\Delta\Theta_c^x$. The figure clearly confirms existence of tilt-dependent variation of the correlation level of the shadowing fading where $\rho_c^{\Theta_c^x,\Theta_c^o}$ drops approximately linearly with $\Delta\Theta_c^x$. Hence, $F_\rho(\Delta\Theta_c^x)$ is modeled as a linear predictor function with coefficients φ and ξ , i.e.,

$$F_\rho(\Delta\Theta_c^x) = \varphi + \xi \cdot \Delta\Theta_c^x. \tag{3.23}$$

The predictor coefficients φ and ξ of the linear curve displayed in Figure (3.10) are determined empirically from the extracted tilt-specific shadowing maps for different $\Delta\Theta_x$ which corresponds to all sites of the considered network. The approach employs least-square fitting method that minimizes the sum square errors of $\tilde{\rho}_c^{\Theta_c^x,\Theta_c^o}$ from $F_\rho(\Delta\Theta_c^x)$ evaluated from all cells and for all range of tilt settings, i.e.,

$$\underset{\varphi,\,\xi}{\arg\min} \sum_{\substack{c \\ c\in\mathcal{C}}} \sum_{\substack{x \\ \Theta_c^x\in\vartheta_c}} \left(\rho_c^{\Theta_c^x,\Theta_c^o} - \left(\varphi + \xi\cdot\Delta\Theta_c^x \right) \right)^2. \tag{3.24}$$

Coefficient values $\varphi = 0.96$ and $\xi = -0.035$ are obtained which are specific to the considered RT-scenario, i.e., $F_\rho(\Delta\Theta_c^x) = 0.96 - 0.035\cdot\Delta\Theta_c^x$. The slop of $F_\rho(\Delta\Theta_c^x)$ indicates that the shadowing correlation drops by approximately 3.5% per 1° tilt change. In contrary, the existing 2D model assumes the shadowing fading effect as tilt independent thereby proposes full statistical correlation despite a change in the tilt, i.e. $\varphi = 1$ and $\xi = 0$.

Since the irregular site locations adopted in the considered RT-scenario are derived from real network planning data, the RT propagation maps utilized in the investigation are able to reflect various clutter experience of the real-world propagation effects. Therefore, the parameters introduced and derived in the proposed model, for example the coefficients of the correlation prediction function $F_\rho(\Delta\Theta_c^x)$, can be seen as valid and applicable to a wide range of case scenarios.

3.4.4   Tilt Specific Shadowing Generation

In this section the developed tilt dependent shadowing model and the procedure how to apply it to generate a new shadow map for a new tilt setting is discussed.

When the tilt is changed from Θ_c^o to Θ_c^x, the developed shadowing model estimates a new shadowing value $\widehat{S_c^u}(\Theta_c^x)$ that is normally distributed with zero mean and standard deviation σ_s. $\widehat{S_c^u}(\Theta_c^x)$ is generated from the shadowing fading value with respect to the same UE location at the reference tilt, $\widehat{S_c^u}(\Theta_c^o)$, while maintaining the desirable statistical dependency as defined in Equation (3.22). In order to determine $\widehat{S_c^u}(\Theta_c^x)$, the model introduces an independent normally distributed random variable described by $\Omega(\Delta\Theta_c^x)$. $\Omega(\Delta\Theta_c^x)$ and $\widehat{S_c^u}(\Theta_c^o)$ are combined in such away that the resulting random shadowing, $\widehat{S_c^u}(\Theta_c^x)$, remains statistically correlated with $\widehat{S_c^u}(\Theta_c^o)$ with correlation coefficient given by $F_\rho(\Delta\Theta_c^x)$, i.e.

$$\widehat{S_c^u}(\Theta_c^x) = F_\rho(\Delta\Theta_c^x)\cdot\widehat{S_c^u}(\Theta_c^o) + \sqrt{1 - F_\rho(\Delta\Theta_c^x)}\cdot\Omega(\Delta\Theta_c^x) \tag{3.25}$$

$$\text{required} \quad \frac{\mathrm{E}\left[\widehat{S^u_c}(\Theta^x_c) \cdot \widehat{\mathcal{S}^u_c}(\Theta^o_c)\right]}{\sigma_{\mathrm{s}} \cdot \underline{\sigma}_{\mathrm{s}}} = F_\rho(\Delta\Theta^x_c) \tag{3.26}$$

$$\mathrm{E}\left[\widehat{S^u_c}(\Theta^o_c) \cdot \Omega(\Delta\Theta^x_c)\right] = 0. \tag{3.27}$$

As explained in Equation (3.16) and demonstrated as well in Figure (3.6), the new shadow fading process is expected to have identical statistical distribution with that of $\widehat{\mathcal{S}^u_c}(\Theta^o_c)$ despite the tilt change. Thus, the variances can be approximated to be the same, i.e. $\sigma_{\mathrm{s}} \approx \underline{\sigma}_{\mathrm{s}}$, and the following conditions hold true,

$$\mathrm{Var}\left[\widehat{S^u_c}(\Theta^x_c)\right] = \mathrm{Var}\left[\widehat{S^u_c}(\Theta^o_c)\right], \tag{3.28}$$

$$\sigma^2_{\mathrm{s}} = \mathrm{Var}\left[F_\rho(\Delta\Theta^x_c) \cdot \widehat{\mathcal{S}^u_c}(\Theta^o_c) + \sqrt{1 - F_\rho(\Delta\Theta^x_c)} \cdot \Omega(\Delta\Theta^x_c)\right]. \tag{3.29}$$

From the relationship defined in Equation (3.28) and Equation (3.29), the variance for the independent random variable, σ^2_Ω, is derived as,

$$\sigma^2_\Omega = \underline{\sigma}^2_{\mathrm{s}} \cdot (1 + F_\rho(\Delta\Theta^x_c)), \quad \text{for} \quad F_\rho(\Delta\Theta^x_c) \neq 1. \tag{3.30}$$

As explained in Section 3.3, in addition to achieving statistically correlated shadowing value after tilt change, as stated by Equation (3.26), the condition with respect to the variance of the shadowing value difference statistics, $\sigma_{\Delta\mathrm{s}}(\Delta\Theta^x_c)$, which characterize the variability of the shadowing with tilt, as described by Equation (3.21), should be satisfied. This can be illustrated as follows,

$$\Delta\widehat{S^u_c}(\Theta^x_c, \Theta^o_c) = F_\rho(\Delta\Theta^x_c) \cdot \widehat{\mathcal{S}^u_c}(\Theta^o_c) + \sqrt{1 - F_\rho(\Delta\Theta^x_c)} \cdot \Omega(\Delta\Theta^x_c) - \widehat{\mathcal{S}^u_c}(\Theta^o_c) \tag{3.31}$$

$$= (F_\rho(\Delta\Theta^x_c) - 1) \cdot \widehat{S^u_c}(\Theta^o_c) + \sqrt{1 - F_\rho(\Delta\Theta^x_c)} \cdot \Omega(\Delta\Theta^x_c), \tag{3.32}$$

and the variance of $\Delta\widehat{S^u_c}(\Theta^x_c, \Theta^o_c)$ is described by,

$$\sigma^2_{\Delta\mathrm{s}}(\Delta\Theta^x_c) = 2 \cdot \underline{\sigma}^2_{\mathrm{s}} \cdot (1 - F_\rho(\Delta\Theta^x_c)). \tag{3.33}$$

Equation (3.33) confirms that, the shadowing variability indicated by $\sigma^2_{\Delta\mathrm{s}}(\Delta\Theta^x_c)$ increases when the shadowing values gets more de-correlated as the applied tilt change increases.

3.5 Performance of Tilt Dependent Shadowing Model

In this section, the statistical behaviors of the extracted shadowing fading values discussed in the modeling section are presented in detail and compared with the corresponding new values generated by applying the developed model. Furthermore, the

considered statistical distribution assumptions considered during the theoretical modeling section are validated.

Employing the new tilt-dependent shadowing model, defined by Equation (3.25), tilt-specific shadowing maps are reproduced from the existing shadowing map that corresponds to the reference tilt Θ_c^o. The statistical dependency between the shadowing values at Θ_c^x and Θ_c^o is guaranteed by Equation (3.26) where the correlation coefficient steers the prediction with respect to $\Delta\Theta_c^x$ whose approximation is demonstrated in Figure (3.10).
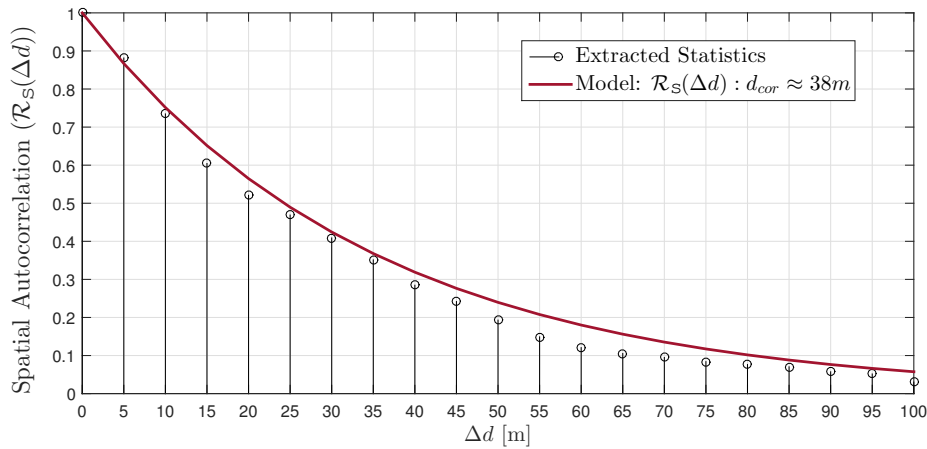
Figure 3.11. Model for spatial correlation of shadowing values

Another criterion which has to be satisfied is the inter-pixel spatial correlation characteristics of the shadowing values described by Equation (2.11). For this reason, the values of the independent random variable $\Omega(\Delta\Theta_c^x)$ introduced in the modeling, in Equation (3.25), are required to have the same spatial statistical correlation behavior as that of the reference shadow statistics extracted from the RT-based scenario as illustrated in Figure (3.11). The autocorrelation model which measures the spatial correlation of the shadowing defined by Equation (2.11) is still valid and applied for $\Omega(\Delta\Theta_c^x)$. Therefore, $\Omega(\Delta\Theta_x)$ values are generated for each user location point with spatial de-correlation distance of $d_{\text{cor}} \approx 38$ m apart whereas the values for other location points in between within inter-pixel distance of d_{cor} are assumed to be correlated and, hence, are computed via interpolation. Figure (3.12) demonstrates the autocorrelation model that is used to describe the spatial correlation of the shadowing values over inter-pixel distance. It is evident that both the model and the spatial correlation for the extracted shadowing values are declining exponentially over distance.

A final statistical analysis examines the distribution of the shadowing maps. Results, as portrayed in Figure (3.12), confirms that the shadowing maps generated with the

new model preserves almost identical statistical distribution where the mean, μ_s, and the standard deviation, σ_s, of the shadowing are in the same range irrespective of the applied tilt change. The plots in Figure (3.12)(a) represents the mean and standard deviation of the extracted shadowing values for a range of tilts for selected cells where $\Theta_c^o = 4°$. For comparison, the mean and standard deviation values of the corresponding shadowing map where the shadowing values at any Θ_c^x are generated from the values at Θ_c^o utilizing the new model, see in Figure (3.12)(b). In Figure (3.12), the non-variability of the standard deviation is clearly exhibited despite tilt changes.
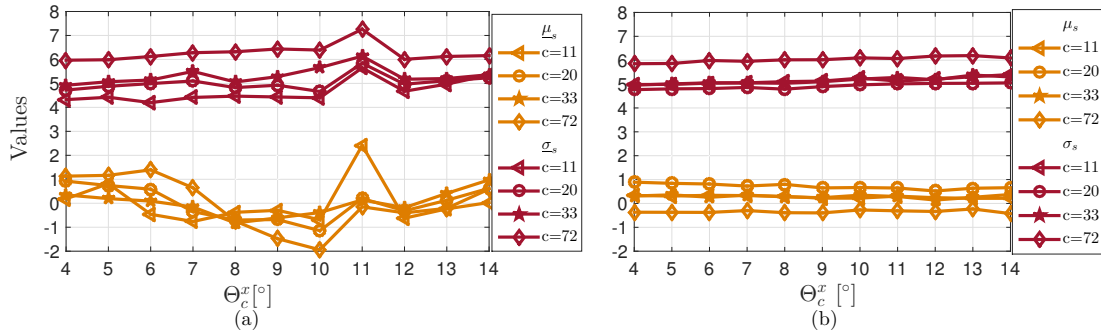
Figure 3.12. Shadowing mean and standard deviation (a) Extracted shadowing values (b) Shadowing values generated with the new model
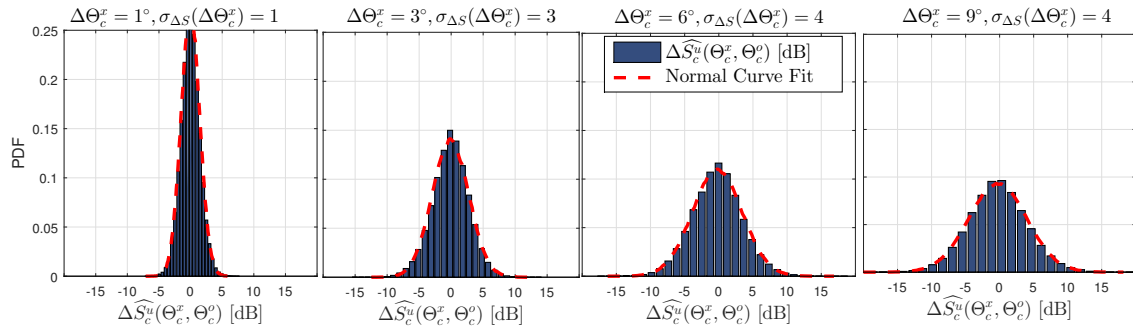
Figure 3.13. Distribution of $\Delta\widehat{\mathcal{S}_c^u}(\Theta_c^x, \Theta_c^o)$ generated using the new model

Additional validation criterion of the new model is concerning the statistical behavior of $\Delta\widehat{S_c^u}(\Theta_c^x, \Theta_c^o)$ defined by Equation (3.31). The statistical distribution presented in Figure (3.13) matches the expected behavior depicted in Figure (3.8) where $\sigma_{\Delta s}^2(\Delta\Theta_c^x)$ increases proportionally with the amount of the applied tilt change, $\Delta\Theta_c^x$. This is illustrated with an exemplary plots from selected site where $\Delta\widehat{S_c^u}(\Theta_c^x, \Theta_c^o)$ at different tilt setting is evaluated. The displayed statistical distribution curves in Figure (3.13) together with its standard deviation variation clearly manifests that the proposed model is able to characterize the impact of the tilt using the predicted shadowing value. Moreover, the observed statistical variability follows the same behavior as what has been exhibited in the extracted tilt-specific shadowing map illustrated in Figure (3.9).

The newly developed tilt dependent shadowing model is applied for the AAS-based sectorization in terms of SON-based control mechanisms in the following sections performance analysis.

Chapter 4

Vertical Sectorization

4.1 Introduction

Dense network configuration and hetrogenous network (HetNet) deployments consisting of small cells have been one of the paradigms of a radio network planning to cope with the increased traffic load problem and to provide higher capacity at a specific areas. Due to the fact that the real traffic distribution is varying intermittently over time and space, such kinds of fixed network densification is unused for a large part of the network operation time. Therefore, such deployment strategies are not very efficient and flexible.

AAS-equipped BS supports higher order sectorization where multiple beams are created simultaneously from a sector-antenna to split the conventional-cell coverage area into smaller coverages. By spatially reusing the total frequency spectrum at each new beam, the cell-splitting scheme with AAS-based sectorization multiplies the total amount of available radio resources. Through a controlled activation OF the beam(s) only when required, the AAS sectorization approach can effectively meet dynamic network capacity demand by intelligently tracking the spatial traffic concentrations and accordingly adapting the cell coverage layout. Unlike to the conventional approach where only horizontal sectorization is feasible, AAS-based sectorization can be applied either in the vertical and horizontal dimension depending on how the user traffic is spatially distributed within the underlying coverage area. This chapter presents the overall system model developed for the sectorization type in the vertical plane, i.e. vertical sectorization (VS). In VS the two beams which are separated in a vertical dimension with different elevation tilt are created splitting the conventional cell vertically in two: inner and outer cell. The model explains in detail the factors determining the performance of VS and provides the basis for the SON algorithm that control its optimal usage. The corresponding model for the sectorizatin in the horizontal plane is discussed separately in the next chapter, Chapter 6.

In this Chapter, the vertical sectorization model is presented in Section 4.2. The factors which determine the performance of VS are investigated in Section 4.3. In Section 4.4.1 the analysis for the inter-cell interference which arises due to the VS and the interference coordination model developed to combat the interference issue are

discussed. Section 4.5 presents a different VS scheme called Supercell as an alternative approach proposed for specific-use case scenarios. In the final section, Section 4.6.1, detailed performance evaluation and analysis are conducted.

4.2   Vertical Sectorization Model

4.2.1   Vertical Cell Layout and Parameter Settings

This section presents the layout of the new cells after VS and discusses the related system parameter settings.

Assume VS is applied at sector-antenna a and two vertical beams with index $b_a = 1$ and $b_a = 2$ are activated. The new cells also known as the vertical cells served by $b_a = 1$ and $b_a = 2$ are referred as outer and inner cells, respectively. Figure 4.1 illustrates VS with two vertical beams and corresponding underlying cell layout. The beams are spatially separated in the vertical dimension by steering them to different beam-specific elevation tilt angle of $\Theta_c, c \in \{c1, c2\} \subset \mathcal{C}$ and $A(c1) = A(c2) = a$, i.e. $\Theta_{c1} < \Theta_{c2}$. Maximizing utilization of the available spectrum, the total frequency is fully reused at the inner and outer cells thereby doubling the total radio resources available over the area of the conventional cell, i.e. maintaining M_{PRB} at each vertical cell. In order to mitigate the interference impact that arises from the co-channel operation, the overlap between the inner and outer vertical beam has to be minimized to a certain level and this can be carried out by controlling the offset angle $\Theta_{2,1}^a \neq 0$ between the tilt setting of each beam, i.e. $\Theta_{2,1}^a = \Theta_{c2} - \Theta_{c1}$, in addition to the size of the beam widths.
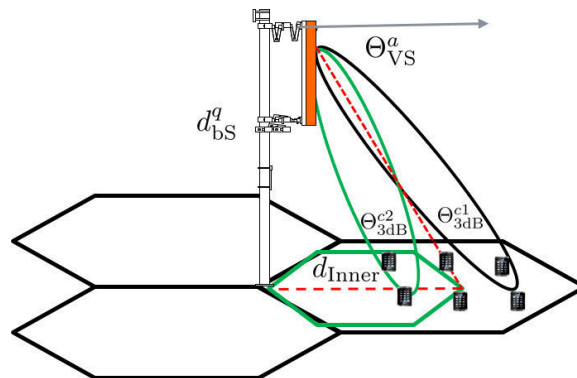

Figure 4.1. Vertical Sectorization

As described by Equation (2.20), when the secrtorization is carried out, the total power available per sector-antenna, P_a, is shared among the two cells where each cell is assigned with α_c power fraction,

$$P_{c1}^{\mathrm{tx}} + P_{c2}^{\mathrm{tx}} \leq P_a \tag{4.1}$$

$$\alpha_{a,1} + \alpha_{a,2} \leq 1. \tag{4.2}$$

Even though the vertical cells are co-sited and served by the same sector-antenna, as depicted in Figure (4.1), the overall attenuation, $h_c^u(\Phi_c, \Theta_c)$, experienced by a signal received by UE u from each cell is different. Incorporating Equation (4.1) into Equation (2.20) and utilizing the link budget calculation described by Equation (2.22), the link imbalance $\kappa_{2,1}^u$ between the channel with respect to the inner and the outer cell served by sector-antenna a is derived as the ratio of the received power level, i.e.,

$$\kappa_{2,1}^u = \frac{\alpha_{c2} \cdot h_{c2}^u(\Phi_{c2}, \Theta_{c2})}{\alpha_{c1} \cdot h_{c1}^u(\Phi_{c1}, \Theta_{c1})} = \frac{\alpha_{c2}}{\alpha_{c1}} \cdot 10^{0.1 \cdot (\widehat{G_{2,1}^u} + \widehat{S_{2,1}^u})}, \tag{4.3}$$

$$\text{where}: \quad \widehat{G_{2,1}^u} = \widehat{G_{c2}^u}(\Phi_{c2}, \Theta_{c2}^x) - \widehat{G_{c1}^u}(\Phi_{c1}, \Theta_{c1}^x), \tag{4.4}$$

$$\widehat{S_{2,1}^u} = \widehat{S_{c2}^u}(\Theta_{c2}) - \widehat{S_{c1}^u}(\Theta_{c1}), \quad \text{for} \quad A(s(u)) = a, \tag{4.5}$$

where $\widehat{G_{2,1}^u}$ is determined by the respective cell 3D beam pattern value in the direction of the UE u and $\widehat{S_{2,1}^u}$ characterizes the variation of the propagation shadowing effect due to the tilt difference $\Theta_{2,1}$, as discussed in Chapter 3. Considering a non-zero $\widehat{S_{2,1}^u}$ exists, the VS propagation model accounts the tilt dependent variation of the shadowing with respect to each cell with correlation coefficient $\rho^{\Theta_{c1}, \Theta_{c2}}$.

Since the AAS-based sectorization is intended to operate in a dynamic mode, the terms VS-activation (VS-ON) and VS-deactivation (VS-OFF) are used interchangeably to refer to the two specific states of VS executed on demand: vertical sectorization (VS) and conventional sectorization (CS), respectively. This will be indicated throughput the thesis by the sectorization status flag, l_a, defined in the system model Section 2.2.1.1,

$$l_a = \begin{cases} 0, & \text{VS-OFF} \\ 1, & \text{VS-ON}. \end{cases} \tag{4.6}$$

When VS is activated, UEs served by the conventional-cell being split are associated to one of the new cells which is dominant over the underlying coverage area as shown by Equation (2.23). The coverage dominance criterion which is the same as the link

imbalance described by Equation (4.3), $\kappa_{2,1}^u$, is determined by the relative strength of the RSRP measured by UE from the respective cell-specific RS,

$$\kappa_{2,1}^u = \frac{RSRP_{c2}^u}{RSRP_{c1}^u}. \tag{4.7}$$

The serving cell re-selection and association is, therefore, expressed as,

$$s(u) = \begin{cases} c1, & \text{if } \kappa_{2,1}^u \leq 10^{0.1 \cdot \chi_{hyst}} \\ c2, & \text{if } \kappa_{2,1}^u > 10^{0.1 \cdot \chi_{hyst}}. \end{cases} \tag{4.8}$$

where χ_{hyst} is a handover hysteresis margin in dB scale used to control the user hand-off operation between the inner and outer cell [HSS12].

Since cellular coverage layout planning is done carefully with drive test verification, it is not desirable to cause unintended coverage change and introduce additional interference on the neighborhood of an optimized network. For this reason, the SON algorithm which controls the VS activation/deactivation is designed to operate autonomously to change the cell layout only local to a particular site. As a consequence, the VS model is subjected to preserving the total coverage area served by the sector-antenna a, $\mathcal{A}_a$, before and after VS, i.e.,

$$\mathcal{A}_a \approx \begin{cases} \mathcal{A}_{co}, & \text{if } l_a = 0 \\ \mathcal{A}_{c1} \bigcup \mathcal{A}_{c2} & \text{if } l_a = 1, \end{cases} \tag{4.9}$$

where $c0 \in \mathcal{C}$ refers to the cell index for the conventional-cell and this can typically be maintained by fixing the RF parameters of the outer cell beam unaltered. The condition of Equation 4.9 can be satisfied by controlling the cell coverage dominance through the parameters of the beam serving each cell and the total transmit power P_{c1}^{tx} of the outer cell. The thesis author has related model analysis in [KWVK14a].

4.2.2   SINR Model for Vertical Sectorization

This section provides a model that expresses the achievable SINR performance of a user after VS in terms of the SINR value with respect to the same user achieved while being served by the conventional-cell. The relationship derived and presented with this model are essentially employed in Chapter 7 to estimate the user SINR performance prior to sectorization decision based on the actual RSRP measurements reported from the UE.

In fact the SINR performance of a user is changed when VS is activated as its serving cell and the interference distribution are altered. The general model for the user SINR

after sectorization described by Equation (2.59) can be directly adopted to the VS case. The total interference power received by UE u denoted by $\mathbb{I}'_u$ assuming the UE is connected to either of the vertical cells, i.e. $s(u) \in \{c1, c2\}$, can be expressed as the sum of the interference power coming from conventional-cells and any other split vertical-cells,

$$\mathbb{I}'_u = \underbrace{\sum_{\substack{\forall a \in \mathcal{Q} \\ l_a = 0}} \sum_{\substack{\forall c \in \mathcal{C} \\ A(c) = a}} \varsigma_c \cdot P^u_c}_{\text{Conventional cells}} + \underbrace{\sum_{\substack{\forall a \in \mathcal{Q} \\ l_a = 1}} \sum_{\substack{\forall c \in \mathcal{C}, c \neq s(u) \\ A(c) = a \wedge b_a = 1}} \varsigma_c \cdot P^u_c}_{\text{Outer cells}} + \underbrace{\sum_{\substack{\forall a \in \mathcal{Q} \\ l_a = 1}} \sum_{\substack{\forall c \in \mathcal{C} \\ A(c) = a \wedge b_a = 2}} \varsigma_c \cdot P^u_c}_{\text{Inner cells}}. \quad (4.10)$$

Due to the required steeper tilt setting for inner cell beam, $\Theta_{c2} > \Theta_{c1}$, the interference contribution from the inner cells of neighbor-sites where VS is activated has insignificant impact. This is indicated in [KWVK14a] and also will be demonstrated in the upcoming section. Hence, the interference signal power term from any VS activated site in Equation (4.10) can be approximated using only the signal power received from the outer cell.

Furthermore, it is essential that the VS model addresses practical challenges by minimizing unintended cell layout changes and the impact of the additional interference level in the network. In order to limit the undue interference injected into neighbor cells by the outer cell of the VS and to satisfy the coverage constraint specified by Equation (4.9), the elevation tilt of the outer cell is fixed to the same setting to that of its corresponding the conventional cell, the cell before VS. Practically, this can be managed by a sectorization strategy where only an inner beam corresponding to the inner cell is activated when VS is intended and the actual beam that has been serving the conventional-cell will be assigned to the outer cell as discussed by the thesis author in [KWVK14a]. Consequently, the signal power received by UE u from the conventional-cell and the outer cell, before and after VS activation, respectively, can be related as

$$P^u_{c1} = \frac{\alpha_{a,1}}{\alpha_{a,0}} \cdot P^u_{c0}, \quad \text{for} \ \ \Theta_{c1} = \Theta_{c0} \wedge A(c1) = A(c0) = a. \quad (4.11)$$

The detail analysis for the trade-off between the beam parameter settings and VS performance will be presented in the subsequent section.

Omitting the impact of the inter-cell interference coming from the inner-cell of neighbor sites, due to the aforementioned reason, and embodying Equation (4.11) in Equation (4.10), the SINR γ'_u of UE u connected to either of the vertical cells is expressed

including the interference power from all co-sited cells as

$$
\gamma'_u = \begin{cases} \dfrac{P^u_{s(u)}}{\displaystyle\sum_{\substack{\forall a \in \mathcal{Q} \\ b_a=0 \\ Q(c)\neq Q(s(u))}} \sum_{\substack{\forall c \in \mathcal{C} \\ A(c)=a}} \varsigma_c \cdot P^u_c \cdot [1 - l_a \cdot (1 - \frac{\alpha_{a,1}}{\alpha_{a,0}})] \ + \displaystyle\sum_{\substack{\forall a \in \mathcal{Q} \\ b_a=2 \\ }} \sum_{\substack{\forall c \in \mathcal{C} \\ c\neq s(u) \\ A(c)=a \\ Q(c)=Q(s(u))}} l_a \cdot \varsigma_c \cdot P^u_c + P_{\mathrm{N}}}, & s(u)=c1 \\[40pt] \dfrac{P^u_{s(u)}}{\displaystyle\sum_{\substack{\forall a \in \mathcal{Q} \\ b_a=0 \\ Q(c)\neq Q(s(u))}} \sum_{\substack{\forall c \in \mathcal{C} \\ A(c)=a}} \varsigma_c \cdot P^u_c \cdot [1 - l_a \cdot (1 - \frac{\alpha_{a,1}}{\alpha_{a,0}})] \ + \varsigma_{c1} \cdot P^u_{c1} + \displaystyle\sum_{\substack{\forall a \in \mathcal{Q} \\ b_a=2}} \sum_{\substack{\forall c \in \mathcal{C}, \\ c\neq s(u) \\ A(c)=a \\ Q(c)=Q(s(u))}} l_a \cdot \varsigma_c \cdot P^u_c + P_{\mathrm{N}}}, & s(u)=c2. \end{cases}
$$

$$(4.12)$$

With additional manipulation of Equation (4.12) and incorporating the assumptions considered in the earlier discussion, SINR model for VS expressing γ'_u as a function of the SINR performance before VS, γ_u, is derived. Given ψ^u represents the sum of all interference power received by UE u from co-sited inner and outer cells normalized to the serving power of the UE, i.e.

$$
\psi^u = \frac{1}{P^u_{s(u)}} \cdot \sum_{\substack{\forall a \in \mathcal{Q} \\ b_a=2}} \sum_{\substack{\forall c \in \mathcal{C}, \\ c\neq s(u) \\ A(c)=a \\ Q(c)=Q(s(u))}} l_a \cdot \varsigma_c \cdot P^u_c.
$$

$$(4.13)$$

Therefore, γ'_u is described as

$$
\gamma'_u = \begin{cases} \dfrac{\alpha_{a,1} \cdot \gamma_u}{\alpha_{a,0} + \alpha_{a,1} \cdot \gamma_u \cdot [\kappa^u_{2,1} \cdot \varsigma_{c2} \ + \ \psi^u]}, & \text{if } \{\forall u | s(u)=c1\} \\[30pt] \dfrac{\alpha_{a,1} \cdot \kappa^u_{2,1} \cdot \gamma_u}{\alpha_{a,0} + \alpha_{a,1} \cdot \gamma_u \cdot [\varsigma_{c1} \ + \ \kappa^u_{2,1} \cdot \psi^u]} & \text{if } \{\forall u | s(u)=c2\} \end{cases}
$$

$$(4.14)$$

4.3 Factors Determining Vertical Sectorization Performance

4.3.1 Introduction

Compared to the conventional-cell case, the enhancement in the achievable user throughput with VS is determined by the amount of radio resource gained and the change in the SINR performance. In order to decide whether the VS is beneficial for a particular UE or not, the UE throughput gain designated by η_u is compared to the

throughput performance achieved before VS, τ_u. Given the resource share of a UE after VS by R'_u, η_u is described as

$$\eta_u = \frac{\tau'_u - \tau_u}{\tau_u} = \frac{R'_u \cdot \mathcal{F}(\gamma'_u)}{R_u \cdot \mathcal{F}(\gamma_u)} - 1. \tag{4.15}$$

R'_u is assigned according the employed PF-based resource-fair sharing strategy as described by Equation (2.64), i.e,

$$R'_u = \begin{cases} \frac{1}{N^{\mathrm{u}}_{c1}}, & \text{if } \{\forall u | s(u) = c1\}, \\ \frac{1}{N^{\mathrm{u}}_{c2}}, & \text{if } \{\forall u | s(u) = c2\}, \end{cases} \tag{4.16}$$

where $N^{\mathrm{u}}_{c1} = |\mathcal{A}_{c1}|$ and $N^{\mathrm{u}}_{c2} = |\mathcal{A}_{c2}|$.

Irrespective to which vertical cell the UE is connected, the expectable improvement in the resource share $\frac{R'_u}{R_u}$ with VS depends on the relative redistribution of the user load between the inner and the outer cells, i.e. N^{u}_{c1} and N^{u}_{c2}. In the event of the VS activation, the number of the UEs that goes to either of the cells is heavily influenced by the nature of the spatial distribution of the UEs and the size of the coverage dominance area of the cells which in turn is determined by the link imbalanced $\kappa^u_{2,1}$ measured at the UE.

In this Section, the factors determining the performance of VS are presented. The section investigates the impact of various system parameters settings and provides detail analysis for the trade-off between the settings and the VS performance. Section 4.3.2 discusses the effect of the spatial user distribution and Section 4.3.3 analyzes the effect of the beam parameter settings. The inter-cell interference between the vertical cells is investigated in Section 4.4.1

4.3.2   Spatial User Distribution

This section explains the effect of the spatial distribution of users on the performance of VS.

A load redistribution metric denoted by λ_a specifies the fraction of user load taken by the inner cell with respect to the load remaining in the outer cell where both cells are served by sector-antenna a. In this thesis, λ_a is defined as the ratio of the number of connected UEs at each cell,

$$\lambda_a = \frac{N^{\mathrm{u}}_{c2}}{N^{\mathrm{u}}_{c1}} \tag{4.17}$$

From Equation 4.16 and Equation (4.17), the achievable R'_u is expressed using the load redistribution measure parameter λ_a to derive a vital inter-relationship between the resource share of a user before and after VS, i.e.,

$$R'_u = R_u \cdot \begin{cases} 1 + \lambda_a, & \text{if,} \quad \{\forall u | s(u) = c1\} \\[2ex] \frac{1+\lambda_a}{\lambda_a}, & \{\text{if,} \quad \forall u | s(u) = c2\}. \end{cases} \tag{4.18}$$

Equation (4.18) is illustrated in Figure (4.2) where the dependency of the resource share gain is explained as a function of λ_a. Accordingly, the gain from resource increases proportionally with λ_a for UEs at the outer cell. On the contrary, the resource gain diminishes at the inner cell for larger λ_a as the resource competition gets higher. The resource gain over both cells is fairly maximized when the load distribution between the cells is balanced and this is achieved when $\lambda_a = 1$.
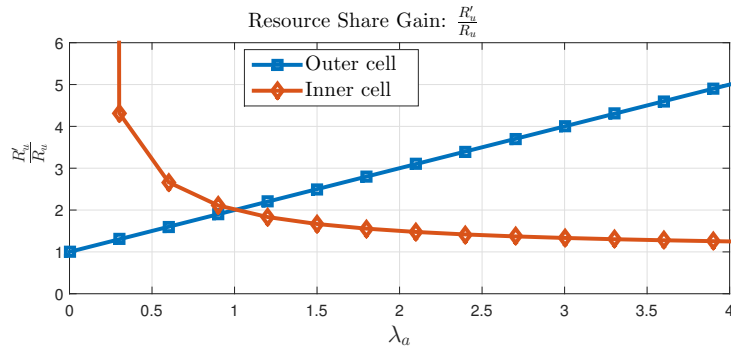
Figure 4.2. Resource share gain with VS

4.3.3   Beam Parameter Settings

This section provides the analysis for the effect of different parameter settings of the beams serving the vertical cells.

As described in Equations (4.3), (4.7) and (4.8), the elevation tilt Θ_c and the elevation HPBW $\Theta^c_{3\text{dB}}$ settings of each cell are important radio parameters in determining the dominance area of the vertical cells through controlling the $\widehat{G^u_{2,1}}$ value in $\kappa^u_{2,1}$. Since the azimuth domain beam characteristics are identical, as explained in Chapter 2 VS beam pattern model, $\widehat{G^u_{2,1}}$ particularly depends on the pattern of each beam in the elevation domain. Due to the fact that the maximum antenna gain achieved in the boresight direction is essentially controlled by the beam width [MHK16], the inverse

proportional inter-relationship between $G_c^{\max}$ and $\Theta_{3\mathrm{dB}}^c$ is defined to explain the effect of the difference in the HPBW setting of each vertical beam as,

$$\frac{G_{c2}^{\max}}{G_{c1}^{\max}} = \frac{\Theta_{3\mathrm{dB}}^{c1}}{\Theta_{3\mathrm{dB}}^{c2}} \tag{4.19}$$

Taking Equation (4.19) into account and the 3D beampattern model given by Equation (2.18), the impact of the beam parameters is demonstrated by deriving an analytical expression for $\widehat{G_{2,1}^u}$,

$$\widehat{G_{2,1}^u} = -10 \cdot \log_{10}(\Xi) + 12 \cdot \left(\frac{\Xi^2 \cdot (\theta - \Theta_{c1})^2 - (\theta - \Theta_{c1} - \Theta_{2,1}^a)^2}{(\Xi \cdot \Theta_{3\mathrm{dB}}^{c1})^2}\right) \tag{4.20}$$

where $\Xi = \frac{\Theta_{3\mathrm{dB}}^{c2}}{\Theta_{3\mathrm{dB}}^{c1}}$ is the relative HPBW of the inner cell beam with respect to the outer, i.e. when $\Xi = 1$ both beams have equal elevation HPBW. For the same total transmitted power per beam, i.e. $\alpha_{a,1} = \alpha_{a,2}$, the theoretical inner/outer cell border where $\kappa_{2,1}^u = 1$, according to Equation (4.3) and (4.7), is defined at an elevation angle Θ_{VS}^a where the antenna gain from each beam is equal. This is depicted in Figure (4.1).

$$\Theta_{\mathrm{VS}}^a = \theta|_{\widehat{G_{2,1}^u} = 0} = \begin{cases} \Theta_{c1} + \frac{1}{2} \cdot \Theta_{2,1}^a, & \Xi = 1 \\ \\ \Theta_{c1} + \frac{\Xi}{(\Xi^2 - 1)} \cdot \sqrt{(\Theta_{2,1}^a)^2 - 0.833 \cdot \Theta_{3\mathrm{dB}}^{c1} \cdot (\Xi^2 - 1) \cdot \log_{10}(\Xi)}, & \Xi \neq 1. \end{cases} \tag{4.21}$$

Therefore, using Equation (4.21), an expression for the inner cell coverage size can be defined geometrically, as indicated in Figure (4.1), by looking at the distance of the inner/outer border, d_{Inner}, from the BS in the boresight direction. Varying d_{Inner} by adjusting the beam parameters configuration controls the trade-offs on the size of the inner cell coverage determining the load distribution which in turn impacts the achievable resource gain. As demonstrated in Figure (4.3), the inner cell coverage gets smaller for a higher tilt offset Θ_{VS}^a. As indicated in Figure (4.3)(b), aggressive downtilting of the inner beam shrinks its dominance area. Taking d_{BS}^q is the mast height at site q where the BS antenna is mounted, the inner/outer cell border d_{Inner} is computed using the following expression based on the Θ_{VS}^a value

$$d_{\mathrm{Inner}} = d_{\mathrm{bS}}^q \cdot \tan(90 - \Theta_{\mathrm{VS}}^a). \tag{4.22}$$

Moreover, it has been indicated that unequal setting of $\Theta_{3\mathrm{dB}}^c$ where $\Xi \neq 1$ remarkably alters the inner cell coverage size by reducing the level of the beam overlapping in the elevation domain. Despite the fact that $\Xi > 1$ broadens the inner beam, it does not provide a better inner cell coverage dominance as the resulting $G_c^{\max}$ value is deteriorated with wider $\Theta_{3\mathrm{dB}}^{c2}$ for the reason explained by Equation (4.19). It is demonstrated that the lower Ξ yields a larger inner cell coverage particularly when small tilt offset

value is applied between the vertical beams. On the other hand, high Ξ and low $\Theta_{2,1}^a$ settings causes an undesirably increased beam overlaps, hence, it is required to properly adjust $\Theta_{2,1}^a$ setting in order to deliver maximized system performance.
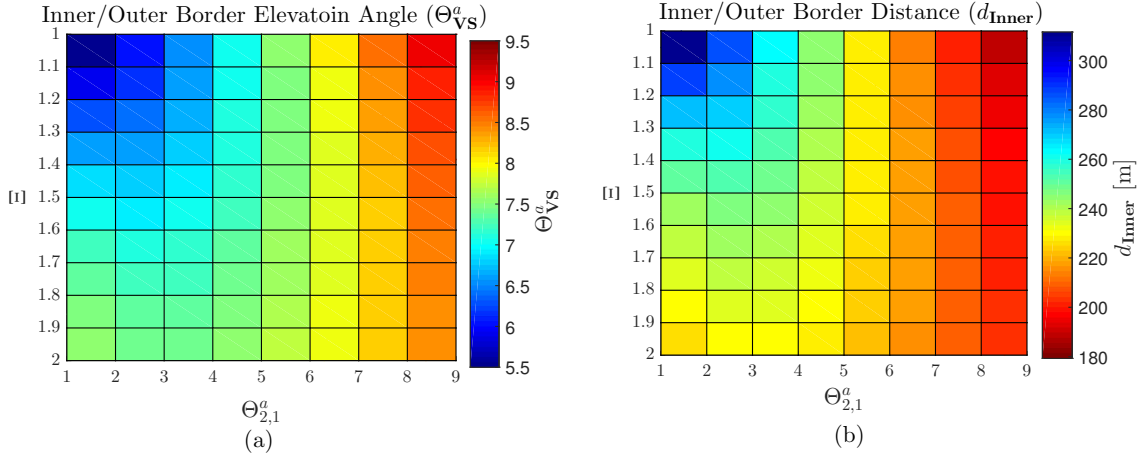
Figure 4.3. Impact of Beam parameter settings on cell coverage dominance

4.3.4   Inter-Cell Interference Between Vertical Cells

This section investigates the impact of the ensuing inter-cell interference from the co-channel operation of the vertical cells.

The system performance gain attributed to the gain from radio resource, i.e. $\frac{R'_u}{R_u} > 1$, can countermanded by the impact of the resulting inter-cell co-channel interference, as indicated in Equation (4.15). The extent to which the interference impact is significant for a particular UE depends on the the relative location where the UE is spatially located with respect to the inner/outer border region where interference is severe. Consequently, the level of the SINR degradation is a crucial factor in determining the overall VS performance. Using the SINR model described by Equation (4.14), the SINR deterioration with VS can be explained by introducing an expression for the SINR ratio $\frac{\gamma'_u}{\gamma_u}$. Thus, the SINR change experienced by UE u in dB scale $\Delta\widehat{\gamma_u} = 10 \cdot \log_{10} \frac{\gamma'_u}{\gamma_u}$ is described as,

$$
\Delta\widehat{\gamma_u} = \begin{cases} -10 \cdot \log_{10}(\frac{\alpha_{a,0}}{\alpha_{a,1}} + \gamma_u \cdot [\kappa_{2,1}^u \cdot \varsigma_{c2} \quad + \quad \psi^u]), & \text{if } \{\forall u | s(u) = c1\}, \\[2em] 10 \cdot \Big(\log_{10}(\kappa_{2,1}^u) - \log_{10}(\frac{\alpha_{a,0}}{\alpha_{a,1}} + \gamma_u \cdot [\varsigma_{c1} \quad + \quad \kappa_{2,1}^u \cdot \psi^u]) \Big), & \text{if } \{\forall u | s(u) = c2\}. \end{cases}
$$
(4.23)
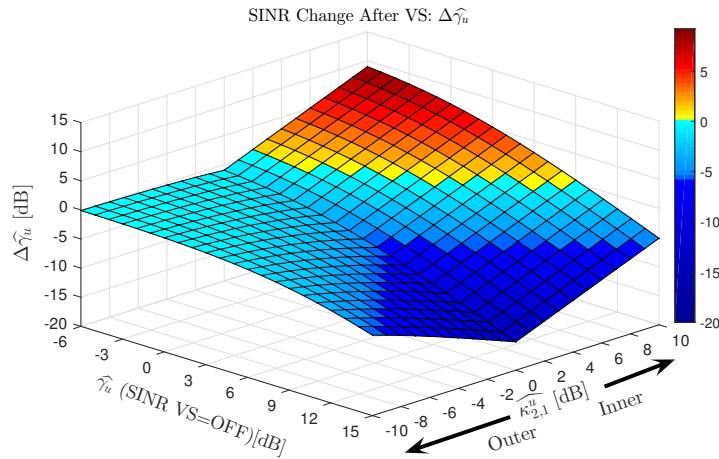
Figure 4.4. SINR Change After VS

Figure (4.4) illustrates the variation of $\Delta\widehat{\gamma_u}$ with γ_u and the spatial location of the UE that is characterized by $\widehat{\kappa_{2,1}^u}$. As can be deduced from Equation (4.23) and clearly be seen in Figure (4.4), the relative SINR deterioration is severe for UEs having high SINR value, γ_u, before the VS. Those UEs are mainly located to the center of the conventional cell coverage and could potentially experience an extreme inter-cell interference after VS activation as the inner/outer coverage border appearing in the area is characterized by $|\widehat{\kappa_{2,1}^u}| \to 0$ where $\widehat{\kappa_{2,1}^u} = 10 \cdot \log_{10}\left(\kappa_{2,1}^u\right)$. On the other hand, the lower SINR region UEs connected to the outer cell are less impacted and are always insensitive $\Delta\widehat{\gamma_u} \to 0$ for the VS activation because $\widehat{\kappa_{2,1}^u} < 0$ as the UEs are faraway from the inner/outer border region. Moreover, at high $\widehat{\kappa_{2,1}^u}$ values, i.e. inner cell is dominant for the UE residing in the area, the SINR performance is improved because the high received power resulting from steep downtilt setting yields $\Delta\widehat{\gamma_u} > 0$. This is demonstrated in Figure (4.4).

4.4 Inter-Cell Interference Coordination Between Vertical Cells

4.4.1 Introduction

The capacity gain in VS attributed to the enhancement in the amount of resource share is often countermanded by the intra-site inter-cell interference resulting between the co-channel operated vertical cells. To combat this interference problem, an interference

coordination mechanism is developed by adopting the enhanced Inter Cell Interference Coordination (eICIC) scheme which is widely used in LTE HetNet for macro/small cell deployment scenario [WSP12, 3GP15a]. The newly developed technique called in this thesis VS-eICIC exploits underutilized radio resources at the inner cell to alleviate the interference level received by the severely impacted outer cell UEs via applying a transmission muting principle on selected radio subframes [WSP12, DMW+11]. As explained in Section , the SINR degradation is more severe for outer cell UEs closer to the inner/outer border. Consequently, the inner cell is regarded as an aggressive interferer where the VS-eICIC applies the transmission blanking.

Detailed analysis for the impact of the inter-cell interference is provided in Section 4.4.2. The VS-eICIC scheme developed for the interference coordination is presented in Section 4.4.3.1 and, in Section 4.4.4, an optimization framework that is used to adapt the transmission blanking pattern is explained.

4.4.2   Inter-Cell Interference Impact Analysis

This section provides the analysis for the interference level between the vertical cells.

The inter-cell interference is a big challenge with VS due to the aggressive frequency reuse between the vertical cells. As described by Equation (4.23), the severity of the level of the inter-cell interference varies at different regions over the coverage layout. Therefore, the interference problem can be exacerbated by the spatial distribution of the UEs. This is manifested in Figure (4.4)(a) with a color map of the SINR deterioration experienced while VS is activated at all cos-sited sector-antenna. It is expected and also demonstrated that UEs located close to the new inner/outer cell border region are critically impacted by the interference and experience a significant SINR loss, see $\Delta\widehat{\gamma_u}$ in Figure (4.4) (a). For this reason, those UEs which have been highly impacted by the interference are classified as sensitive group of UEs (S-UE) and they are to be treated as the severely interference affected UEs after VS activation. The notation $g_u = $ S is used to refer to a UE that belongs to S-UEs group. Whereas, the UEs which experience less SINR loss are classified as non-sensitive (NS-UE) and are denoted by $g_u = $ NS. Within the conventional-cell layout, the coverage region where S-UEs and NS-UEs are spatially located is illustrated in Figure (4.5) (a) wherein the figure clearly demonstrates the variation of $\Delta\widehat{\gamma_u}$ for a VS activated site and the corresponding sensitivity regions that are referred as sensitive and non-sensitive.
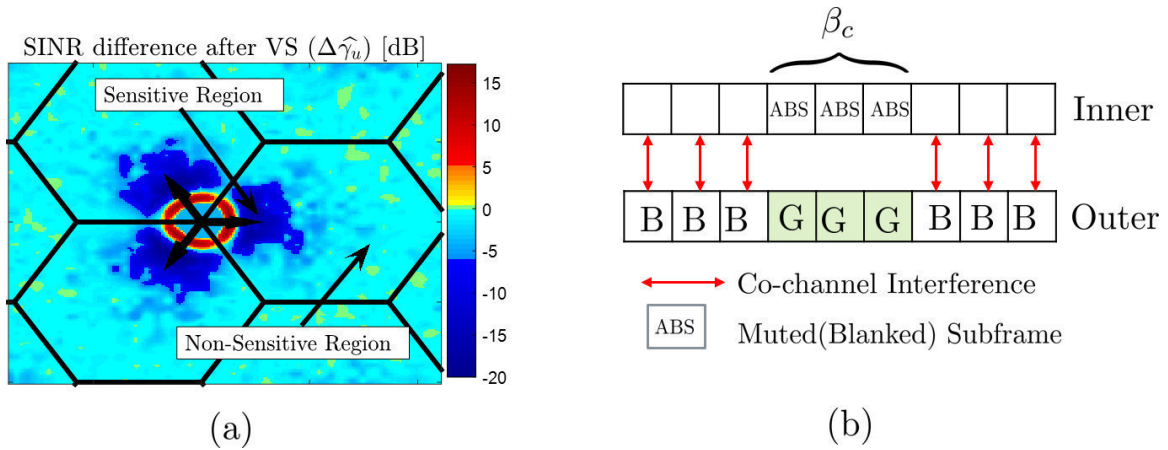
Figure 4.5. (a) SINR Change After VS, (b) FDD-LTE Downlink Radio Frame Structure with Transmission Blanking

4.4.3 Enhanced Inter-Cell Interference Coordination (eICIC) Mechanism for Vertical Sectorization

This section describes the principles of the interference coordination scheme to be used with VS.

The eICIC scheme, being used in controlling the interference level in HetNet environments relies on muting the data transmission over selected radio subframes [WSP12] [DMW$^+$11, TZV$^+$14]. In this section, VS-eICIC method is developed adopting the identical principle where the radio transmissions during β_c fraction of the inner cell's radio subframes are muted to protect the corresponding outer-cell subframes so that sensitive region UEs can be scheduled in a better SINR condition [WSP12, DMW$^+$11]. During the muted subframes, data signal is not transmitted at the inner cell but only critical system information and Common Reference Signals (CRS). For this reason the muted subframes are also called Almost Blank Subframes (ABS) and the muting scheme is referred as transmission blanking [3GP15a]. Figure (4.5) (b) depicts the muted subframes and the time domain transmission coordination using an FDD-LTE downlink radio frame structure. Such transmission coordination principle yields two types of radio subframes at the outer cell which are classified based on the interference experience from the corresponding inner-cell: i) Good-SINR (G) subframes, and ii) Bad-SINR (B) subframes. In order to identify the UEs to be scheduled over G- or B-subframes, SINR sesitivity measure is considered. A user sensitivity measure metric Γ_u^a is defined that characterizes the sensitivity of the UE for the inter-vertical cell interference. Given $\gamma_u'^{\mathrm{G}}$ and $\gamma_u'^{\mathrm{B}}$ are the average SINR values of a UE per PRB on G- and B-subframes, respectively, Γ_u^a is defined as the ratio of the spectral efficiency performance of the UE

when scheduled on a G-subframe and B-subframe, i.e.,

$$\Gamma_u^a = \frac{\mathcal{F}(\gamma_u'^{\mathrm{G}})}{\mathcal{F}(\gamma_u'^{\mathrm{B}})} \geq 1, \tag{4.24}$$

Depending on the sensitivity level distribution at the outer cell, a sensitivity level threshold Γ^{Thr} is applied by the scheduler to categorize the UEs in two groups as discussed: S-UEs and NS-UEs [KFW$^+$15], where

$$N_{c1}^{\mathrm{u(S)}} = \sum_{\forall u \in \mathcal{A}_{c1}} \mathbf{1}\{\Gamma_u^a \geq \Gamma^{\mathrm{Thr}}\}, \tag{4.25}$$

$$N_{c1}^{\mathrm{u(NS)}} = \sum_{\forall u \in \mathcal{A}_{c1}} \mathbf{1}\{1 \leq \Gamma_u^a < \Gamma^{\mathrm{Thr}}\}. \tag{4.26}$$

4.4.3.1   Transmission Blanking Pattern of Radio Subframe

The amount of mutable resources at the inner cell, also known as the blanking pattern, is configured based on the load at the inner cell itself as well as the sensitivity distribution at the outer cell. To create an abstraction for the VS-eICIC aware resource partitioning, the total amount of radio resources available at the scheduling time with respect to each vertical cells are analyzed. Apparently, a blanking pattern configuration of β_{c2} at the inner cell reduces the total resources effectively available at the inner cell to $M_{\mathrm{PRB}} \cdot (1 - \beta_{c2})$. On the other hand, the transmission blanking yields $M_{\mathrm{PRB}}^{\mathrm{g}} = M_{\mathrm{PRB}} \cdot \beta_c$ and $M_{\mathrm{PRB}}^{\mathrm{b}} = M_{\mathrm{PRB}} \cdot (1 - \beta_{c2})$ amount of resources from G- and B-subframes, respectively, at the outer cell, i.e. $M_{\mathrm{PRB}} = M_{\mathrm{PRB}}^{\mathrm{g}} + M_{\mathrm{PRB}}^{\mathrm{b}}$. The VS-eICIC scheme employs a resource allocation strategy where the radio resources from the G- and B-subframes are partitioned with a resource share amount that maximizes the overall system performance over the aggregate coverage area, $\mathcal{A}_a$. The detail resource allocaiton and paritioniing strategy is presented in Section 4.4.3.2.

4.4.3.2   Radio Resource Partitioning Strategy with Fixed Blanking Pattern

This section presents the resource allocation strategy applied to coordinate the interference employed by VS-eICIC.

The PF resource allocation strategy aiming at maximizing the sum throughput utility $U_c = \sum_u \log(\tau_u')$ of cell c as described in Equation (2.64) is employed to fairly distribute the radio resources among the UEs at the vertical cells. Similar to what is derived for

the conventional sectorization case in Equation (2.64), the radio resource allocation objective defined with respect to the inner cell is subjected to a constraint only that puts a limit on the upper bound of the sum of all assigned resource shares [KFW+15]. The resource allocation set at the inner cell, $\mathcal{R}'_{c2} = \{R'_u | u \in \mathcal{A}_{c2}\}$, is given by

$$\underset{R'_u}{\operatorname{argmax}} \sum_{u \in \mathcal{A}_{c2}} \log(R'_u \cdot \mathcal{F}(\gamma'_u)), \tag{4.27}$$

$$\text{subject to : } \sum_{u \in \mathcal{A}_{c2}} R'_u = 1 - \beta_c, \qquad R'_u \geq 0, \tag{4.28}$$

then,

$$R'_u = \frac{1 - \beta_c}{N^u_{c2}} \quad \{\forall u | s(u) = c2\}. \tag{4.29}$$

Maximizing the sum $\sum \log(\tau'_u) = \sum \log(R'_u \cdot \mathcal{F}(\gamma'_u)) + \sum \log(M_{\text{PRB}} \cdot \Omega_{\text{PRB}})$ is the same as shown in Equation (4.27) if the second constant term is dropped out. Henceforth, the utility expression as indicated by Equation (4.27) will be used likewise.

At the outer cell, however, having two group of UEs and two types of resources make the resource partitioning strategy more complex as the total resource share of an outer cell UE R'_u for $g_u \in \{\text{S}, \text{NS}\}$ is composed of a resource shares of R'^{G}_{u,g_u} and R'^{B}_{u,g_u} from G-subframes and B-subframes, respectively, i.e.,

$$R'_u = R'^{\text{G}}_{u,g_u} + R'^{\text{B}}_{u,g_u}, \quad g_u \in \{\text{S}, \text{NS}\} \quad \{\forall u | s(u) = c1\}. \tag{4.30}$$

Accordingly, the sum throughput utility of the outer cell U_{c1} is described as,

$$U_{c1} = \sum_{\substack{u \in \mathcal{A}_{c1} \\ g_u = \text{S}}} \log(R'^{\text{G}}_{u,g_u} \cdot \mathcal{F}(\gamma'^{\text{G}}_u) + R'^{\text{B}}_{u,g_u} \cdot \mathcal{F}(\gamma'^{\text{B}}_u)) + \sum_{\substack{u \in \mathcal{A}_{c1} \\ g_u = \text{NS}}} \log(R'^{\text{G}}_{u,g_u} \cdot \mathcal{F}(\gamma'^{\text{G}}_u) + R'^{\text{B}}_{u,g_u} \cdot \mathcal{F}(\gamma'^{\text{B}}_u)).$$
$$\tag{4.31}$$

Having the expression for the composite resource shares R'_u, the resource allocation problem at the outer cell is provided subjected to multiple constraints as shown below,

$$\underset{R'^{\text{G}}_{u,\text{S}}, R'^{\text{B}}_{u,\text{S}}, R'^{\text{G}}_{u,\text{NS}}, R'^{\text{B}}_{u,\text{NS}}}{\operatorname{argmax}} \mathbb{U}_{c1},$$

$$\text{subject to: } \sum_{\substack{u \in \mathcal{A}_{c1} \\ g_u = \text{S}}} R'^{\text{G}}_{u,g_u} + \sum_{\substack{u \in \mathcal{A}_{c1} \\ g_u = \text{NS}}} R'^{\text{G}}_{u,g_u} = \beta_{c2},$$

$$\sum_{\substack{u \in \mathcal{A}_{c1} \\ g_u = \text{S}}} R'^{\text{B}}_{u,g_u} + \sum_{\substack{u \in \mathcal{A}_{c1} \\ g_u = \text{NS}}} R'^{\text{B}}_{u,g_u} = 1 - \beta_{c2}, \tag{4.32}$$

$$\sum_{\substack{u \in \mathcal{A}_{c1} \\ g_u = \text{S}}} R'_{u,g_u} + \sum_{\substack{u \in \mathcal{A}_{c1} \\ g_u = \text{NS}}} R'_{u,g_u} = 1,$$

$$R'^{\text{G}}_{u,\text{S}}, R'^{\text{G}}_{u,\text{NS}}, R'^{\text{B}}_{u,\text{S}}, R'^{\text{B}}_{u,\text{NS}} \geq 0.$$

The resource allocation strategy at the conventional and inner cell have manifested that the sum of the logarithm of the throughput is maximized within the same group of UEs when fairness is achieved with respect to resource. Unless a different type UEs or resources exist, the resource fairness is maintained when the UEs are assigned with equal share [KFW$^+$15, TZV$^+$14]. Considering the S-UEs and NS-UEs are characterized by an average SINR performance, user group-based resource partitioning can be utilized in order to further simplify the resource allocation problem at the outer cell described with Equation (4.32) by defining group resource shares that satisfies the following relationship,

$$\mu_S^G = \sum_{\substack{\forall u \in \mathcal{A}_{c1} \\ g_u = S}} R_{u,g_u}^{\prime G}, \quad \mu_{NS}^G = \sum_{\substack{\forall u \in \mathcal{A}_{c1} \\ g_u = NS}} R_{u,g_u}^{\prime G}, \quad \mu_S^B = \sum_{\substack{\forall u \in \mathcal{A}_{c1} \\ g_u = S}} R_{u,g_u}^{\prime B}, \quad \mu_{NS}^B = \sum_{\substack{\forall u \in \mathcal{A}_{c1} \\ g_u = NS}} R_{u,g_u}^{\prime B},$$

$$\text{then,} \qquad R_{u,g_u}^{\prime G} = \frac{\mu_{g_u}^G}{N_{c1}^{u(g_u)}}, \qquad\qquad R_{u,g_u}^{\prime B} = \frac{\mu_{g_u}^B}{N_{c1}^{u(g_u)}}.$$

$$\tag{4.33}$$

Substituting Equation (4.33) in Equation (4.32), the resource allocation problem targets finding the group resource shares to be assigned to the S-UEs and NS-UEs:

$$\operatorname*{argmax}_{\{\mu_S^G, \mu_S^B, \mu_{NS}^G, \mu_{NS}^B\}} \sum_{\substack{\forall u \in \mathcal{A}_{c1} \\ g_u = S}} \log\left(\frac{\mu_S^G \cdot \mathcal{F}(\gamma_u^{\prime G}) + \mu_S^B \cdot \mathcal{F}(\gamma_u^{\prime B})}{N_{c1}^{u(S)}}\right) + \sum_{\substack{\forall u \in \mathcal{A}_{c1} \\ g_u = NS}} \log\left(\frac{\mu_{NS}^G \cdot \mathcal{F}(\gamma_u^{\prime G}) + \mu_{NS}^B \cdot \mathcal{F}(\gamma_u^{\prime B})}{N_{c1}^{u(NS)}}\right)$$

$$\text{subject to:} \qquad \mu_S^G + \mu_{NS}^G = \beta^R, \qquad \mu_S^B + \mu_{NS}^B = 1 - \beta_{c2},$$

$$\mu_S^G, \mu_S^B, \mu_{NS}^G, \mu_{NS}^B \geq 0.$$

$$\tag{4.34}$$

In fact the grouping of UEs is applied based on the sensitivity metric to schedule as many S-UEs as possible in the protected radio subframe while the inner cell data transmission is muted. Furthermore, the sensitivity threshold Γ^{Thr} requires timely calibration depending on the available fraction of G-subframe resources and by monitoring the nature of the spatial distribution of the UEs in the critically interfered sensitive region. Thus, a closed form expression can not be easily derived for Γ^{Thr}, hence, an iterative approach is utilized to select the optimal sensitivity threshold Γ_{opt}^{Thr} maximizing the cell utility based on an average statistical behavior over a fixed time window, i.e.

$$\operatorname*{argmax}_{\mu_S^G, \mu_S^B, \mu_{NS}^G, \mu_{NS}^B} U_{c1}\big|_{\Gamma^{Thr} = \Gamma_{opt}^{Thr}},$$

$$\text{subject to:} \qquad \mu_S^G + \mu_{NS}^G = \beta_{c2}, \qquad \mu_S^B + \mu_{NS}^B = 1 - \beta_{c2} \qquad \tag{4.35}$$

$$\mu_S^G, \mu_S^B, \mu_{NS}^G, \mu_{NS}^B \geq 0$$

4.4.4 Optimization of Radio Subframe Blanking Pattern

This section presents the optimization of the blanking pattern to enable adaptive VS-eICIC.

A fixed blanking pattern might be suboptimal in terms of the overall system performance as the configured blanking pattern β_{c2} takes usable resources from the inner cell and brings substantial negative impact. Essentially, the optimal β_{c2} configuration requires to properly redistribute the total available radio resources between the vertical cells by taking the load imbalance at the individual cell into account. In order to overcome this problem and adapt the VS-eICIC according to the cell load situation, a joint blanking pattern optimization problem is defined which maximizes the combined utility of the aggregate of the cell described by $U_a = U_{c1} + U_{c2}$ in a coordinated manner while satisfying the resource allocation strategy discussed earlier at the outer cell, i.e.:

$$\underset{\{\mu_S^G, \mu_S^B, \mu_{NS}^G, \mu_{NS}^B\}}{\operatorname{argmax}} U_a|_{\Gamma^{Thr} = \Gamma^{Thr}_{opt}},$$

$$\text{subject to:} \quad \mu_S^G + \mu_{NS}^G + \mu_S^B + \mu_{NS}^B = 1 \tag{4.36}$$

$$\mu_S^G, \mu_S^B, \mu_{NS}^G, \mu_{NS}^B \geq 0,$$

where the utility at each cell is defined as a function of the unknown group resource shares of the outer cell as:

$$U_{c1} = \sum_{\substack{\forall u \in \mathcal{A}_{c1} \\ g_u = S}} \log\left(\frac{\mu_S^G \cdot \mathcal{F}(\gamma_u'^G) + \mu_S^B \cdot \mathcal{F}(\gamma_u'^B)}{N_{c1}^{u(S)}}\right) + \sum_{\substack{\forall u \in \mathcal{A}_{c1} \\ g_u = NS}} \log\left(\frac{\mu_{NS}^G \cdot \mathcal{F}(\gamma_u'^G) + \mu_{NS}^B \cdot \mathcal{F}(\gamma_u'^B)}{N_{c1}^{u(NS)}}\right)$$

$$\tag{4.37}$$

$$U_{c2} = \sum_{\forall u \in \mathcal{A}_{c2}} \log\left(\frac{1 - (\mu_S^G + \mu_{NS}^G)}{N_{c2}^u} \cdot \mathcal{F}(\gamma_u')\right) \tag{4.38}$$

Having the group resource shares from Equation (4.36), the optimal blanking pattern to be configured at the inner cell is computed as $\beta_{c2} = \mu_S^G + \mu_{NS}^G$.

The optimization of the blanking pattern can be done in an automated manner based on the load situation in the network that supports a self-organizing feature. To enable a VS-eICIC operation with adaptive β_{c2} configuration, SON based optimization of β_{c2} is developed and presented in the system automation Section of Chapter 7 along with dynamic sectorization scheme.

4.5   Supercell Deployment with Vertical Sectorization

Motivated by the incursion of the high inter-cell interference when VS is simultaneously activated at all co-sited sector-antenna, a different sectorization approach in a vertical dimension is proposed as an alternative options. The section describes the operation mode of the proposed sectorization type and explains the drawback of the VS approach that has been being discussed so far.

Yet another deployment variant with respect to the VS is the so-called Supercell, where a single inner cell called VS-Supercell (VS-S) is created by assigning identical cell IDs to all co-sited inner cells and transmitting the same signal through them. This scheme provides a virtually combined sector antenna transmission which acts as quasi-omni directional operation. The advantages of this configuration are having a better balanced coverage by having a largerVS-Supercell compared to the normal VS inner cell and reduced co-channel interference. The Supercell is realized by a simulcast transmission of identical signals on all three inner cell from the same baseband unit (BBU) as well as by combining and jointly processing the signals received by each sector antenna [ADG$^+$96, hp09].
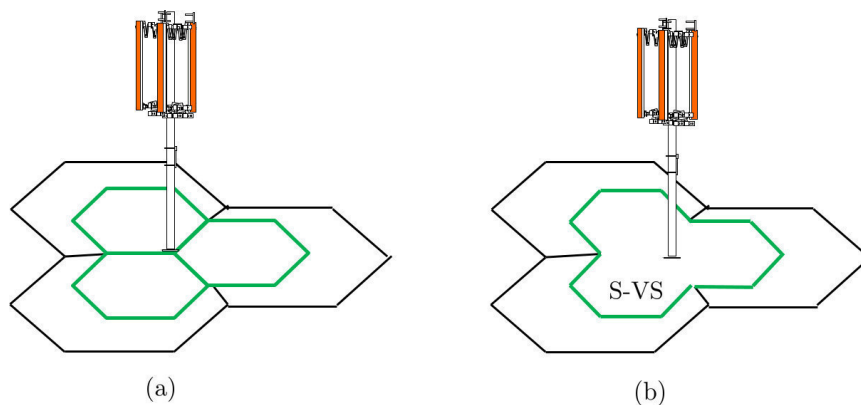
Figure 4.6. Vertical Sectorization: (a)Full VS, (b)VS-Supercell (VS-S)

As can be observed in Equation (4.12) and (4.23), the VS performance is challenged by the increased intra-site co-channel interference. Particularly, when all co-sited inner cells are simultaneously activated, the total interference from the co-sited inner cells indicated by ψ^u gets worse for the inner cell UEs. This interference impact becomes severe at the area of the inner cells where the superposition of the radiation from the side and back lobes of the aggressively down-tilted inner cells' beams is dominant

[KWVK14a] [KWVK14b]. Unlike to the full VS which multiplies the radio resource via a higher order densificaiton, the VS-S operation introduces only one additional cell, i.e. number of resources is not doubled but increased by 1/3 only. The schematic cell layout representation for the vertical sectorization with Supercell configuration is depicted in Figure (4.6) in comparison to the VS approach discussed so far and will be referred as full VS henceforth.

With the Supercell configuration, the digital base band signal is split up and transmitted through all co-sited sector-antenna and the corresponding RF modulated signal is sent over the inner cells' beams that are broadcasting identical cell ID. Consequently, since a user receives replicas of identical signals from each beam, the total serving signal power $P^u_{s(u)}$ becomes the superposition of all the signal received from each cells's AAS yielding a better quality of the desired signal power as long as all the replicas are received within a time delay not longer than the cyclic prefix (CP) of the OFDM symbol [HT09]. Accordingly, assuming the super-cell is activated at site q, the desired signal power received by UE u when served by the super-cell, $P^u_{s(u)}$, is expressed as

$$P^u_{s(u)} = \sum_{\substack{c \in \mathcal{C}, Q(c)=q \\ b_{A(c)}=2}} P^u_c. \tag{4.39}$$

The Supercell coverage dominance criterion and best server cell association of user are modeled the same way as described in Equation (4.8) but using a new relative signal power strength measure criterion designated by $\kappa^u_{2,1(\text{VS-S})}$. Depending on to which outer cell side UE u is located in the coverage layout, as depicted in Figure (4.6) (b), the corresponding $\kappa^u_{2,1(\text{VS-S})}$ is computed as,

$$\kappa^u_{2,1(\text{VS-S})} = \frac{\sum\limits_{\substack{c \in \mathcal{C}, Q(c)=q \\ b_{A(c)}=2}} RSRP^u_c}{RSRP^u_{c1}} = \kappa^u_{2,1} + \frac{\sum\limits_{\substack{c \in \mathcal{C}, Q(c)=q \\ b_{A(c)}=2, c \neq c2}} RSRP^u_c}{RSRP^u_{c1}}. \tag{4.40}$$

Owing to the fact that $\kappa^u_{2,1(\text{VS-S})} > \kappa^u_{2,1}$, see Equation (4.40), the Supercell configuration always guarantees a stronger and an improved service coverage compared to the full VS for the areas where the inner/inner boundaries are eliminated. In fact the Supercell implementation intrinsically provides a wider single inner cell coverage comparable to an outer cell thereby providing better traffic load balance among the co-sited cells unlike to the full VS where the inner sectors' coverage span smaller area creating coverage imbalance and uneven load distribution in the system [KWVK14a].

Besides, since the joint transmission scheme over the Supercell effectively avoids the interference between the co-sited inner cells, the deployment substantially mitigates the overall system interference and enhances the SINR performance of UEs located
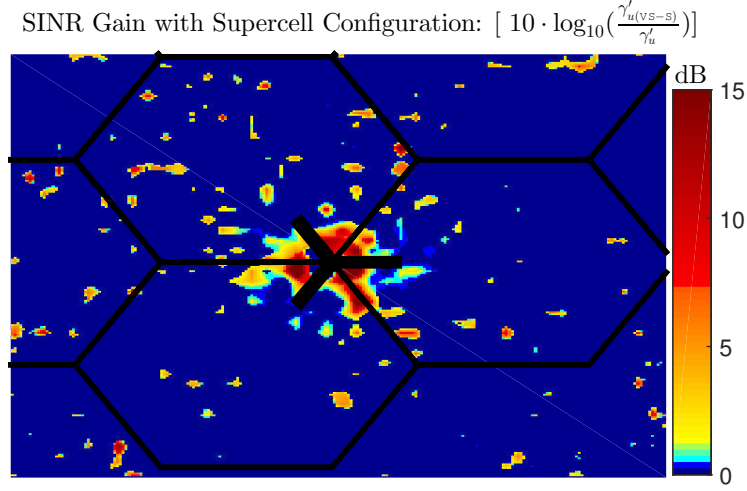
SINR Gain with Supercell Configuration: $[\ 10 \cdot \log_{10}(\frac{\gamma'_{u(\text{VS-S})}}{\gamma'_u})]$

Figure 4.7. SINR Improvement with Supercell Configuration

within the vicinity of the the inner cell region. Accordingly, the SINR of UE u served by the Supercell with VS-S denoted by $\gamma'_{u(\text{VS-S})}$ is modeled as,

$$\gamma'_{u(\text{VS-S})} = \frac{\sum\limits_{\substack{c \in \mathcal{C}, Q(c)=q \\ b_{A(c)}=2}} P_c^u}{\sum\limits_{\substack{\forall a \in \mathcal{Q} \\ b_a=0 \\ Q(c) \neq Q(s(u))}} \sum\limits_{\substack{\forall c \in \mathcal{C} \\ A(c)=a}} \varsigma_c \cdot P_c^u \cdot [1 - l_a \cdot (1 - \frac{\alpha_{a,1}}{\alpha_{a,0}})]\ \ + \varsigma_{c1} \cdot P_{c1}^u}. \tag{4.41}$$

From Equation (4.14) and (4.41), the SINR performance of UE u achieved with the Supercell configuration can be expressed compared to the γ'_u, with $\frac{\gamma'_{u(\text{VS-S})}}{\gamma'_u} > 1$ as,

$$\frac{\gamma'_{u(\text{VS-S})}}{\gamma'_u} = (1 + \psi^u) \cdot \frac{(\alpha_{a,0} + \alpha_{a,1} \cdot \gamma_u \cdot [\varsigma_{c1}\ \ + \ \kappa_{2,1}^u \cdot \psi^u])}{\alpha_{a,0} + \alpha_{a,1} \cdot \gamma_u}. \tag{4.42}$$

Since $\psi^u > 1$, it can be seen from Equation (4.42) that the UE SINR with VS-S is always improved for those inner cell UEs, moreover, the achieved SINR gain significantly increases while getting closer to the BS as the value of ψ^u is gets higher. The SINR performance comparison achieved with the Supercell configuration compared to the full VS case is demonstrated in Figure (4.7) for $\alpha_{a,1} = \alpha_{a,0}$. As can be observed in the figure, the SINR of the the inner most region (the Supercell area) is enhanced substantially.

In real propagation environment, apart from the critical interference problem due to the denser deployment, the inner most cell coverage region is randomly dominated by any of the inner cells. This is due to the fact that the side and the back lobes of all co-sited cells can get randomly dominant causing a fragmented cell coverage thereby
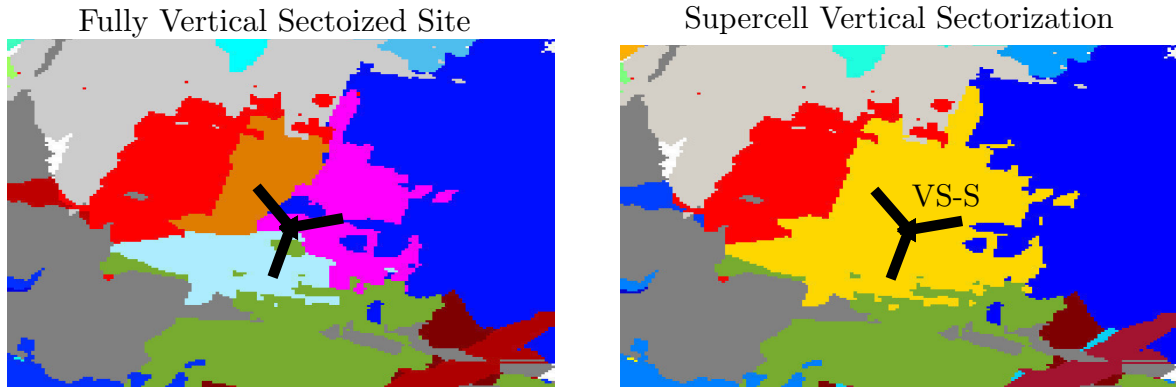
Figure 4.8. RT-Scenario: Best Server Map Comparison for Full VS and VS-S

creating more cell boundaries as demonstrated with the best server map plot in Figure (4.8).

This situation is examined extensively using the ray tracing based 3D model scenario where real antenna beam pattern data is utilized. The impact of such fragmented sector boundaries with respect to mobility related network operation is investigated thoroughly and the related performance evaluations and analysis are examined. The Supercell deployment study have been carried out to contribute an alternative concept and approach for the SON-based activation/deactivation operation to be discussed in later section. Detail performance analysis and results of the Supercell investigation are documented by the author and can be referred in [KWVK14b].

4.6   Performance Evaluation and Analysis

This section discusses the performance of the vertical sectorization for various system parameter settings.

The different performance determining factors derived in the developed VS model in Section 5.3 have been analyzed in detail for diverse spatial user distribution behavior. The limitation to the VS performance with respect to different behaviors of the spatial UE distribution, i.e. uniform and non-uniform cases, is demonstrated along with the achievements of the developed interference-coordination scheme, VS-eICIC, illustrating the situations when and where the foreseen VS performance can be delivered. For the aforestated reason, the total transmit power share at the inner/outer cell is considered equal, i.e. $\alpha_{a,1} = \alpha_{a,0}$. The scenario layout and the UE distribution type utilized

for the performance analysis is presented in Figure 4.9 with the best server map for inner/outer cells. The various UE distribution cases including traffic hotspot placed at different spatial location which contains 50% of the total number UEs from the coverage area served by a sector-antenna $\mathcal{A}_a$ is assumed.

The structure of this section is as follows. Section 4.6.1 presents the performance VS for varies parameter settings without employing the developed interference coordination scheme. The detail VS performance analysis when the VS-eICIC is integrated is presented in Section 4.6.2.

4.6.1 Performance of Vertical Sectorization without Inter-Cell Interference Coordination

This section discusses the performance of VS without including the developed Inter-Cell interference coordination scheme.

As described in Equation 4.15, the overall system throughput performance with VS is determined by the trade-offs between the radio resource gain and the degradation due to the co-channel interference impact. The primary investigation examines the impact of the beam paramters' settings on controlling the inner/outer cell UE load distribution and the level of the inter-cell co-channel interference utilizing a uniform spatial UE distribution assumption as shown in Figure 4.9 Case-1.
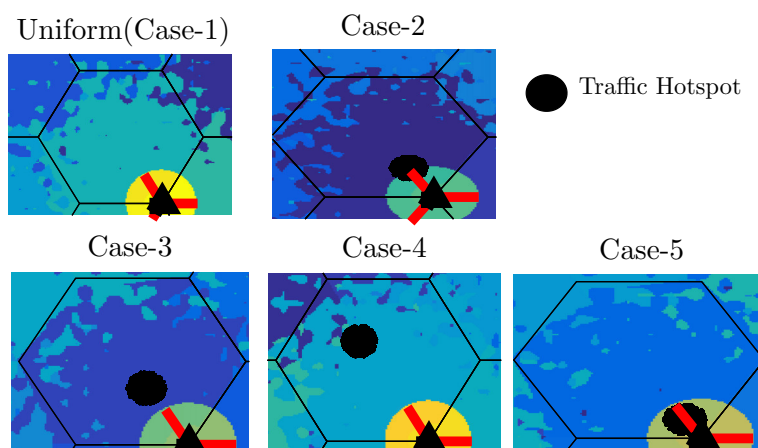

Figure 4.9. Uniform and Non-Uniform Spatial UE Distribution Scenarios

The first study deals with the beam offset setting, $\Theta_{2,1}^a$, between the beams of the inner and outer cells while maintaining equal elevation HPBW settings, $\Theta_{3dB}^{c1} = \Theta_{3dB}^{c2} = 5°$,

i.e. $\Xi = 1$. The $\Theta_{2,1}^a$ setting is varied by changing the elevation tilt of the inner cell, $\Theta_{c2} \in \{9°, 11°, 13°, 15°, 17°\}$, whereas the outer cell elevation tilt setting is fixed to an optimized value of 5° for aforementioned reason, see [KWVK14a]. The cell throughput (TP) performance from the individual inner/outer cells and from the aggregate of the cells (Inner+Outer) are used as evaluation criterion as depicted in Figure 4.10 for various beam parameter settings. Since the outer cell border is not changing due to the fixed tilt setting, the inner/outer cell load redistribution is mainly determined by the relative coverage size of the inner cell. As illustrated in Figure (4.10) (a), the total cell throughput, $\sum \tau_u$, at the inner cell diminishes as the $\Theta_{2,1}^a$ is increased for the fact that the inner cell coverage size is proportionally reduced, see Figure 4.3. High value of $\Theta_{2,1}^a$ introduced by adjusting the inner cell tilt dramatically boosts the total throughput performance of the aggregate of the cells by favoring a better interference situation for the majority of the outer cell UEs as the corresponding $\kappa_{2,1}^u$ value gets lower.

However, too high $\Theta_{2,1}^a$ setting significantly degrades the aggregate throughput performance as further shrinking the inner cell coverage reduces the number of UEs which have good throughput performances contributing to the cell throughput. Furthermore, the inner cell shrinking causes a deterioration of the resource share gain achieved by the outer cell UEs due to the additional cell load pushed to the outer cell. Based on the parameter sweeping, the offset $\Theta_{2,1}^a = 6°$ is found to be a setting that maximizes both the total and the average user throughput performances over the aggregate area of the cells and this exhibited in Figure (4.10).

In addition, the vertical HPBW can be seen as a parameter to optimize the coverage imbalance between the inner and outer sector. As demonstrated in Section 5.3, in limited cases, wider inner beam promises to yield better resource gain by increasing the coverage dominance of the inner cell. In conjunction with the tilt change, the impact of HPBW study is explored for wider inner cell beam setting case at $\Xi = 2$.

The corresponding results presented in Figure (4.10) (b) illustrate that wide inner beam maintains the total inner cell throughput performance almost unchanged despite the tilt change variation. However, the outer cell performance has declined as compared to $\Xi = 1$ case for moderate tilt offset, as indicated in Figure (4.10) (b). This is due to the fact that the co-channel interference level received at the outer cell from the inner gets worse resulting from the higher beam overlap. As a consequence, larger offset $\Theta_{2,1}^a$ is required to isolate the beams and alleviate the impact. An offset setting $\Theta_{2,1}^a = 10°$ is found to provide enough cell beam isolation maximizing the system performance. Figure (4.10) (c) demonstrates the average UE throughput performance comparison for both HPBW setting cases. It can clearly be seen in Figure (4.10) that narrower and equal HPBW setting outperforms the unequal (wider inner beam) setting.
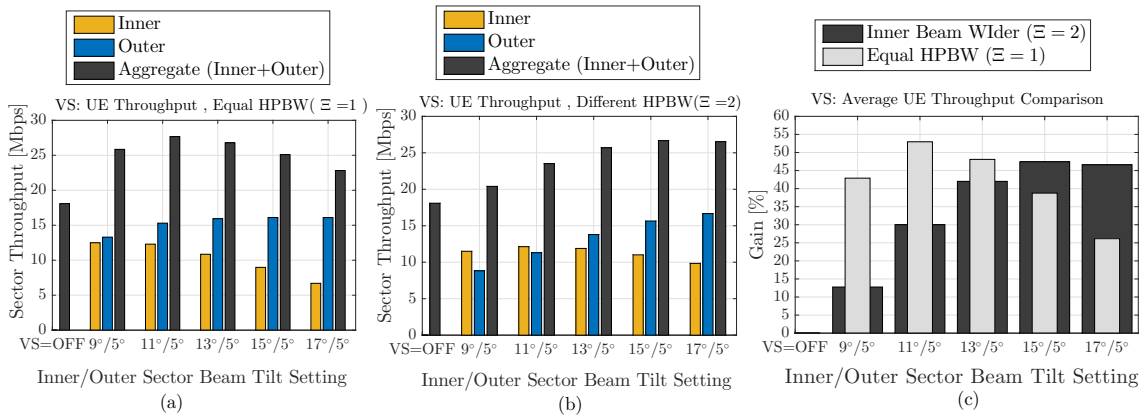
Figure 4.10. Impact of Sector Beam Parameters on VS Performance

Moreover, the performance of the later setting is substantially impacted by the inter-cell interference problem. Consequently, equal narrow HPBW and offset $\Theta_{2,1}^{a} = 6°$ setting are selected as suitable cell beam parameter settings, henceforth, for the remaining VS investigation.

The other VS study investigates the impact of the spatial distribution of UEs on the system performance assuming the realistic non-uniform distribution cases, (Case-2 to Case-5 as illustrated in Figure (4.9). For each UE distribution case of different UE locations, a fixed inner/outer cell coverage is maintained and the VS performance while positioning the traffic hotspot at different location is, heavily, impacted by the level of the experienced SINR degradation.

The hotspot locations at the highly interfered sensitive outer cell regions close to the inner/outer border, depicted in Case-2 and Case-3, are detrimental. From the UE performance analysis within the aggregated cell area, i.e. combining the throughout statistics of all UEs served within the inner and the outer cell, the achieved UE throughput values corresponding to different CDF percentiles level, $\omega\%$, ($\text{TP}^{\omega\%}$) and average (TP^{avg}) performances are reported in Figure (4.11).

As can be observed in the figure, the VS performance is substantially degraded for Case-2 and Case-3 due to the critical interference situation where losses of 28% and 22% are recorded, respectively, at the 50%-ile UE throughput CDF level compared to the VS=OFF case. Moreover, the average UE throughput performances have also sharply declined that only marginal gains are observed in Case-2 and Case-3 owing to the very few inner cell UEs having peak throughput. For the Case-4 where the traffic hotspot is located far away in the non-sensitive region, the the VS gain is less-significant. On the other hand, the UE distribution situation demonstrated by Case-5
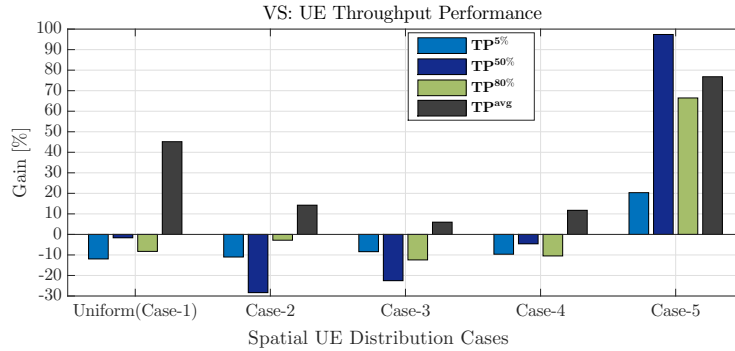
Figure 4.11. Impact of spatial UE distribution on VS performance

is a particular scenario in which VS considerably improves the UE throughput at all CDF percentiles due to the fact that the inner cell accommodates approximately 50% of the total conventional cell load providing a double the resource share (100% gain) for all UEs residing in both inner/outer cells. This analysis have indicated that, the VS performance highly depends on the nature of the spatial user distribution, hence, the VS activation requires proper analysis and decision prior to executing the sectorization.

4.6.2   Performance of Vertical Sectorization with Inter-sector Interference Coordination

This section provides the VS performance analysis by employing the VS-eICIC scheme to coordinate the inter-cell interference.

The developed interference coordination technique, VS-eICIC, is employed to effectively deal with the impact of the co-channel interference described in the previous subsection. For each traffic hotspot scenario shown in Figure (4.9), the UE sensitivity level Γ_u^a is examined over the aggregate coverage area, $\mathcal{A}_a$, and used as a criterion for sensitivity-based user grouping analysis. The sensitivity CDFs depicted in Figure (4.12) (a) clearly show that high percentage of the aggregate of the cells' UEs in Case-2 and Case-3 are critically interfered, hence, are exhibiting high sensitivity values. For example, 50% of the UEs in Case-2 are reporting a significant sensitivity level while over 20% are critically interfered experiencing a 50% loss in the spectral efficiency performance, exhibited on the Γ_u^a value.

In contrast, the sensitivity CDF of Case-5 is almost identical to the uniform case, Case-1, as their corresponding outer cell UEs are uniformly distributed. On the other hand, since the hotspot in Case-4 is positioned in the non-sensitive region, the sensitivity

Figure 4.12. VS-eICIC with fixed blanking pattern

level of most of the UEs is very small. As explained in the VS-eICIC modeling section, Section 5.4, the sensitivity-based user grouping operation is performed by selecting a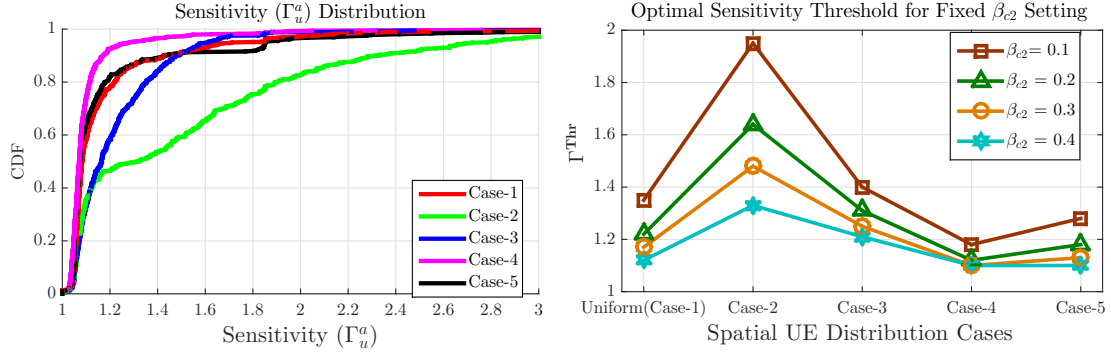s many severely interfered UEs as possible depending on the available fraction of subframes, β^{R}, muted at the respective inner sector.

The value of $\Gamma_{\mathrm{opt}}^{\mathrm{Thr}}$ to be used for categorizing UEs to each sensitivity group is determined during scheduling time by monitoring the defined cell utility function, as discussed in Equation (4.25) and Equation (4.35). In order to demonstrate the inter-relationship between the Γ^{Thr} and the blanking pattern, simulation results with sweeping the value of $\beta_{c2} \in \{0.1, 0.2, 0.3, 0.4\}$ are considered for all the five show case scenarios and the results are presented in Figure (4.12) (b). As expected, lower Γ^{Thr} value accommodates more UEs into the sensitive UE group when the configured β_{c2} is increased, irrespective of the UE distribution. As illustrated in Figure (4.12) (b), a rather high Γ^{Thr} value is needed in Case-2 for small blanking setting, $\beta_{c2} = 0.1$, due to the fact that only few of the critical UEs can be accommodated. The sensitivity threshold drops more as indicated with an increase of the blanking pattern to $\beta_{c2} = 0.4$. For the non-sensitive scenario, Case-4, the Γ^{Thr} remain more or less the same irrespective of the β_{c2} setting. Furthermore, no significant changes are observed in Case-1 and Case-5, due to the uniformity of their outer cell user distribution.

The optimal β_{c2} that yields the maximum system performance is adapted based on the sensitivity level reports which vary according to the underlying spatial distribution of the UEs. In general, blanking the inner cell brings overall system benefit when the inner cell is not heavily loaded so that it has a spare radio resources to offer for the coordination and simultaneously there are classified sensitive UEs at the corresponding outer cell to be scheduled during the interference protected subframes. Applying the developed blanking pattern optimization model, discussed in Section 5.4, the optimal β_{c2} values are obtained and shown in Figure (4.13). For instance, in Case-1, 40% of

the resources of the inner cell ($\beta_{c2} = 0.4$) can be muted to provide 40% good SINR resources at the corresponding outer cell. Despite the critical situation in Case-2, the optimal β_{c2} found is even lower, $\beta_{c2} \approx 0.3$, due to the high load situation at the inner cell as is it serving the portion of the hotspot region. Light load situation at the inner cell and the presence of hotspot UEs at the outer cell drives rather high β_{c2} values in Case-3 and Case-4. In contrast, the inner-cell of Case-5 can not afford to blank some of its resources as it is heavily loaded due to the presence of hotspot traffic, therefore, the blanking pattern obtained is $\beta_{c2} \approx 0$.
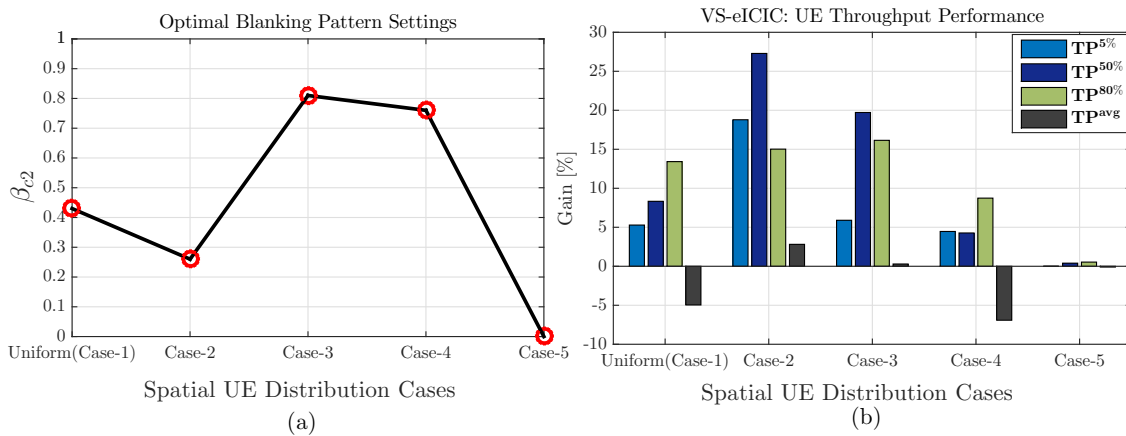
Figure 4.13. Performance of VS-eICIC with optimal blanking pattern

The performance of VS-eICIC compared to the traditional VS (VS-Only) is analyzed by examining the achieved UE throughput statistics from the aggregate coverage area for each UE distribution cases. In Figure (4.13) (b), the performance gain of VS-eICIC evaluated with respect to the VS-Only case is presented utilizing the various throughput CDF percentile values as a measure of performance metrics. Except for scenario in Case-5, the VS-eICIC outperforms the VS-Only by delivering additional significant performance gain. A marginal gain of around 5% is reported for cell-edge UEs reflected at the 5%-ile CDF level for Case-1, Case-2 and Case-4 whereas this gain is significantly higher, 15%, in Case-2, as severely affected hotspot UEs at the inner/outer sector border are benefiting a lot from the VS-eICIC. Furthermore, the VS-eICIC provides substantial throughput gains at higher CDF percentile which is manifested in Case-2 and Case-3 where the hotspot UEs are positioned in the interference sensitive region. Gains of more than 25% and 15% are achieved at the 50%-ile CDF level for each cases, respectively. For Case-4, however, since the hotspot is located far in the non-sensitive area, only minor performance enhancement is obtained from the applied VS-eICIC. It is worth noting that, in all scenarios but Case-2, the average throughput performance of the aggregate sector has deteriorated marginally with VS-eICIC and

this is the price which has to be paid-off as the transmission blanking reduces the high resource shares of the over-performing UEs of the inner sectors. In overall, the VS-eICIC utilizes the extra resource shares from the inner sector UEs to enhance the performance of the sensitive outer sector UEs in order to bring a balanced system performance over the aggregate sector.

Chapter 5

Horizontal Sectorization

5.1 Introduction

With Horizontal Sectorizaiton (HS), the cell count served by a single sector-antenna is increased by simultaneously creating two horizontally directed beams having narrower beam width configuration in the azimuth domain compared to the wide beam used for conventional sectorization. The horizontal beams are spatially separated by controlling the orientation of each beam via adjusting the respective azimuth steering angle settings. This type of sectorization is applicable in a capacity-strapped area where users are spatially distributed in the horizontal direction over the conventional cell coverage area. Unlike to VS which can be applied by activating an additional inner beam corresponding to the inner cell, HS involves replacing the conventional cell with two new cells having different cell-specific configurations. This chapter presents the model for HS describing the relationships between the various cell-specific parameter configurations and explains their impact on the system performance. The performance analysis of HS is carried out in terms of the introduced coverage layout change, the intra-site inter-cell interference and its impact on the user's SINR performance based on simulation results in conjunction with detailed discussions.

The structure of the Chapter is as follows. Section 5.2 provides the the sectorization model for the HS presenting the horizontal cell layout and describing the relationship between the SINR performance of a user before and after HS to be used for further HS performance study. In Section 5.3, factors which determine the performance of HS are discussed. In subsequent section, Section 5.4, the performance evaluations and analysis are presented.

5.2 Horizontal Sectorization Model

5.2.1 Horizontal Cell Layout and Parameters Settings

This section describes the cell layout and parameter settings for the HS.

In HS procedure two new cells are formed by simultaneously activating two horizontal beams designated by index $b_a = 1$ and $b_a = 2$ and, likewise to the VS, each beam is assigned a unique Cell ID. In fact the coverage overlap between the new cells is controlled by adjusting the azimuth steering angle Φ_c, $c \in \{c1, c2\} \subset \mathcal{C}$, and the HPBW settings, $\Phi_{3dB}^c < \Phi_{3dB}^{c0}$, where $c0$ refers to the index of the conventinal cell being replaced during the HS. Proper beam parameters setting enable to focus the radiation of the corresponding cell beam towards the desired coverage area and to reduce the level of interference. Φ_c can generally be expressed in terms of an offset angle $\Phi_{c,c0}$ that has to be applied with respect to the corresponding conventional cell orientation Φ_{c0}, i.e. $\Phi_c = \Phi_{c0} + \Phi_{c,c0}$, hence, the total angular separation between the horizontal beams denoted by $\Phi_{c1,c2}$ is described as $\Phi_{c1,c2} = \Phi_{c1,c0} + \Phi_{c2,c0}$. The illustration for HS is shown with a diagram in Figure 5.1.
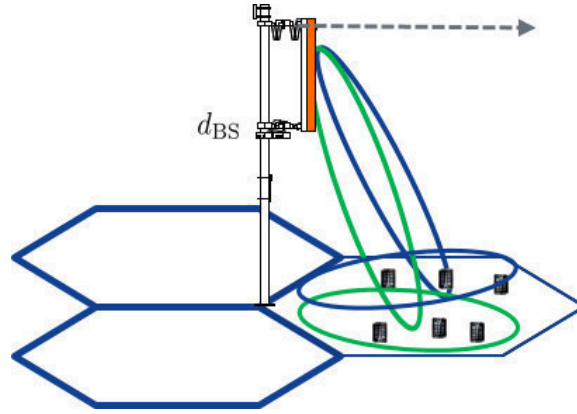
Figure 5.1. Horizontal Sectorization

As discussed in the system model section, since the number of array columns employed for the HS beamforming is twice compared to what is being used for the conventional case, the resulting HPBW of the horizontal cells in the azimuth domain is reduced by half, i.e. $\Phi_{3dB}^c = \frac{1}{2} \cdot \Phi_{3dB}^{c0}$. The two columns array configuration increases the directivity of the antenna and provides additional 3dB higher antenna gain on $G_c^{\max}$.

The total transmit power assigned for each cell can generally be described with the power sharing scheme defined for the VS case in Equation (2.20). Equal power allocation maximizes and balances the coverage dominance area of both horizontal cells due to the fact that the cell beams have identical elevation parameter settings and equal azimuth HPBW. Therefore it is reasonable to set the relative power split fact $\alpha_{c1} = \alpha_{c2}$ yielding equal total transmit power per beam.

While HS is executed, the UEs in the underlying coverage layout are handed over to one of the new cells which becomes dominant at UE's location. As the coverage dominance

of each cell is determined by the strength of the received signal power, likewise to VS, relative signal power strength criterion denoted by $k_{2,1}^u$ is computed using RSRP reports to determine the propagation link imbalance between the two new horizontal cells with respect to the same UE location,

$$\kappa_{2,1}^u = \frac{RSRP_{c2}^u}{RSRP_{c1}^u}. \tag{5.1}$$

The value of $k_{2,1}^u$ characterizes not only the relative strength of the serving cell's signal power but also expresses the level of interference created between the new cells. The best serving cell selection and association of UEs is defined in the same manner based on the $k_{2,1}^u$ criterion as explained in Equation 4.8. In HS $k_{2,1}^u$ is mainly determined by the azimuth domain radiation pattern characteristics of the beams. Besides, additional relative signal strength measurement criterion denoted by $k_{c,c0}^u$ is specified in order to relate the strength of the signal power received from the best serving cell of a UE after and before HS. This can be expressed as,

$$\kappa_{c,c0}^u = \frac{RSRP_c^u}{RSRP_{c0}^u} \propto \frac{G_c^u(\Phi_c, \Theta_c)}{G_{c0}^u(\Phi_{c0}, \Theta_{c0})}. \tag{5.2}$$

5.2.2 SINR Model for Horizontal Sectorization

In this section, the model describing the relationship between the user SINR performance before and after HS is explained.

Unlike to the VS case, the inter-cell interference situation with HS is more challenging as the two new horizontal cells not only interfere each other but also cause additional interference in the neighborhood. Therefore, the SINR model for HS requires to properly account any sectorization changes in the network in order to comprise the interference impacts within the inter-site domain as well. Considering activation of HS at the sector-antenna of index a, the SINR performance of UE u served by either of the horizontal cells denoted by γ_u' is generally expressed including all the inter- and intra-site additional interfering signals' power as

$$\gamma_u' = \frac{P_{s(u)}^u}{\displaystyle\sum_{\substack{\forall a \in \mathcal{Q} \\ b_a=0}} \sum_{\substack{\forall c \in \mathcal{C} \\ A(c)=a}} \varsigma_c \cdot P_c^u \cdot [1 - l_a] + \sum_{\substack{\forall a \in \mathcal{Q} \\ b_a=1}} \sum_{\substack{\forall c \in \mathcal{C} \\ c \neq s(u) \\ A(c)=a}} l_a \cdot \varsigma_c \cdot P_c^u + \sum_{\substack{\forall a \in \mathcal{Q} \\ b_a=2}} \sum_{\substack{\forall c \in \mathcal{C} \\ c \neq s(u) \\ A(c)=a}} l_a \cdot \varsigma_c \cdot P_c^u + P_N} \tag{5.3}$$

The derivation of the relationship between the SINR performance of UE u before and after HS activation is essential as it enables to estimate or pre-evaluate system

performance prior to execution and validation of HS change. From Equation 5.3, the expression for γ'_u as a function of γ_u is formulated substituting the additional interference impacts with $k^u_{2,1}$ and $k^u_{c,c0}$ parameters as shown below,

$$
\gamma'_u = \begin{cases} \dfrac{k^u_{c1,c0} \cdot \gamma_u}{k^u_{c1,c0} \cdot \left(k^u_{2,1} + \psi^u \right) \cdot \gamma_u + 1} & \text{if,} \quad \kappa^u_{2,1} \leq 10^{0.1 \cdot \chi_{hyst}} \wedge s(u) = c1 \\[3em] \dfrac{k^u_{c2,c0} \cdot \gamma_u}{k^u_{c2,c0} \cdot \left(\frac{1}{k^u_{2,1}} + \psi^u \right) \cdot \gamma_u + 1} & \text{if,} \quad \kappa^u_{2,1} > 10^{0.1 \cdot \chi_{hyst}} \wedge s(u) = c2, \end{cases} \tag{5.4}
$$

where ψ^u is the sum of the additional interference signal power received at u attributed to any sectorization changes occurring in the network normalized to the signal power of the serving cell, i.e.

$$
\psi^u = \frac{1}{P^u_{s(u)}} \cdot \left(\sum_{\substack{\forall a \in \mathcal{Q} \\ b_a = 1}} \sum_{\substack{\forall c \in \mathcal{C} \\ A(c) = a \\ A(c) \neq A(s(u))}} l_a \cdot \varsigma_c \cdot P^u_c + \sum_{\substack{\forall a \in \mathcal{Q} \\ b_a = 2}} \sum_{\substack{\forall c \in \mathcal{C} \\ A(c) = a \\ A(c) \neq A(s(u))}} l_a \cdot \varsigma_c \cdot P^u_c - \sum_{\substack{\forall a \in \mathcal{Q} \\ b_a = 0}} \sum_{\substack{\forall c \in \mathcal{C} \\ A(c) = a}} \varsigma_c \cdot P^u_c \cdot l_a \right) .
$$

$$\tag{5.5}$$

5.3 Factors Determining Performance of Horizontal Sectorization

5.3.1 Introduction

The performance of HS is examined by comparing the UE throughput achieved before and after the sectorization state change. The UE throughput gain evaluation approach performed for the VS case in Equation (4.15) is similarly employed for the HS as well to explain the achievable HS performance as a function of both the attainable resource gain, $\frac{R'_u}{R_u}$, and the experienced change in the SINR performance, i.e. $\frac{\gamma'_u}{\gamma_u}$.

In addition to the relative coverage size of each horizontal cell, the nature of the spatial distribution of the users over the underlying coverage area is a crucial factor in determining the resulting load redistribution between the new cells. Likewise to what is explained for VS with Equation (4.17), the load redistribution metric specified in Equation (4.17) is applicable to measure the relative number of connected UEs associated to each horizontal cells and to estimate the amount of resource fraction to be allocated.

5.3.2 Beam Parameter Setting

This section discusses the effect of the beam parameter settings in determining the performance of HS.

The coverage area the horizontal cells can be flexibly controlled by tuning the cell-specific beam parameters. This provides a mechanism to adjust the inter-cell coverage boundary as the coverage dominance is decided based on the value of $\kappa_{2,1}^u$. As defined by Equation (5.1), $\kappa_{2,1}^u$ is proportional to the relative antenna gain difference measured with respect to each beam, $\widehat{G_{2,1}^u}$, i.e.

$$\kappa_{2,1}^u \propto \widehat{G_{2,1}^u} = 10 \cdot \log_{10} \left(\frac{G_{c2}^u(\Phi_{c2}, \Theta_{c2})}{G_{c1}^u(\Phi_{c1}, \Theta_{c1})} \right). \tag{5.6}$$

$\widehat{G_{2,1}^u}$ in HS is predominantly determined by the characteristics of the radiation pattern of the beams in the azimuth plane and its expression using the related beam parameters is derived from the 3D radiation pattern model described by Equation (2.18),

$$\widehat{G_{2,1}^u} = -10 \cdot \log_{10}(\Xi) - \left(\frac{\Phi_{c1,c0} - \Phi_{c2,c0}) \cdot \left[2 \cdot (\phi - \Phi_{c0}) + \Phi_{c1,c0} + \Phi_{c2,c0} \right]}{\Xi \cdot \Phi_{3\text{dB}}^{c1}} \right) \tag{5.7}$$

where the relative azimuth HPBW of each sector beam is described in similar fashion like VS with $\Xi = \frac{\Phi_{3\text{dB}}^{c2}}{\Phi_{3\text{dB}}^{c1}}$. In contrast to VS, each beam in HS can be flexibly steered within a wide range of angles in the azimuth domain enabling better control of the individual beam direction to regulate the coverage dominance area. Accordingly, a cell-splitting procedure yielding a balanced coverage layout can be performed by adjusting the azimuth angle Φ_{HS} of the resulting inter-cell boundary where $\widehat{G_{2,1}^u} = 0$. A general expression for Φ_{HS} is derived incorporating the required steering angle offset of each beam and the azimuth HPBW setting as

$$\Phi_{\text{HS}} = \phi|_{\widehat{G_{2,1}^u}=0}, \tag{5.8}$$

$$= \Phi_0 - \frac{1}{2} \cdot \left(\frac{\Xi \cdot \Phi_{3\text{dB}}^{c1} \cdot 10 \cdot \log_{10}(\Xi)}{\Phi_{c1,c0} - \Phi_{c2,c0}} + (\Phi_{c1,c0} + \Phi_{c2,c0}) \right). \tag{5.9}$$

For the considered double column AAS array architecture, the azimuth HPBW of the horizontal beams are equal as discussed in Section 6.1 and aligning the Φ_{HS} to the orientation angle of reference conventional cell beam steering angle Φ_{c0}, i.e. $\Phi_{\text{HS}} = \Phi_{c0}$, enables to achieve a symmetrical coverage splitting. This can be achieved by steering each beams away from Φ_{c0} with the same offset angle, i.e. $\Phi_{c1,c0} = -\Phi_{c2,c0}$.

5.3.3   Inter-Cell Interference Between Horizontal Cells

This section investigates and evaluates the impact of the inter-cell interference that arises due to HS.

Similar to the VS case, the impact of the co-channel interference resulting between the two new horizontal cells is analyzed by examining the average SINR performance change experienced by a user employing the relationship provided with the HS SINR model described by Equation 5.3. Accordingly, the SINR change is expressed as

$$\Delta\widehat{\gamma_u} = 10 \cdot \begin{cases} \log_{10} k_{c1,c0}^u - \log_{10}\left(k_{c1,c0}^u \cdot (k_{2,1}^u + \psi^u) \cdot \gamma_u + 1\right), & \kappa_{2,1}^u \leq 10^{0.1 \cdot \chi_{hyst}} \\ \\ \log_{10} k_{c2,c0}^u - \log_{10}\left(k_{c2,c0}^u \cdot (\frac{1}{k_{2,1}^u} + \psi^u) \cdot \gamma_u + 1\right), & \kappa_{2,1}^u > 10^{0.1 \cdot \chi_{hyst}} \end{cases} \tag{5.10}$$

The expression for $\Delta\widehat{\gamma_u}$ indicates that the performance of UE's SINR with HS is proportional to the values of $k_{c1,c0}^u$ and $k_{c2,c0}^u$ computed at the respective UE location. In fact high values of $k_{c1,c0}^u$ and $k_{c2,c0}^u$ are achieved within the center of each horizontal cell coverage where the antenna gain measured from the newly activated cell beam is higher compared to what is measured with respect to the replaced conventional cell as described by Equation (5.2). Higher antenna gain value increases the strength of the desired signal power which potentially enhances the SINR performance. On the other hand, the area where the coverage of the two new horizontal cells is overlapping is characterized by a low values of $k_{c1,c0}^u$ and $k_{c2,0c}^u$, i.e. $k_{c1,c0}^u, k_{c2,c0}^u < 1$, besides the extreme inter-cell interference situation. As a consequence, UEs in this overlapping coverage region are significantly impacted and suffers from substantial SINR degradation, i.e. $\Delta\widehat{\gamma_u} < 0$, $\{\forall u | u \in \mathcal{A}_a, \max(k_{c1,c0}^u, k_{c2,c0}^u) < 1\}$.

Using the described expression, the behavior of $\Delta\widehat{\gamma_u}$ variation experienced by UE u after HS is illustrated in Figure (5.2). In contrast to VS where the user SINR performance is sensitive for new inner beam activation owing to the negative impact caused by the additional interference, HS may yield SINR improvement for the UEs which are spatially located away from the critically interfered overlapped coverage region, i.e. $|k_{2,1}^u| >> 1$, as exhibited in Figure (5.2).

5.4   Performance of Horizontal Sectorization

This section provides the analysis and evaluation of the performance of HS.
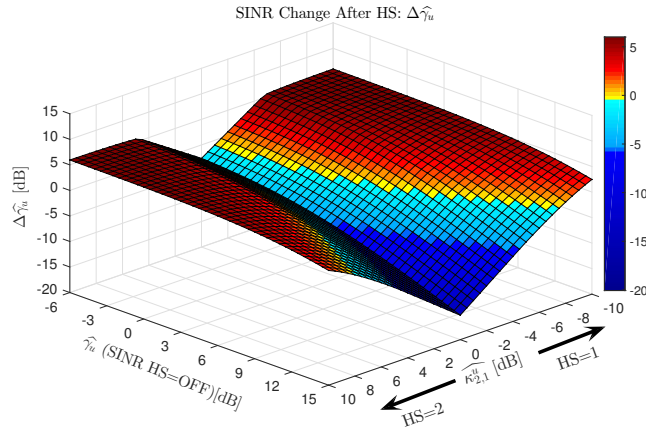
Figure 5.2. SINR change after HS

The analysis and evaluation of HS performance is carried out by investigating the impact of the system parameters utilizing the relationship developed in the HS model. For the purpose of this particular investigation, HS is activated to split the conventional cell at a single site considering the regular hexagonal cellular network scenario where users are assumed uniformly distributed. In the analysis, the impact of HS activation on the SINR performance is inspected for all UEs being served by the conventional cell undergoing the sectorizaiton and its first tier-neighbor cells.

The antenna gain values corresponding to the beams of the new horizontal cells in any direction within cells coverage area is shown in Figure 5.4, i.e. computed as $\{\forall u | u \in \mathcal{A}_a, \max(\widehat{G_{c1}^u}(\Phi_{c1}, \Theta_{c1}), \widehat{G_{c2}^u}(\Phi_{c2}, \Theta_{c2}))\}$.
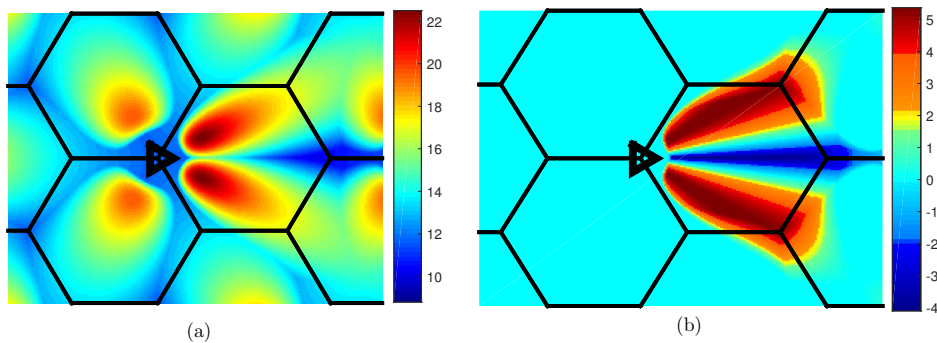
Figure 5.3. (a)Total antenna gain, (b)Antenna gain value difference after HS

As can be observed in Figure (5.4) (a), due to the narrower azimuth beam width con-figuration of the horizontal beams, users within each horizontal cell achieve relatively

a higher antenna gain in the respective beam boresight direction compared to the re-
placed conventional cell. This is justified in Figure (5.4)(b) where the difference in the
antenna gain values experienced within each serving cell coverage before and after HS
is depicted. This demonstrates that the HS indeed provides an improved antenna gain
performance in the boresight direction. On the contrary, the antenna gain experience
gets worse with HS within the cell coverage close to the inter-cell boundary of the
horizontal cells. As described by Equation(5.2), $\kappa_{c,c0}^u$ is related and proportional to the
antenna gain difference determining the relative strength of the serving signal power
of the new cells with respect to the conventional cell replaced due to HS.

Once HS is activated, the new coverage layout is determined based on the value of
$\kappa_{2,1}^u$ computed using the RSRP value measured with respect to each horizontal cell
and the UEs are associated to their best serving cell which becomes dominant over the
underlying coverage area according to the $\kappa_{2,1}^u$ value. As depicted in Figure (5.2) (a),
unlike to the VS case where unbalanced new cell coverages are created, the coverage
of both cells in HS spans over a wide area and their size is comparable to each other.
In fact the number of UEs connected to each cell is proportional to the size of the cell
coverage area for the typical case scenario where homogeneous spatial user distribution
is considered. Moreover, since the employed PF resource allocation strategy assigns
radio resource according to the total number of UEs connected to the individual cell, the
exhibited coverage balance between the new horizontal cells maximizes the achievable
resource gain from HS within both cells, i.e. $\frac{R_u'}{R_u}$.
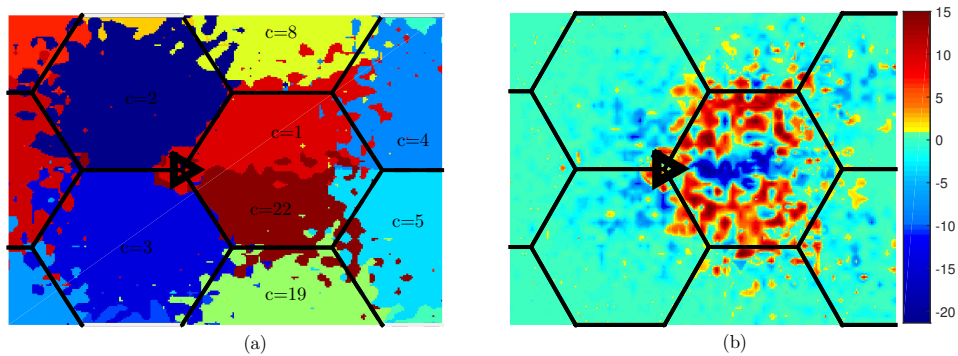
Figure 5.4. HS: (a) Best server map, (b)Change in SINR value

The comparison of the UE SINR performance achieved after and before HS activation
is conducted by evaluating the SINR difference, $\Delta\widehat{\gamma_u}$, for all UEs within the new as well
as within the neighboring cells surrounding the area undergoing the cell layout change.
Figure (5.4) (b) presents the map of the $\Delta\widehat{\gamma_u}$ values both on the cell that undergoes HS
and its neighboring cells which are indicated by their respective cell index. The $\Delta\widehat{\gamma_u}$

behavior explained with the model in earlier section according to Equation (5.10) is also demonstrated in Figure (5.4) (b) where a significant SINR gain is observed within the coverage of both horizontal cells. Whereas a substantial degradation of UE SINR performance is indicated as expected for UEs residing in the cell coverage area close to the border between the two horizontal cells. Moreover, with the proposed beam parameter and transmit power setting, the additional interference introduced with HS to the surrounding neighboring cells has been found to be minimal as illustrated with small SINR loss observed around the edge of the cells' coverage.

The throughput performance of a UE with HS, τ'_u, is computed based on the assigned resource share, R'_u, and the new SINR experience, γ'_u, applying Equation (2.62). As explained with the SINR model, the achievable τ'_u value can significantly vary depending on where the UE is spatially located within the cell coverage as a result of the exhibited SINR condition variation. For the performance comparison, the CDFs of the UE throughput statistics collected from the aggregate coverage area $\mathcal{A}_a$ is presented in Figure (5.4). As can be clearly seen in the figure, the UE throughput performance is substantially improved with HS and a throughput gain of about 100% is achieved at the 50%-ile CDF level. For the homogeneous UE distribution scenario, the impact of the critical SINR degradation that can be experienced around the cell border is reflected on the throughput CDF with a decline in the throughput performance for less than 5% of the UEs. It is worth noting that in realistic non-homogeneous UE distribution the presence of high fraction of UEs in such critically interfered area close to the inter-horizontal cell border region could potentially cause a deteriorated overall system performance. This explains the fact that the achievable user throughput performance gain with HS may rather vary considerably depending on the nature of the UE distribution.

Further analysis has been carried out to assess the impact caused by HS on the throughput performance of the UEs being served by the surrounding neighbor cells. As demonstrated in Figure (5.2) (a), the newly activated horizontal cells introduce a coverage overshoot within the neighboring cells in addition to the incursion of the additional interference that impacts the UEs' SINR which is depicted in Figure (5.2) (b). On the other hand, the coverage map evaluation have shown that only 85% of the conventional coverage area is replaced by the two new horizontal cells after HS activation. The remaining 15% coverage are taken over by the neighboring cells thereby introducing coverage change. Accordingly, the impact of HS both due to the introduced coverage change and the interference on the surrounding neighbors is examined by comparing the CDFs of the UE throughput statistics at the neighbor cells before and after HS, and the results are summarized in Figure (5.4). It can be observed in Figure (5.4) that visible performance degradation has been observed at cell $c = 4$ where on average 16%
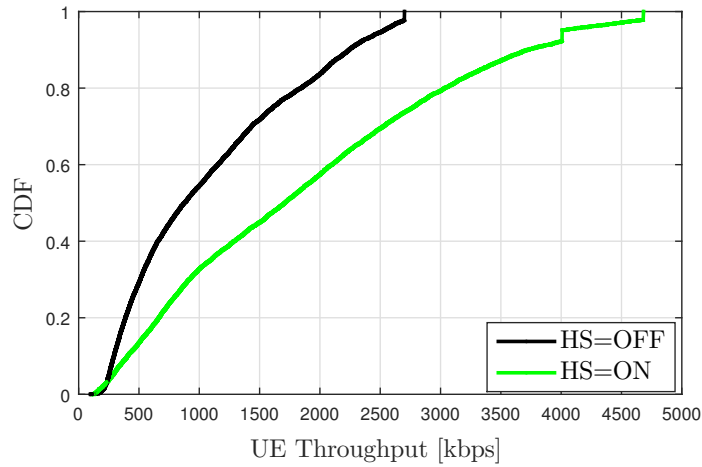
Figure 5.5. HS: UE throughput CDF comparison

throughput loss is recorded. This is due to the fact that cell $c = 4$ is directly impacted by the HS as it is located facing towards to the cell that undergoes the sectorization. To the contrary, the performance at cell $c = 8$ has achieved up to 14% improvement in the system throughput at higher CDF percentiles due to a better resource share as the coverage overshoot caused by the HS takes some of its load. In overall, the performance impact on the remaining surrounding neighbor cells is seen to be not critical and no significant deterioration in the system throughput is observed.
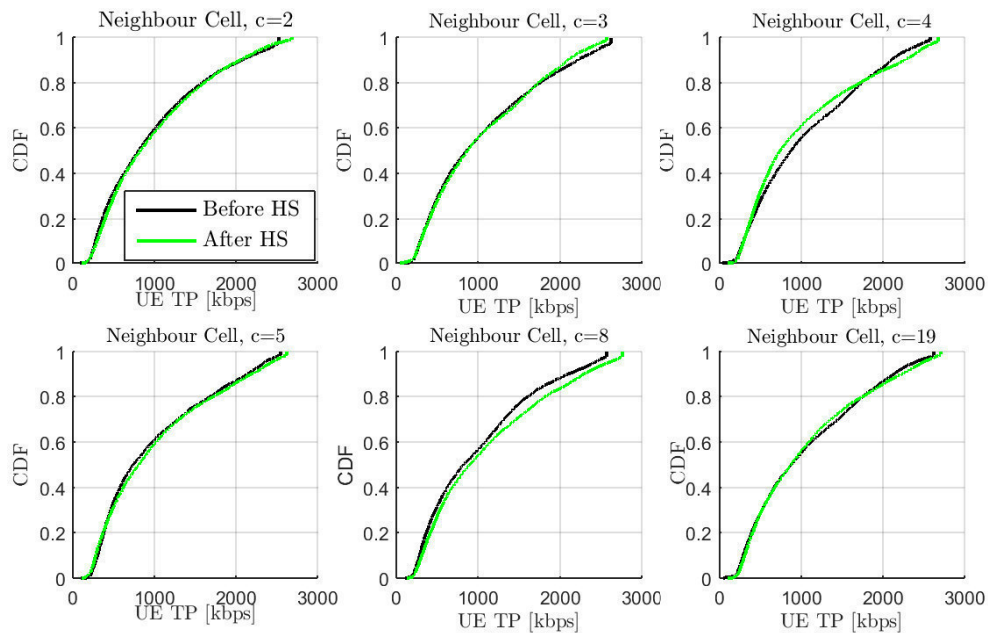
Figure 5.6. UE throughput CDF comparison of surrounding neighbor cells after HS

The presented HS model discussion and simulation result analysis demonstrated that, indeed, HS can significantly enhance system capacity by splitting the conventional cell coverages in to two cell coverages that are relatively balanced, compared to the VS case. However, in contrast to VS which can be executed while maintaining its outer cell and surrounding neighbor coverage border, HS recognizably causes a change in the coverage border of its own and neighboring cells. For this reason, the decision on executing HS requires careful attention as it could lead to unprecedented coverage layout change that might cause undesirable impact on the performance of neighbor cell(s).

Chapter 6

SON for Automated Sectorization

6.1 Introduction

Being intermittently variant overtime and space, the nature of real traffic distribution in cellular network is challenging the fixed deployment paradigm where the cell layout and system configurations remain fixed. The particular advantage of AAS-driven sectorization is the flexibility to adapt the cell layout to such temporarily and spatially varying traffic situation by activating/deactivating of new cells only when and where the extra capacity is needed. The dynamic reconfiguration of the AAS parameters for the on demand activation/deactivation of the new cells following the timely and locally varying user traffic is difficult to be handled efficiently by manual operation. This motivates the development for an automated mechanism in order to manage and carry out the appropriate sectorization procedures in a self-organized manner.

Driven by the AAS capability, dynamic sectorization has been seen as one of the AAS-use case scenarios that promises to provide flexible cell layout adaptation and is being discussed by 3GPP. The 3GPP radio access network (RAN) different work groups (WGs) have approved AAS related study and work items (SIs and WIs) to explore the RF and system level requirements to analyze the SON mechanisms for AAS based deployments.The SIs and WIs also discuss to provide standardized inter-node communications for automated sectorization (AS) without affecting service quality and ensuring seamless operation of the existing SON functionalities running in the underlying network [3GP12, 3GP13b]. Herein, the basic questions in the development of the SON framework are to define input triggering conditions and to specify the network informations to be used for network status evaluations with a decision criteria to yield a reliable SON mechanism. This aspect has been also highlighted in one of the SON-specific aspects discussed by 3GPP RAN3 SI proposed by [3GP13b].

In this chapter of the thesis, a SON framework that controls automated sectorization mechanism has been developed by integrating the sectorization models presented in Chapter 4 and 5. The SON framework specifies different procedures that relies on real time information collected from the network using actual measurement reports and defines analytical framework for the evaluation of a decision metric. In addition, SON-based automated interference-coordination mechanism mainly targeting on the

adaptation of the blanking pattern of radio subframe in the VS-eICIC scheme is proposed particular to the VS case.

The organization of the chapter is as follows. The SON architecture defined for the automated sectorization is presented in Section 6.2. Section 6.3 presents the SON function corresponding to the automated sectorization and a brief description of the different SON functional blocks. In Section 6.4, the SON function responsible for adapting the blanking pattern configuration in the VS-eICIC inter-cell interference coordination scheme is explained along with the algorithm description. Finally, the performance evaluation and analysis carried out using both the 3GPP-Scenario and RT-Scenario are presented and discussed in detail in Section 6.5.

6.2   SON Architecture for Automated Sectorization

This Section provides the SON architecture considered for the AAS-driven automated sectorization.

The SON architecture presented in this section describes the structure of the SON mechanism, the basic functional components of the SON function and the relationship among the functional blocks. Depending on the desired location to put the role of the SON mechanism in the network, the SON algorithms and functions can be located either inside a central unit in the Operation and Maintenance (OAM) domain or can be distributed in the radio access network employed in the base station which is equipped with AAS. As explained in the modeling section of Chapter 5, the AAS-based sectorization is intended to dynamically follow the local traffic density variation and capacity demand of an area served by a particular site and the SON action is intended to be performed without introducing unforeseen interruption of any user connection on own and on neighboring site. For this reason, a distributed SON-architecture where the local eNB is responsible for monitoring and decision role is considered. With a distributed SON architecture design, the SON function including the corresponding algorithm for the automated sectorization is assumed to be placed inside the eNB. Due to the fact that the sectorization process involves changing the cellular layout of the network of its serving area, an interaction mechanism between the SON functions in the eNB and the central OAM unit and/or other network elements like neighbor eNBS needs to be specified. The SON-arhitecture defined for the automated sectorizaiton depicting the required information exchange among the basic network components is presented in Figure 6.1.
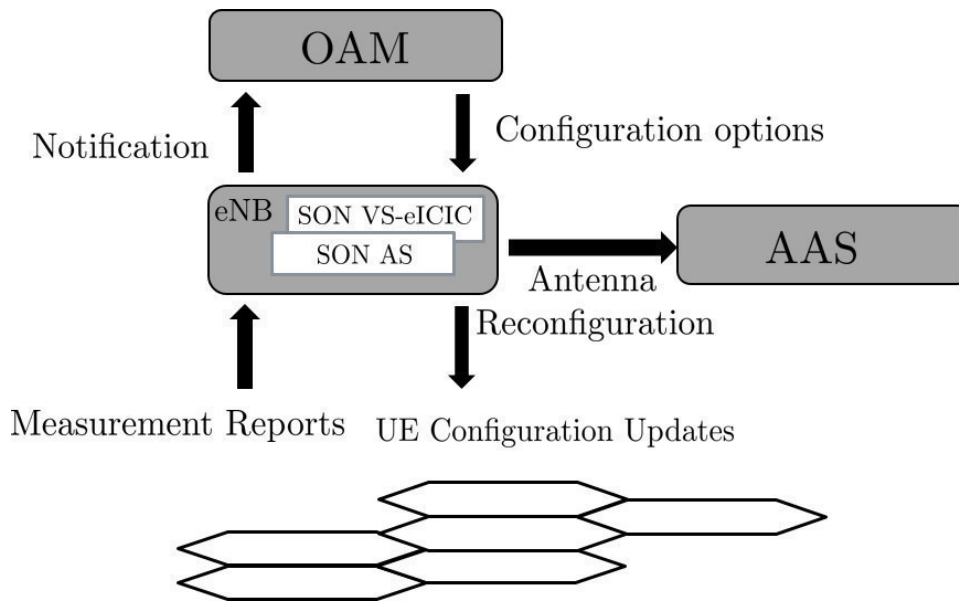
Figure 6.1. SON Architecture for Automated Sectorization

In Figure 6.1, two SON functions are embedded inside the eNB, i.e. SON-AS and SON VS-eICIC. The SON-AS is the SON function that controls the automated sectorization mechanism. Inside the SON-AS, different modules are defined that are responsible to carry out specific procedures whose detailed descriptions are provided in Section 6.3. The other SON function indicated inside the eNB, SON VS-eICIC, is used to automate the blanking pattern configuration to provide an adaptive interference-coordination mechanism using the developed VS-eICIC scheme. Further explanations and discussions for the SON VS-eICIC function is presented in Section 6.4.

According to the described SON architecture, sectorization change request is triggered based on the load situation at the cells served by the eNB. The triggering action initiates the data collection procedure where measurement reports are collected from the UEs residing in the underlying coverage area served by the same eNB. In order to perform event-triggered measurement reporting, the UEs needs to be configured with the required measurement reporting information after triggering, hence, UE configuration updates is broadcast over the serving coverage area using cell broadcast channel. The SON functions residing inside the eNB statistically analyze and make use of the collected measurement report data to extract relevant information like the nature of the spatial distribution of the UEs and to perform pre-evaluation of various performance metrics. While the final decision is made by the SON-logarithms at the eNB, the reconfiguration of the AAS parameter is carried out to activate/deactivate the beams of the desired sectorization type. The default or optimal configuration parameters utilized to reconfigure the AAS and also the various performance evaluations thresholds used

inside the SON functions are assumed to be provided by the OAM unit. Therefore, the exchange of these information are specified in the SON architecture configuration options information between the eNB and OAM. For further coordination of the sectorization changes and their impacts with other running network functions, the decisions of the SON algorithms are assumed to be communicated with the OAM unit via notification message information. The notification can be implemented either as a pre-notification where the eNB notifies a priori when the setorization change is planned after it is triggered or post-notification where the final sectorization decision is notified after the decision is through and the required action has been executed.

6.3   SON Function for Automated Sectorization

6.3.1   Introduction

The developed SON-AS function has four functional blocks. The first function block is called Monitoring where cell load condition and defined sectorization triggering criteria are periodically monitored and desired system parameters information are extracted. The next function block referred as Probing(Scanning) is responsible for triggering measurement reports and collection of the required information from the network. In the Probing(Scanning) stage the collected measurement report statistics are analyzed to extract essential input data to be used with the SON algorithm that automates the sectorization procedure. The SON algorithm performs further analysis on the input statistical data and evaluation of metric value to be used for final decision. The final SON function component described as Decision block compares the metric value evaluated in the Algorithm section against with a defined threshold level. The diagram of the SON-AS function comprising its four functional blocks is illustrated in Figure 6.2. Detail discussions about each functional blocks of the SON-AS function are provided in the subsequent sections.

6.3.2   Performance Monitoring

This section explains the monitoring procedures carried out by the SON function.

The sectorization process is designed to be performed on event-driven base. In this regard, both the activation and deactivation processes require associated triggering
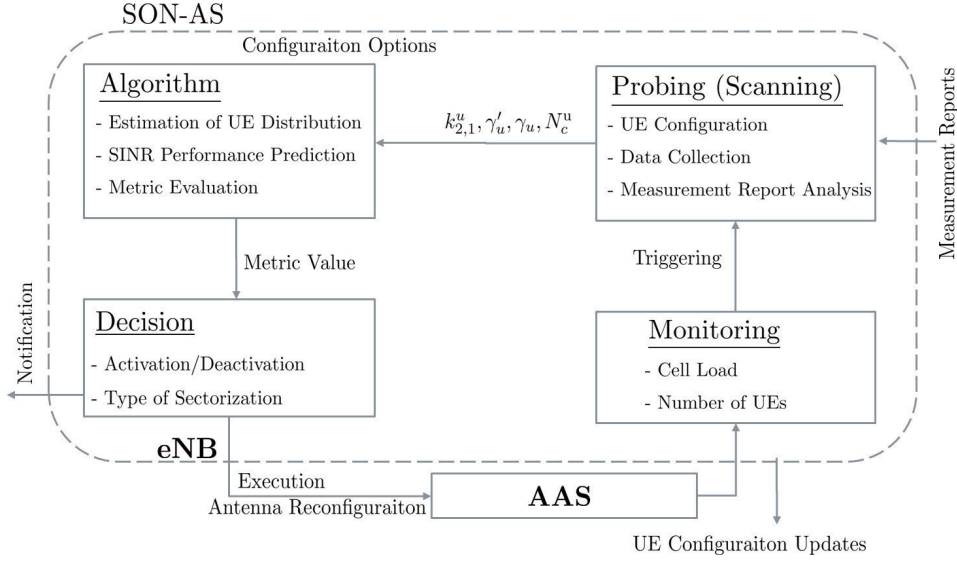
Figure 6.2. SON function for automated sectorization (SON-AS)

conditions when fulfilled the respective process is initialized. While the state of sectorization is OFF, the sector-antenna is serving the conventional cell coverage area using a single beam. The driving factor to trigger the addition of new cell that calls the activation process is attributed to the capacity demand stems from an overload situation at the conventional cell. For an accurate and timely reaction, the SON function needs to periodically monitor and track the average load level variation over time. Assuming the instantaneous load of cell c at scheduling time instant t is described by $\Lambda_c(t)$, the average cell load denoted by $\hat{\Lambda}_c(t)$ is computed using an exponential moving average to smooth out the short-term load fluctuation, i.e.

$$\hat{\Lambda}_c(t) = \begin{cases} \Lambda_c(t), & \text{if,} \quad t = 1, \\ \varepsilon \cdot \Lambda_c(t) + (1 - \varepsilon) \cdot \hat{\Lambda}_c(t - 1), & \text{otherwise,} \end{cases} \tag{6.1}$$

where $\varepsilon \in (0,1)$ is a smoothing factor used to weight the previous and current load information in order to get a smoother statistics of the load. For the triggering action, cell load threshold level Λ^{thr} is defined to indicate the occurrence of an overload situation. As a result, the conventional cell c is regarded as overloaded and the activation process is triggered when

$$\hat{\Lambda}_c(t) > \Lambda^{\text{thr}}. \tag{6.2}$$

For initialization of the deactivation process which merges the activated two cells to one, a rule is defined based on the presence or absence of UEs within the coverage of the two cells which are associated to the same-sector antenna. Hence, the deactivation process is triggered to revert to the conventional cell state if either of the cells are not

serving a single UE for a certain duration of time called here monitoring window time t_{mw}. Assuming, the number of UEs connected to cell c at time instant t is given by $N_c^{\mathrm{u}}(t)$, the deactivation process is triggered to reconfigure the sector-antenna a where $l_a = 1$ when

$$N_c^{\mathrm{mw}} = \sum_{\iota=0}^{t_{\mathrm{mw}}-1} N_c(t-\iota) \quad \text{for,} \quad (c \in \{c1, c2\} \subset \mathcal{C}) \wedge (A(c1) = A(c2) = a). \tag{6.3}$$

6.3.3   Measurement Data Collection and Analysis

This section discusses the approach used to collect data and its analysis after sectorization change process has been triggered.

After being triggered, the data collection process is carried out by employing a technique called cell Probing (Scanning). The Probing (Scanning) technique refers to the activation of a beam that can be used to scan over the coverage area of the conventional cell following a certain pattern in sectorization OFF state. In this regard, the configuration of the probing beam is assumed to be the same as one of the cell beams planned to be activated if the sectorization activation process is successful. The probing beam is designed only to broadcast cell-specific reference signal intended to be detected by UEs and trigger event based measurement reports, i.e. no data is transmitted over it. Figure 6.3 depicts the probing beam illustrating a certain scanning pattern. Accordingly, the UEs served by the conventional cell are configured using configuration update message to make measurement reports from the probing beam. From the UE perspective, the status of the probing beam will seen seen as a normal cell beam broadcasting a dedicate cell ID, hence, the normal RSRP measurement reporting procedure can be carried out.
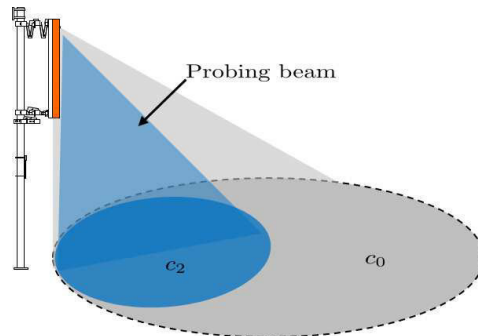
Figure 6.3. Probing(Scanning) mechanism

The analysis of the raw measurement report data is performed at the eNB. The first stage of the analysis is to determine the number of UEs that has been triggered by the probing cell beam and reported it as a potential handover target. This involves the computation of the link imbalance measurement criterion described by $k_{2,1}^u$ by Equation 4.7 and Equation 5.1 in the modeling section of Chapter 5 and 6, respectively. This eventually provides the estimate for the number of UEs that can be captured by each cell, N_c^{u}, if sectorization is executed.

The pre-evaluation of the UE SINR foreseeable after the sectorization change is carried out incorporating the computed $k_{2,1}^u$ and applying the developed SINR models which provide the relationship between γ_u and γ_u' as described by Equation 4.14 and Equation 5.4. All the analyzed data are provided to the SON algorithm where further analysis including rule based performance evaluation and decision metric value computation are executed.

6.3.4 SON Algorithm for Sectorization

In this section the developed SON algorithm employed to control the automation of the sectorization process is explained.

Once the sectorization process is triggered, the respective SON algorithm is started by initializing different timers associated to various activities during the algorithm run time. The SON algorithm is designed to run within a fixed time window described by t_{w} where t_{w} is defined as the time duration between the triggering and the final decision. This is illustrated with Figure 6.4 where the activation triggering process is exemplified using the average cell load variation. Once it is triggered the SON algorithm runs full cycle for t_{w} duration unless an interrupt criteria is fulfilled. For instance, the interrupt criteria defined for the activation process which is illustrated with the diagram in Figure 6.4 is the drop in the average cell load value below the overload Λ^{thr} level. This is specified by introducing a load hysteresis margin Λ^{hys} such that the running SON algorithm will be aborted if $\hat{\Lambda}_c(t) < \Lambda^{\mathrm{thr}} - \Lambda^{\mathrm{hys}}$.

The SON algorithm evaluates the system performance by considering the throughput statistics of all UEs from the coverage area served by the sector-antenna involved in the triggered sectorization process. This is carried out by a utility-based performance evaluation where an overall system utility associated to each sector-antenna is analyzed. The system utility of sector-antenna a denote by U_a is generally defined as the
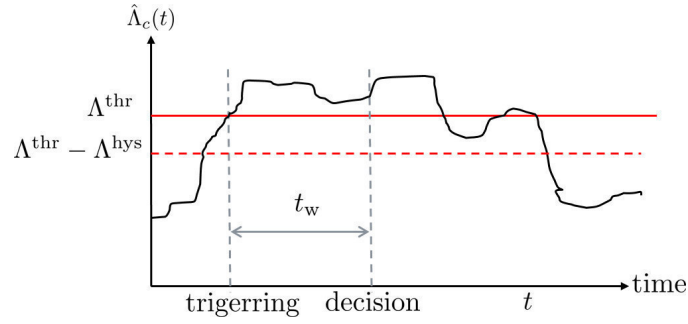
Figure 6.4. Example: sectorization activation process triggering

logarithmic sum of the throughput of the UEs connected to the cell(s) associated to a, i.e.

$$U_a = \sum_{\substack{\forall c \in \mathcal{C} \\ A(c)=a}} \sum_{\substack{\forall u \\ s(u)=c}} \log(\tau_u) \tag{6.4}$$

The decision metric to select the sectorizatin state that yields better system utility is derived by comparing the utility values evaluated for each sectorization state, i.e. for $l_a = 0$ and $l_a = 1$. Accordingly, the a decision metric, henceforth described by Δ_a, is defined as,

$$\Delta_a = U_{a|_{l_a=1}} - U_{a|_{l_a=0}} \tag{6.5}$$

$$= \sum_{u \in \mathcal{A}_a} \log\left(\frac{R'_u}{R_u} \cdot \frac{\mathcal{F}(\gamma'_u)}{\mathcal{F}(\gamma_u)}\right). \tag{6.6}$$

The expression obtained in Equation 6.5 portrays that the system utility difference described by Δ_a is determined by the achievable resource share gain, $\frac{R'_u}{R_u}$, and the ratio of the spectral efficiency performance of the UEs with respect to each state, $\frac{\mathcal{F}(\gamma'_u)}{\mathcal{F}(\gamma_u)}$. Replacing the the resource share gain as a function of the UE redistribution metric λ_a and the ratio of the spectral efficiency performance by the sensitivity level metric defined by Equation 4.24, Equation 6.5 can be re-expressed as

$$\Delta_a = \sum_{u \in \mathcal{A}_{c1}} \log\left((1+\lambda_a) \cdot \frac{1}{\Gamma^a_u}\right) + \sum_{u \in \mathcal{A}_{c2}} \log\left(\left(\frac{1+\lambda_a}{\lambda_a}\right) \cdot \frac{1}{\Gamma^a_u}\right), \quad \text{for} \ \ \lambda_a \neq 0 \tag{6.7}$$

$$\text{where,} \ \ \mathcal{A}_a = \mathcal{A}_{c1} \bigcup \mathcal{A}_{c2}, \tag{6.8}$$

and the coverage of the cells $\mathcal{A}_{c1}$ and $\mathcal{A}_{c2}$ are determined in the probing stage of the SON-AS function. Equation 6.7 can be rewritten as the sum of the logarithm of the resource gains and a term describing the overall change of the SINR of the UEs at each

cell using their sensitivity values, i.e.,

$$\Delta_a = \log \left(\frac{(1 + \lambda_a)^{N^{\mathrm{u}}_{c1} + N^{\mathrm{u}}_{c2}}}{\lambda_a^{N^{\mathrm{u}}_{c2}}} \right) - \left(\sum_{u \in \mathcal{A}_{c1}} \log(\Gamma^a_u) + \sum_{u \in \mathcal{A}_{c2}} \log(\Gamma^a_u) \right). \qquad (6.9)$$

Given $\hat{\Gamma}_{c1}$ and $\hat{\Gamma}_{c2}$ are geometric means of the sensitivity values of the UEs within each cell, i.e.,

$$\hat{\Gamma}_{c1} = \left[\prod_{u \in \mathcal{A}_{c1}} \Gamma^a_u \right]^{\frac{1}{N^{\mathrm{u}}_{c1}}}, \quad \text{and} \quad \hat{\Gamma}_{c2} = \left[\prod_{u \in \mathcal{A}_{c2}} \Gamma^a_u \right]^{\frac{1}{N^{\mathrm{u}}_{c2}}}, \qquad (6.10)$$

Δ_a can be re-described in terms of the average sensitivity values,

$$\Delta_a = \Delta_\lambda - \Delta_\Gamma, \qquad (6.11)$$

$$\text{where,} \quad \Delta_\lambda = \log \left(\frac{(1 + \lambda_a)^{N^{\mathrm{u}}_{c1} + N^{\mathrm{u}}_{c2}}}{\lambda_a^{N^{\mathrm{u}}_{c2}}} \right), \quad \text{and} \qquad (6.12)$$

$$\Delta_\Gamma = \left(N^{\mathrm{u}}_{c1} \cdot \log(\hat{\Gamma}_{c1}) + N^{\mathrm{u}}_{c2} \cdot \log(\hat{\Gamma}_{c2}) \right). \qquad (6.13)$$

From Equation 6.11, Δ_a metric is used to indicate which sectorization state is outperforming in maximizing the defined system utility, accordingly, sectorization ON is selected if $\Delta_a > 0$ else sectorization OFF state is preferred. As clearly illustrated, the value of Δ_a depends on the balance between the overall system gain from radio resource share and the degradation experienced in the system SINR, i.e. $\Delta_a > 0$ if $\Delta_\lambda > \Delta_\Gamma$. Consequently, the region in the performance curve where $\Delta_a > 0$ and the decision boundary for the SON algorithm varies following λ_a and Γ^a_u values within each cell. For the purpose of illustration, the curve showing the Δ_Γ plotted for a range of average sensitivity values within $c1$ and $c2$ when the UE distribution yields different λ_a cases are presented in Figure 6.5 assuming typical VS scenario. The figure demonstrates the SON decision curve where $\Delta_a > 0$ is defined based on Δ_λ which is evaluated at the given λ_a using Equation 6.11. As depicted in Figure 6.5 (a), Δ_λ value keeps increasing as λ_a increases because it starts to balance the resource gain within each cell served by the sector-antenna a. It is interesting to see that the value of Δ_λ attains its maximum when the load distribution between the two cells becomes balanced, $\lambda_a = 1$, in this case, the achieved resource gain on the overall aggregate coverage area is fairly maximized.

For low λ_a value, $\lambda_a = 0.1$, the achievable resource gain at the outer cell is minimal resulting in a very small Δ_λ, this puts limitation on the margin of the sensitivity level that leads to $\Delta_a > 0$, see the light color region in Figure 6.5. Accordingly, an average sensitivity of around $\hat{\Gamma}_{c1} \approx 1.5$ is seen to be the limit at the outer cell such that if there

are many UEs suffering from the inter-cell interference being in the sensitive region, i.e. $\hat{\Gamma}_{c1} > 1.5$, the system utility becomes deteriorated resulting in a negative metric value, $\Delta_a < 0$, which is indicated by red color in the figure. As demonstrated with the plots in Figure 6.5 (b-f), the sensitivity boundary at the outer cell exhibits improvement as λ_a increases and the corresponding sensitivity range that corresponds to $\Delta_a > 0$ is in balance at both cells when $\lambda_a = 1$. This clearly demonstrates that the decision metric of the SON inspects not only the number connected UEs within each cell but also the impact of their spatial concentration by using the average sensitivity level metric value.
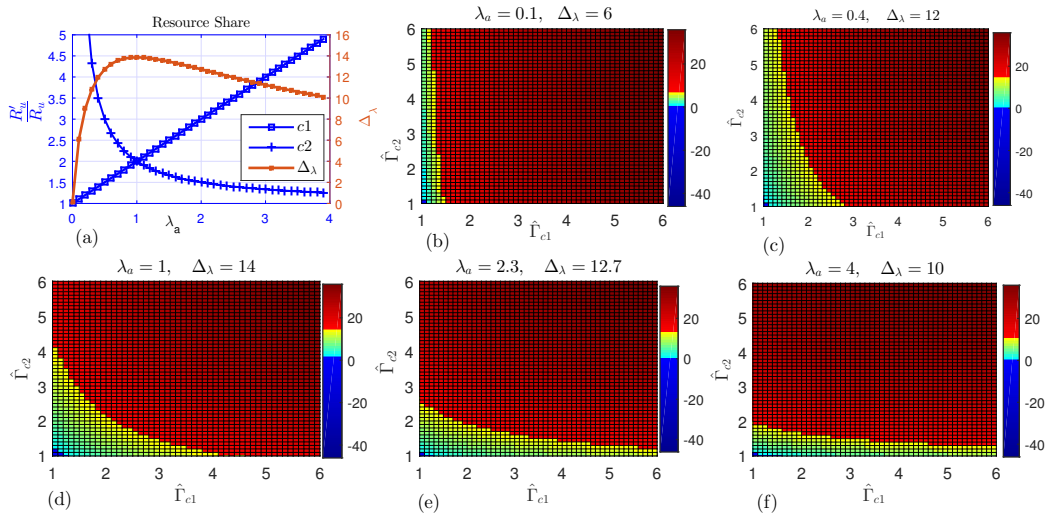
Figure 6.5. SON algorithm decision for VS: UE distribution and sensitivity

Moreover, the trends observed in Figure 6.5 indicates that depending on the average sensitivity performance of each cell, there exists a limited range of λ_a that maximizes the utility. In order to determine the λ_a range a necessary but not sufficient condition for sectorization activation decision is defined. From Equation 6.4, fairly maximizing the overall utility, U_a, is the same as maximizing the utilities of each cell denoted by U_{c1} and U_{c2}, see their coverage relationship by Equation 6.8. The same way described by Equation 6.7, the utility performance difference corresponding to each cell is defined as Δ_{c1} and Δ_{c2}. Given δ_{c1} and δ_{c2} are the allowable margin of the utility degradation at each cell, the necessary conditions needs to be fulfilled when Δ_a is evaluated are

$$\Delta_{c1} \geq \delta_{c1}, \quad \text{and} \quad \Delta_{c2} \geq \delta_{c2} \tag{6.14}$$

With further manipulation of the respective cell utilities, the range of λ_a that satisfies

the necessary condition specified by Equation 6.14 is derived as

$$e^{\frac{\delta_{c1}}{N_{c1}^{u}}} \cdot \hat{\Gamma}_{c1} - 1 \;\; \leq \;\; \lambda_a \;\; \leq \;\; \frac{1}{e^{\frac{\delta_{c2}}{N_{c2}^{u}}} \cdot \hat{\Gamma}_{c2} - 1}. \tag{6.15}$$

During every iteration, the SON algorithm evaluates the necessary condition described by Equation 6.15 by computing λ_a.

The SON algorithm used to automate the AAS-driven sectorizaion process is presented in Algorithm 2. In the algorithm, different timers and counters are defined to control the operation while the full algorithm is run within the time window t_{w}. When activation process is triggered, activation timer t_{act} is initialized. In each iteration, two counters $t_{\mathrm{act}}^{(+)}$ and $t_{\mathrm{act}}^{(-)}$ are used which are incremented when activation conditions are fulfilled or failed, respectively. Likewise, deactivation timer t_{deact} and the counters $t_{\mathrm{deact}}^{(+)}$ and $t_{\mathrm{deact}}^{(-)}$ are used for the deactivation process. After the algorithm iteration cycle is completed, the number of successful and fail conditions are compared by analyzing the counter values by applying thresholds $t_{\mathrm{act}}^{\mathrm{thr}}$ and $t_{\mathrm{deact}}^{\mathrm{thr}}$ which provides hysteresis margin for the decision boundary. Accordingly, if the count of success is higher than the fails, a decision flag will be set for the respective process, i.e. $flag_{\mathrm{act}}$ or $flag_{\mathrm{deact}}$, which is passed to the final decision block of the SON-AS function together with average metric value $\hat{\Delta}_a$, see Algorithm 2 for details.

6.3.5 Decision

This section describes the final decision block of the SON-AS function.

By examining the status of the decision flag provided by Algorithm 2, the final sectorization decision is made according to the value of the decision metric compared against with threshold $\delta_a > 0$. δ_a is introduced to avoid unnecessary frequent activation/deactivation decision due to a marginal change on the decision metric value. The decision procedure is described in Algorithm 3.

In practice, the type of sectorization to be executed, HS or VS, is determined by two factors. The first one is the capability of the employed AAS to support HS, i.e. whether the antenna array is a single column or multi-column array. If the AAS is composed of a single column array, the viable option for the sectorization is only VS. On the other hand, if it is a multi-column array, for instance two column array as discussed in the system model, both HS and VS are supported. In this regard, either HS or VS can be executed depending on how the UEs are spatially distributed over the underlying coverage area which can be captured by analyzing the data collected during

---

Algorithm 2 : SON Algorithm for Automated Sectorization

  1: **<u>ACTIVATION PROCESS</u>**
  2: **if** $l_a = 0$ **then**
  3:      **if** $\hat{\Lambda}_c(t) > \Lambda^{\text{thr}}$ **then**
  4:          $t_{\text{act}} \leftarrow 1$:ACTIVATION TRIGGERED
  5:          $t_{\text{act}}^{(+)} \leftarrow 1, \quad t_{\text{act}}^{(-)} \leftarrow 0$
  6:          **while** $t_{\text{act}} \neq 0$ **And** $t_{\text{act}} \leq t_{\text{w}}$ **do**
  7:              **if** $\hat{\Lambda}_c(t) \geq \Lambda^{\text{thr}} - \Lambda^{\text{hys}}$ **then**
  8:                  **if** $e^{\frac{\delta_{c1}}{N_{c1}^{\text{u}}}} \cdot \hat{\Gamma}_{c1} - 1 \ \leq \ \lambda_a \ \leq \ \dfrac{1}{e^{\frac{\delta_{c2}}{N_{c2}^{\text{u}}}} \cdot \hat{\Gamma}_{c2} - 1}$ **then**
  9:                      $t_{\text{act}}^{(+)} \leftarrow t_{\text{act}}^{(+)} + 1$
 10:                  **else**
 11:                      $t_{\text{act}}^{(-)} \leftarrow t_{\text{act}}^{(-)} + 1$
 12:                  **end if**
 13:                  $t_{\text{act}} \leftarrow t_{\text{act}} + 1$
 14:              **else**
 15:                  $t_{\text{act}} \leftarrow 0$:ACTIVATION ABORTED
 16:                  $t_{\text{act}}^{(+)} \leftarrow 0, \quad t_{\text{act}}^{(-)} \leftarrow 0$
 17:              **end if**
 18:          **end while**
 19:      **end if**
 20: **end if**

---

each probing pattern. Having decided the type of sectorizatin, the AAS is reconfigured with the right parameter from the configuration options provided in order to execute the cell beams with the desired radiation pattern.

6.4 SON Function for Adaptive Inter-Cell Interference Coordination

6.4.1 Introduction

The performance and reliability of the inter-cell interference coordination technique developed for VS highly depends on the blanking pattern configuration. Since the spatial distribution of the users is dynamically varying, the blanking pattern needs to be flexibly configured with the a value that yields maximized overall system performance, hence, the blanking pattern optimization is a crucial step in applying the VS-eICIC. The analytical approach for the blanking pattern configuration optimization and the respective performance analysis have been presented in Chapter 5. Automatically adapting the configuration requires to timely follow the change in the system load

21: **DEACTIVATION PROCESS**
22: **if** $l_a = 1$ **then**
23:      **if** $N_{c1}^{\mathrm{mw}} = 0$ **Or** $N_{c2}^{\mathrm{mw}} = 0$ **then**
24:         $t_{\mathrm{deact}} \leftarrow 1$:DEACTIVATION TRIGGERED
25:         $t_{\mathrm{deact}}^{(+)} \leftarrow 1, \quad t_{\mathrm{deact}}^{(-)} \leftarrow 0$
26:         **while** $t_{\mathrm{deact}} \neq 0$ & $t_{\mathrm{deact}} \leq t_{\mathrm{w}}$ **do**
27:             **if** $e^{\frac{\delta_{c1}}{N_{c1}^{\mathrm{u}}}} \cdot \hat{\Gamma}_{c1} - 1 \;\leq\; \lambda_a \;\leq\; \dfrac{1}{e^{\frac{\delta_{c2}}{N_{c2}^{\mathrm{u}}} \cdot \hat{\Gamma}_{c2} - 1}}$ **then**
28:                 $t_{\mathrm{deact}}^{(-)} \leftarrow t_{\mathrm{deact}}^{(-)} + 1$
29:             **else**
30:                 $t_{\mathrm{deact}}^{(+)} \leftarrow t_{\mathrm{deact}}^{(+)} + 1$
31:             **end if**
32:             $t_{\mathrm{deact}} \leftarrow t_{\mathrm{deact}} + 1$
33:         **end while**
34:      **end if**
35: **end if**
36: **DECISION METRIC EVALUATION**
37: **if** $(t_{\mathrm{act}} \neq 0$ **And** $t_{\mathrm{act}} = t_{\mathrm{w}})$ **Or** $(t_{\mathrm{deact}} \neq 0$ **And** $t_{\mathrm{deact}} = t_{\mathrm{w}})$ **then**
38:      **if** $l_a = 0$ **And** $t_{\mathrm{act}}^{(+)} > t_{\mathrm{act}}^{(-)} - t_{\mathrm{act}}^{\mathrm{thr}}$ **then**
39:        $flag_{\mathrm{act}} \leftarrow 1$
40:      **end if**
41:      **if** $l_a = 1$ **And** $t_{\mathrm{deact}}^{(+)} > t_{\mathrm{deact}}^{(-)} - t_{\mathrm{deact}}^{\mathrm{thr}}$ **then**
42:        $flag_{\mathrm{deact}} \leftarrow 1$
43:      **end if**
44:      $\hat{\Delta}_a \leftarrow \frac{1}{t_{\mathrm{w}}} \cdot \sum\limits_{\iota=0}^{t_{\mathrm{w}}-1} \Delta_a(t - \iota)$
45: **end if**

Algorithm 3 DECISION: Sectorization-ACTIVATION/DEACTIVATION

1: **if** $flag_{\mathrm{act}} = 1$ **And** $\hat{\Delta}_a \geq \delta_a$ **then**
2:      $l_a = 1$: **ACTIVATE**
3:      $flag_{\mathbf{act}} \leftarrow 0$
4: **end if**
5: **if** $flag_{\mathbf{deact}} = 1$ **And** $\hat{\Delta}_a < \delta_a$ **then**
6:      $l_a = 0$: **DEACTIVATE**
7:      $flag_{\mathbf{deact}} \leftarrow 0$
8: **end if**

---

and the sensitivity of the UEs to the inter-cell interference level based on their spatial location. Hence, a SON based mechanism that adaptively optimize the blanking pattern configuration is designed and presented.

The SON function that controls the adaptive VS-eICIC is described by Figure 6.6. Accordingly, when VS is activated, the blanking pattern can be configured to a default initial value β_{int}. Two functional blocks are defined for the SON VS-eICIC operation.

The first block is an initialization step where performance analysis and algorithm entering conditions evaluations are carried out. The second functional block embeds the SON algorithm that iteratively updates the blanking pattern. Detail explanations of the functional blocks is provided in subsequent sections. In Section 6.4.2, the initialization step is discussed and the SON algorithm is presented in Section 6.4.3
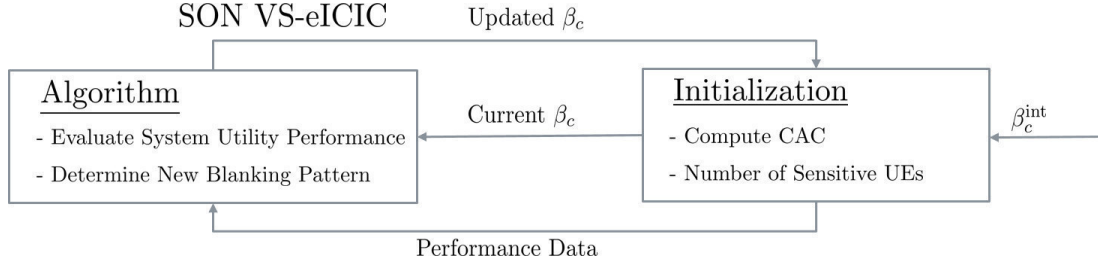
Figure 6.6. SON function for adaptive VS-eICIC (SON VS-eICIC)

6.4.2 Initialization and Resource Status Reporting

This section describes the first functional block of the SON function for VS-eICIC.

The interference-coordination can be carried out effectively while maintaining enhanced system performance if two conditions are satisfied. The first one is the interference aggressor cell which mutes its transmission, in this case the inner cell, should have available extra capacity to allow the blanking. The second condition refers to whether there are UEs or not at the outer cell which are impacted by the interference coming from the inner cell such that their transmission needs to be coordinated during the transmission muting duration.

The available capacity at the inner cell is computed the same way as described in the system model Section 2.6. However, considering the transmission blanking, the effective fraction of resource available at the inner cell for transmission is $1 - \beta_{c2}$. Therefore, the available capacity at the inner cell can be re-described incorporating blanking pattern β_{c2} as

$$AC_{c2} = \max\{0, \Lambda_{c2}^{\text{peak}} - \beta_{c2} - (1 - \beta_c) \cdot \Lambda_{c2}\} \leq 1. \qquad (6.16)$$

Therefore, the inner cell is regarded as able to blank if it has a non-zero AC_{c2} value, i.e. $AC_{c2} > 0$.

The number of sensitive UEs, $N_{c1}^{\text{u(S)}}$, at the outer cell is computed utilizing a sensitivity level threshold used for grouping as described in Equation 4.25. As explained in Section

4.4.4, the sensitivity threshold, Γ^{Thr}, is determined iteratively based on the inner cell utility performance evaluated for the configured blanking pattern, i.e.,

$$N_{c1}^{\text{u(S)}} = \sum_{\forall u \in \mathcal{A}_{c1}} \mathbf{1}\{\Gamma_u^a \geq \Gamma^{\text{Thr}}\}. \tag{6.17}$$

At initial phase of the algorithm $\beta_{c2} = \beta_{\text{int}}$. Having $AC_{c2} > 0$ and $N_{c1}^{\text{u(S)}} > 0$ are the entering conditions for the SON algorithm.

6.4.3   SON Algorithm for Blanking Pattern Adaptation

This sections explains the SON algorithm that automatically adapts the blanking pattern.

The iterative blanking pattern adaptation procedure analyzes the statistics of the UE throughput performance data collected each scheduling time step. The system utility U_a computed over the aggregate cell coverage area $\mathcal{A}_a$, i.e. inner plus outer, as expressed in Section 4.4.4 is employed for performance based adaptation. The average of the UE throughput performance data within a sliding time window t_{ABS} are used in the system utility computation to provide a reliable comparison between utility performances where variables used for utility computation are indicated in Equation 4.37. Furthermore, a blanking pattern adaptation step size β^{step} is defined to be used to adjust the current blanking pattern in a desired direction, i.e. increase (β^{++}) or decrease (β^{--}). In the SON algorithm, the primary conditions to determine the blanking pattern update direction, β^{++} or β^{--}, are the values of AC_{c2} and $N_{c1}^{\text{u(S)}}$. In this regard, unless both conditions $AC_{c2} > 0$ and $N_{c1}^{\text{u(S)}} > 0$ are fulfilled, the blanking pattern is always decremented if the respective utility performance evaluation is successful and this can be summarized in pseudo-code 4

Pseudo-code 4 : Blanking pattern update direction

---
   if $AC_{c2} > 0$ **And** $N_{c1}^{\text{u(S)}} > 0$ **then**
      β^{++} **Or** β^{--}
   else
      β^{--}
   end if

Every iteration step, the adaptation strategy involves the computation of the system utility from the UE throughput performance data collected within the t_{ABS} window applying three different blanking pattern settings using Equation 4.37: the current

(β_c), incremented $\beta_c^+ = \beta_c + \beta^{\text{step}}$ and decremented $\beta_c^- = \beta_c - \beta^{\text{step}}$ blanking pattern values and the corresponding utility values are denoted by U_a, U_+^a and U_a^-, respectively. During the updating step, the decision whether to increase/decrease β_c is performed by comparing the values of U_a^+ and U_a^- with respect to the actual utility performance, i.e. U_a. The overall adaptive mechanism and algorithm decisions are more elaborated and presented using the flow chart depicted in Figure 6.7.
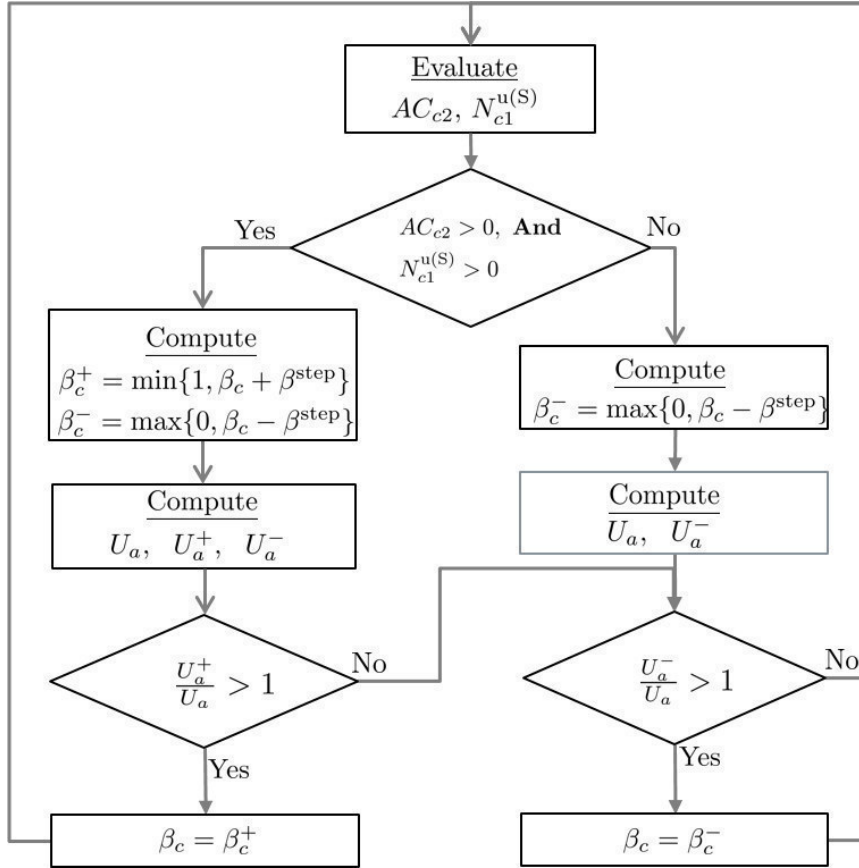
Figure 6.7. SON algorithm flowchart for adaptive VS-eICIC

6.5 Performance Evaluation and Analysis

6.5.1 Performance Evaluation of SON for Automated Sectorization

The performance evaluation of the SON mechanism developed to automate the AAS-based sectorization is presented in this Section. The investigation and evaluations

have been carried out with system level simulations conducted using the 3GPP and RT-Scenarios considering a non-homogeneous spatio-temporarily varying UE traffic distributions.

In the investigation, the initial state of the sectorization is set to the default Conventional sectorization and the SON for AS is let to run network-wide at all BS sites. Each eNB autonomously monitors the load situation over the coverage area served by the respective-sector antenna. In this particular exemplary scenario, the automated vertical sectorization is illustrated where it is prioritized over HS and assumed to be generally preferred as it can be enabled for both single/multi-column array AAS for the aforementioned reason. In the simulation, the non-homogeneous UE distribution variation involving traffic hotspots changing their spatial location periodically over time. The resulting sectorization status (ON/OFF) for the complete simulation time period is shown in Figure 6.8. As exhibited in Figure 6.8 the sectorization state at various sites served by each sector-antenna a is changing overtime and, for this particular scenario, the sectorization has been activated over the entire network for 24% of the network operation time, that means, the the SON based automation mechanism is able to avoid unnecessary sectorization activation over 76% of the time thereby proportionally reducing consumption of network resources, like base band resources and energy consumption, compared to the always ON sectorizaion case to which a fixed and dedicated resources are always allocated.
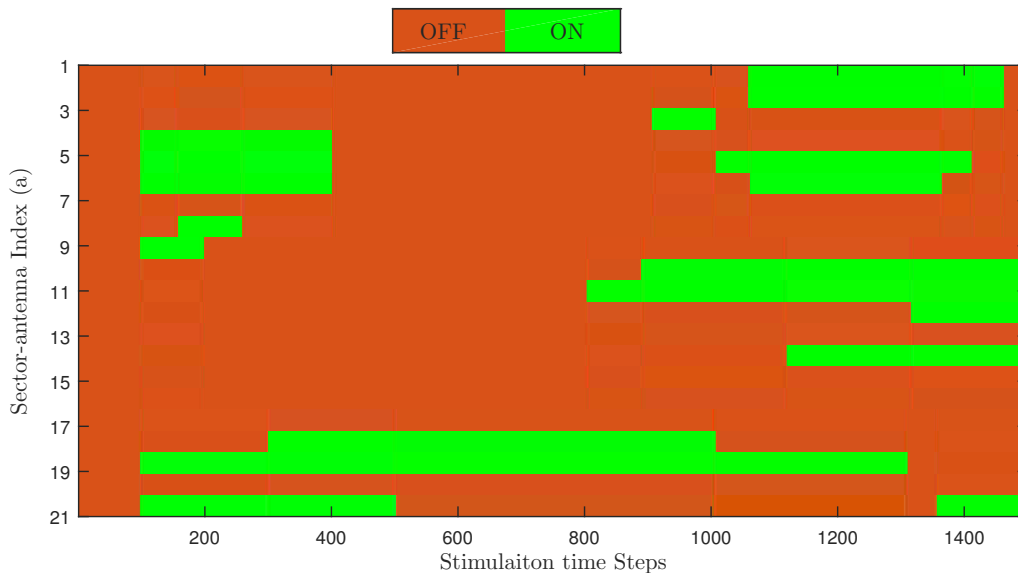
Figure 6.8. 3GPP-scenario: Sectorization state over time

The performance of the SON-enabled sectorization is further explored by analyzing UE

throughput statistics collected from the coverage area $\mathcal{A}_a$ served by different sector-antennas. The throughput performance of the UEs within coverage $\mathcal{A}_a$ for different cases such as conventional sectorization (VS=OFF), always VS=ON with out SON and VS with SON are plotted in Figure 6.9. For exemplification, results from three selected coverage areas served by sector-antenna $a = 5$, $a = 9$ and $a = 15$ where the UE throughput statistics are collected and evaluated overtime considering a sliding evaluation time window $t_{\text{ev}} = 100$ simulation time steps while tracking the traffic variation. The evaluation scheme is carried out by comparing the values of $\text{TP}^{5\%}_{\mathcal{A}_a}$, $\text{TP}^{50\%}_{\mathcal{A}_a}$ and $\text{TP}^{\text{avg}}_{\mathcal{A}_a}$ computed from the collected statistical data. As indicated in Figure 6.8 for $a = 5$, the applied SON mechanism has activated VS at different times. In comparison, the value of $\text{TP}^{5\%}_{\mathcal{A}_a}$ achieved with SON-AS is outperforming the always VS=ON case by 35% maintaining the same performance with VS=OFF during the second time when VS has been activated. Moreover, it can be clearly seen that the automated VS mechanism yields performance enhancement similar to the always VS=ON case by activating the sectorization only when it is worthwhile thereby providing throughput gain of over 80% at the 50% CDF level of the statistics.
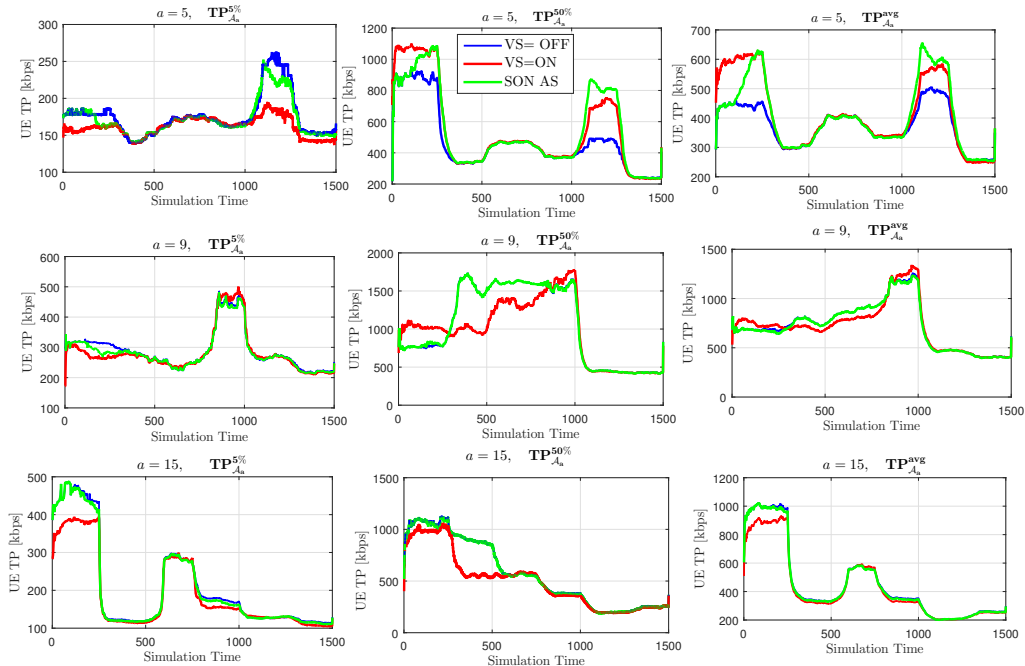
Figure 6.9. SON AS performance comparison for 3GPP-scenario

The adverse impact of always VS=ON case and the need for SON is demonstrated in Figure 6.9 for $a = 9$ where deactivating the sectorization averts the significant performance degradation that could arise from the activated cells. This is evident in the performance plot that the 50% CDF level throughput performance is enhanced

achieving a gain of more than 60% by employing the automation mechanism.

On the other hand, Figure 6.8 shows that for $a = 15$ the SON strictly decides turning off the VS at all times as favorable conditions have not been met. This is manifested in Figure 6.9 where the automated VS performance has been following the VS=OFF both at the 5% and 50% CDF level which are indicated by $TP_{\mathcal{A}_a}^{5\%}$ and $TP_{\mathcal{A}_a}^{50\%}$ values, respectively. In this case, the automated VS is able to provide a gain of up to 37% and 57% over the always VS=ON approach at the 5% and 50% CDF level respectively. This clearly demonstrates that the static always VS=ON approach is detrimental and could lead to significant performance degradation in situations like $a = 15$ if it is kept active all the time. It is worth noting that the always VS=ON is unwanted and costly over-provisioning solution as it keeps the VS always activated irrespective of the load situation. The presented results show that the applied sectorization automation mechanism provides a substantial system performance gain by averting the critical performance deterioration situations that can be caused by keeping the activated cells all the time ensuring the sectorization state that outperforms is maintained.
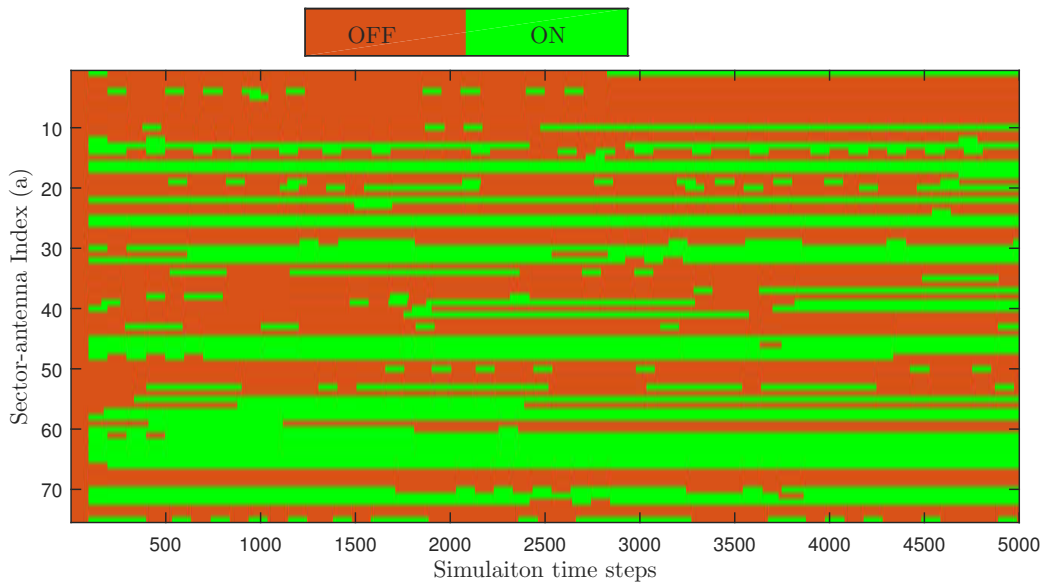
Figure 6.10. RT-scenario: Sectorization state over time

The sectorization study has been carried out further by employing the developed SON based automation scheme in a more realistic RT-scenario wherein the UEs are spatially distributed in a diversified manner to reflect various practical situations. In this scenario, both indoor and outdoor propagation environments are assumed. Cluster of UEs which are moving on streets with a constant speed of 3 km/h creating a moving traffic hotspots are considered to simulate dynamically varying load situation within

the entire network. Accordingly, it can be seen in Figure 6.10 that the sectorization state is dynamically changing over time tracking the traffic load variation. Compared to the 3GPP-scenario discussed above, the ON/OFF operations in this particular scenario are significantly noticeable where the ON states are accounting for 40% of the total simulation time over the entire network while 60% of the time the sectorization is deactivated.

Similarly, the performance of the automated sectorization is examined by analyzing the UE throughput statistics while the UEs are being served by a specific sector-antenna irrespective of the sectorization state. For the purpose of illustration, the throughput statistics collected from two coverage areas served by sector-antenna $a = 53$ and $a = 60$ are presented in Figure 6.11 where in each sub-figure three CDF plots are depicted comparing the three different sectorization cases discussed earlier. For each coverage area served by a particular sector-antenna, the throughput statistics within a certain evaluation time window of $t_{\text{ev}} = 250$ are compared and three different time widows are selected for exemplification to assess the performance while the sectorization state is being varied over time.
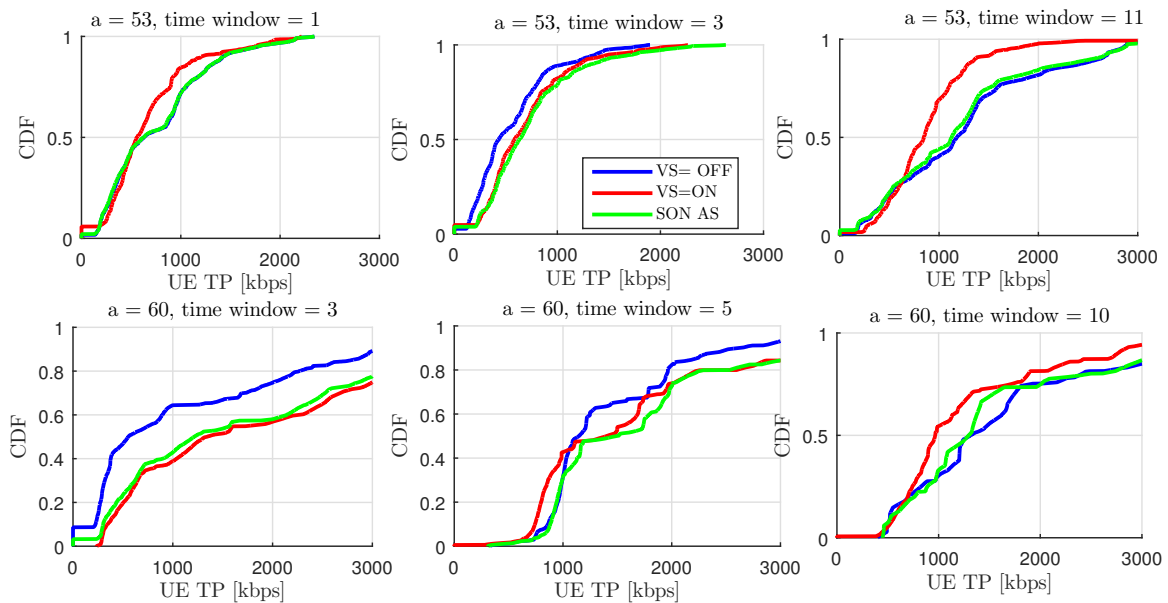
Figure 6.11. SON AS performance comparison for RT-scenario

In Figure 6.11, for $a = 53$ time window 1 refers to the initial phase of the simulation and apparently the sectorization state if OFF at this stage. In this situations we can still see the that the throughput CDF corresponding to the SON AS is aligned with

the VS=OFF and no significant performance difference is observed. While the simulation time increases, the sectorization state is changed to ON in the third evaluation time window as exhibited in Figure 6.10 triggered by higher load situation. As can be observed from the corresponding performance comparison figure, the automated VS performance is aligned with the always VS=ON case as the sectorization stayed activated for the whole evaluation time windows and yielding above 51% gain in the system throughput at the 50% and 80% CDF levels compared to the VS=OFF case. However, the sectorization state have stayed on ON state only until the beginning of the 11$^{\text{th}}$ evaluation time windows, i.e. $t = 2600$ simulation time, within this time window the VS has been deactivated going back to VS=OFF state. The corresponding performance plots are evident that the VS=OFF state outperforms the always VS=ON case for higher CDF percentiles providing more than 35% gain in the average UE throughput, i.e. $\text{TP}_{\mathcal{A}_a}^{\text{avg}}$. The same performance trend has been demonstrated for $a = 60$ over different evaluation time windows. It is worth noting the performance over time window 5 that the CDF of the automated VS throughput performance is aligned with both the VS=OFF case at the lower percentile and the always VS=ON at the higher percentiles thereby maintaining always the better performance distribution. This is a clear manifestation of the benefits of the developed SON based automation mechanism in ensuring maximized achievable system performance via tracking the traffic load variation.

The presented performance comparisons and detail analysis have demonstrated that, indeed, the sectorization process needs to be automated in order to deliver enhanced system performance based on the actual traffic mix and distribution. As reported using the displayed exemplary results, the sectorization needs to be activated when and where there is a demand for the capacity and only when it can bring benefit.

6.5.2   Performance Evaluation of SON for Adaptive Inter-Cell Interference Coordination

The performance of the developed adaptive VS-eICIC technique that automatically optimizes blanking pattern configuration is discussed in this Section.

For this particular investigation, the heterogeneous hotspot-based traffic distribution model used in the SON-AS study is considered over the entire network coverage are and the spatial locations of the UEs are assumed to remain invariant with time. In order to avoid any conflict that might occur between the SON-functions of AS and VS-eICIC, as SON-function coordination is out of the scope of this thesis, only the SON

for VS-eICIC is let to run while SON-AS is turned off. In this regard, it is valid to maintain the same sectorization state, for instance VS=ON in this case, for the whole simulation time as long as the spatial distribution of the UEs remains stationary.

Assuming VS=ON state at all sites, the network wide blanking pattern is initially configured to a default value $\beta_{\text{int}} = 0.2$. Then, the SON VS-eICIC is enabled to operate autonomously at each eNB as explained in Section 6.4 for several simulation time steps. Each simulation time step, β_c can be updated, increased/decreased, based on conditions by applying a constant step size $\beta^{\text{step}} = 0.05$. Figure 6.12 shows how the the network wide β_c behave for different blanking pattern adaptation period, t_{ABS}, where one period corresponds to $90s$ in the simulation. Despite identical initial configuration, β_c is converged to different values overtime at the inner cells associated to various sector-antenna where the final converged values are presented in Figure 6.12 (b).
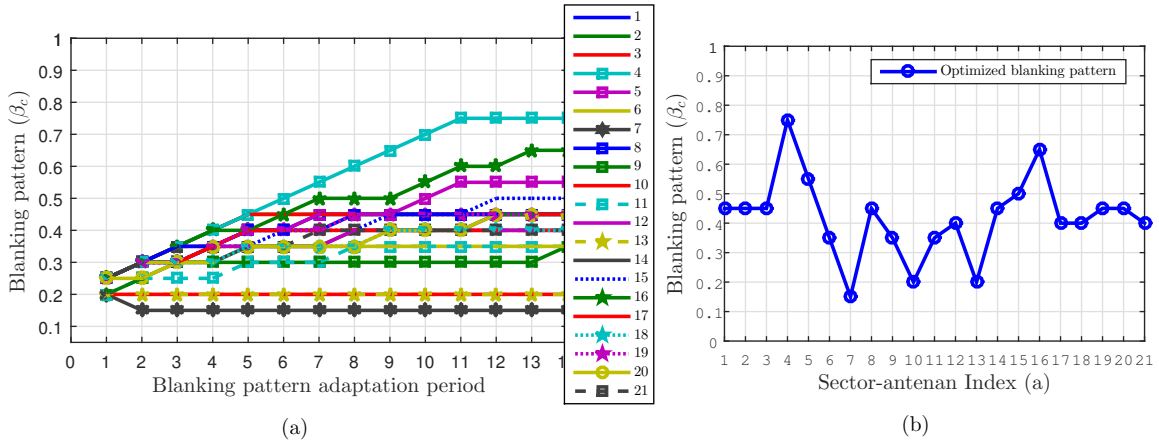
Figure 6.12. SON based automated blanking pattern adaptation for VS-eICIC

For example, the inner cell at $a = 4$ is converged to 0.75 indicating the presence of high number UEs within the corresponding outer cell which are highly impacted by the interference coming from the inner cell and the capability of the inner cell to mute its transmission while maximizing the system utility performance. On the other hand, the value of β_c is converged to a minimum value of 0.15 at $a = 7$ depicting the nonavailability of extra capacity the inner cell can offer by blanking. Moreover, it can be observed that in some cells where the spatial distribution of the UEs behave more or less uniform, the blanking pattern is moderate and converged fast to around 0.35. These observations are in agreement with the results of the analytical optimization approach presented in the modeling section, Section 4.4.4.

The performance of the developed adaptive VS-eICIC is further studied by statistical analysis of the UE throughput data collected from the respective coverage area $\mathcal{A}_a$.

The results are summarized for the entire network and presented in Figure 6.13 where the values of $\text{TP}_{\mathcal{A}_a}^{5\%}$, $\text{TP}_{\mathcal{A}_a}^{50\%}$, $\text{TP}_{\mathcal{A}_a}^{80\%}$ and $\text{TP}_{\mathcal{A}_a}^{\text{avg}}$ are shown for two simulation cases: in the first case VS-eICIC is disabled, i.e. $\beta_c = 0$, and in the second simulation case, the SON enabled VS-eICIC is employed. The gain values indicated in the figure are evaluated with respect to the corresponding performance while VS is deactivated, i.e. VS=OFF.
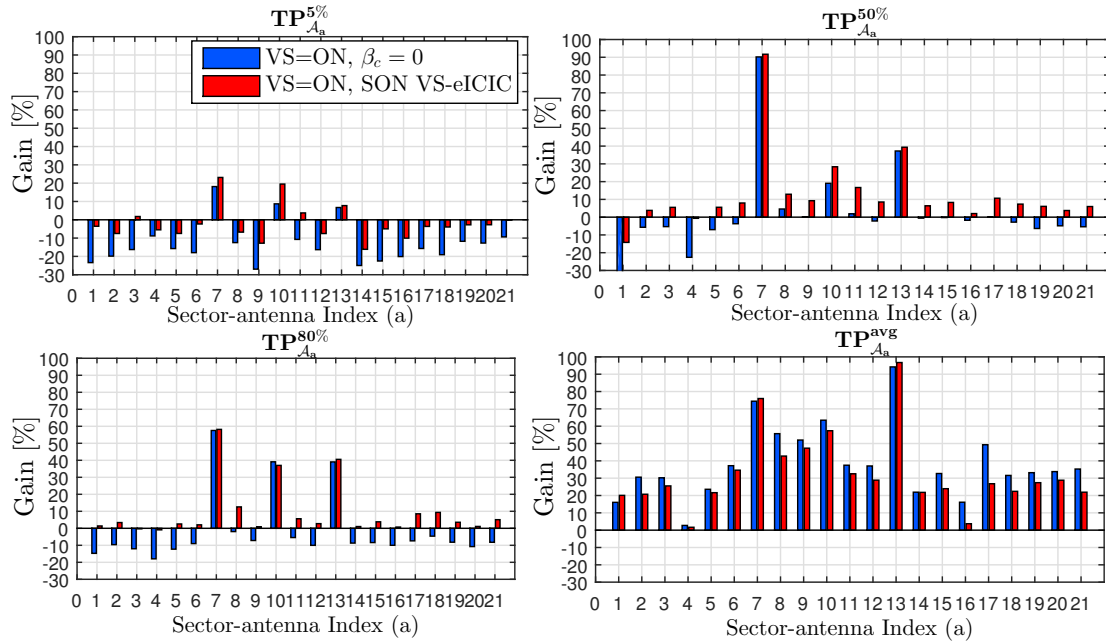
Figure 6.13. Performance of SON enabled adaptive VS-eICIC

The main objective of the proposed VS-eICIC scheme is to combat the impact of the inter-cell interference that results from the sectorization at a cost of muting data transmission in interferer cell while selectively maximizing the performance of the UEs critically affected by the interference problem on the interfered cell. This is demonstrated in Figure 6.13 where the extreme performance degradation with VS=ON at the 5%, 50% and 80% throughput CDF level are significantly mitigated by applying VS-eICIC technique. Specifically, when the VS-eICIC is employed, up to 23% additional performance gain is achieved at the 5% throughput CDF levels, see $\text{TP}_{\mathcal{A}_a}^{5\%}$ values for $a = 1$ and $a = 9$. Moreover, at the 50% CDF level, the VS-eICIC has completely avoided the performance loss incurred due to VS activation at $a = 4$ and is able to restore 22% performance as depicted in the plot. In addition, it is worth noting to remember that the presence of the severe interference at $a = 4$ is evident from the resulting high blanking pattern value indicated in Figure 6.12 (b). At $a = 7$ the performance at all throughput CDF percentile levels have not been impacted at all, therefore, this justifies that it is reasonable to maintain the blanking pattern as minimum as possible to prevent

undesirable impacts. Furthermore, it has been discussed in the VS SINR model and interference analysis that UEs which have high SINR performance during VS=OFF are more sensitive for VS activation and their impact on the system performance is reflected at the higher percentiles of the throughput CDF. As a consequence, the values of $\text{TP}_{\mathcal{A}_a}^{80\%}$ are compared with and without VS-eICIC. It can be clearly observed that, indeed, the $\text{TP}_{\mathcal{A}_a}^{80\%}$ performances are suffering from interference problem at all sites and negative performance gains up to -18% are reported in Figure 6.13. When VS-eICIC is enabled, however, all those negative gains have disappeared at all and even additional gains have been recorded in some cases. This clearly demonstrates that the VS-eICIC is able to address and resolve the interference problem. Finally, the trade-offs of the transmission muting to enable the interference coordination is expected to be reflected on the average performance of the UE throughout, $\text{TP}_{\mathcal{A}_a}^{\text{avg}}$. Accordingly, a reduction in the average performance is observed almost at all sites but compared to the achieved gains, the reduction level is marginal and acceptable, compare $\text{TP}_{\mathcal{A}_a}^{\text{avg}}$ values in in Figure 6.13.

Based on the presented performance results and analysis, it is evident that the SON enabled VS-eICIC has proved its capability in enhancing the system performance and providing substantial capacity by adaptively coordinating the interference. As demonstrated by a diversified network wide heterogeneous spatial distribution scenario, the SON mechanism developed to automate the coordination scheme has been effectively able to optimize the blanking pattern according to the underlying traffic situations. In conclusion, the SON VS-eICIC addresses and averts the critically limiting interference problem which arises in AAS-enabled vertical sectorization. Moreover, this feature can be integrated as one of the SON features that can be automatically enabled/disabled. In real network where SON is enabled, the adaptive VS-eICIC operation can operate in coordination with other SON functions like SON-AS and the procedure can be carried out in a self-organized manner.

Chapter 7

Impact of Cell Layout Change on Existing Automated Network Operations

7.1   Introduction

The various SON mechanisms developed to automate the complicated tasks of radio network planning and optimization are currently designed to operate in a network wherein the deployment is not changing frequently and the cell layout remain stationary [HSS12]. Mobility Robustness Optimization (MRO) is one of the SON use cases which relies on a cell-pair wise statistical information collected from the network over a sufficient period of time. The collected statistics is considered as valid as long as the coverage size/shape of the cells remain static and the neighbor relationships are maintained [HSS12]. In AAS-driven sectorization, however, the cell layout can be dynamically changed due to the activation/ deactivation of cell-beams triggered by momentary local traffic situation. For instance, the introduction of cells via activation process with a new cell IDs results in a new sets of handover borders altering the existing cell neighbor relationships. Unless those changes are properly accommodated and measures are taken, the cell layout change can impair the operation of various SON mechanisms running in the underlying network.

The impacts of AAS-enabled dynamic sectorizaton on the existing SON functionalities have been discussed by 3GPP within the SI [3GP15b], and a WI have been approved to address related ope issues. Future enhancements that might be required on the existing standardized SON solutions are embodied in the WI to guarantee interoperability within multi-vendor deployment environment [3GP14b]. This entails a detailed study and impact analysis of AAS-sectorization with respect to each particular SON use case as well as identifying the associated issues the resulting cell layout change might cause.

In this chapter, the cell layout change introduced by the automated sectorization is thoroughly investigated by including user mobility aspects and particularly enabling MRO operation to optimize the handover performance. The rest of the chapter is organized as follows. Section 7.2.1 briefly explains the analysis carried out to assess the impact of the cell layout change on the performance of the existing MRO operation. Based on the observations from the provided analysis, coordinated strategies for user mobility handling during the sectorizaiton process are presented in Section 7.3.

7.2 Impact of Cell Layout Change on Mobility Robustness Optimization

7.2.1 Intra-RAT Mobility Robustness Optimization

In this section, the performance of the existing MRO operation with respect to the activation/deactivation process of sectorization is outlined.

MRO is one of the self-optimization features of SON that automatically adjusts mobility related network parameter configurations by autonomously detecting handover related connection failures [HSS12]. Intra-RAT MRO particularly deals with handover related problems occurring between two cells which belong to the same type of Radio Access Technology (RAT), for example, between two LTE cells. The existing MRO operation is based on stationary network deployment assumption where handover error statistics are continuously monitored between cell-pair borders as long as the layout of the cells and their neighbor relationships are not altered. However, while the cell layout is dynamically changing from time to time due to automated sectorization, the existing cell neighbor relationships might keep varying as neighbor cell(s) could emerge/disappear. In such cases, the collected mobility event statistics, MRO instances and counter values associated to the state of the network before the execution of the cell layout change might not be valid any longer for the new cell layout. As a consequence, the performance of the HO parameter optimization operation could be impaired thereby causing unexpected degradation of user experience.

When a new cell with a different cell border or different cell ID is introduced, new sets of measurement report statistics are required. This is due to the fact that the propagation environment with respect to the updated cell layout and the spatial distribution of the underlying user traffic to be served by each cell are modified. Moreover, new MRO instances are defined for the new cell-pairs as well. The subsequent sections examines particularly mobility problems and the performance of MRO by considering VS as a means to introduce cell layout changes. The objective of the investigation is to address the following questions.

- How does the existing MRO perform in different sectorization state?

- What HO offset configuration settings can be reused for quick adaptation of handover parameter after a cell layout is restored?

- How does the MRO statistics collected at specific sectorization state can be handled once cell layout is changed?

7.2.2 Connection Failures and Performance of MRO

This section investigates user handover problems and analyzes mobility related connection failures to evaluate the performance of MRO for different sectorization states.

In MRO, mobility related failure types are classified into different groups in order to be able to precisely identify the root causes of the failures. These different failure types are termed as Too-Late (TL) HO (HO_{TL}), Too-Early (TE) HO (HO_{TE}) and HO to Wrong Cell (WC) (HO_{WC}) [HSS12]. In addition, Ping-Pongs(PPs) which are unnecessary back-and-forth of HO events are also regarded as HO problems as it causes extra signaling overhead in the system and needs to be addressed by MRO. Such failure classification enables MRO to take appropriate action via adjusting the Cell Individual Offset (CIO) values which corresponds to specific HO boundary where mobility failure is detected.

A mobile user can suffer from connection failure (CoF) from its serving cell due to either Radio Link Failure (RLF) caused by poor radio condition or a failure to successfully complete a HO process already initiated which is referred as HO failure (HoF). The statistics of these failures are categorized and used to study user mobility problems and the performance of MRO. The total number of CoF N_{CoF} is described as the sum of the number of HO event failures caused by RLF N_{RLF} and HoF N_{HoF}, i.e. $N_{CoF} = N_{RLF} + N_{HoF}$. Given the number of HO_{TL} events by N_{TL}, and the number of HO_{TE} and HO_{HoF} events as a combination of the count of the corresponding mobility failure events associated to RLF and HoF by $N_{TE(RLF)}$, $N_{TE(HoF)}$, $N_{WC(RLF)}$ and $N_{WC(HoF)}$, respectively, the expressions for N_{RLF} and N_{HoF} become

$$N_{RLF} = N_{TL} + N_{TE(RLF)} + N_{WC(RLF)}$$

(7.1)

$$N_{HoF} = N_{TE(HoF)} + N_{WC(HoF)}.$$

In fact the decisions of MRO are made based on observations of HO events and collection of sufficient statistics at each HO cell-pair, i.e. HO-source and HO-target cells. Hence, MRO convergence depends on the number and behavior of the mobile users crossing a particular cell border where a specific type of mobility problem is dominant.

In this section, the performance of MRO is illustrated by looking at the statistics of the HO events collected from the complete network area in cell-pair wise manner, and the number of all HO events described above in Equation 7.1 represent network-wide statistics. Therefore, the value of N_{CoF} indicates the reduction of the connection failure problems and demonstrates the convergence of MRO over time. Besides to CoF, an

additional performance metric described as mobility failure ratio (MFR) (N_{MFR}) is defined to express N_{CoF} as a fraction of the total attempted HO events that includes the statistics of the successful HOs (HO$_{\text{suc}}$) expressed by N_{suc}, i.e.

$$N_{\text{MFR}} = \frac{N_{\text{CoF}}}{N_{\text{CoF}} + N_{\text{suc}}} \tag{7.2}$$

Simulation based MRO performance evaluation has been carried out to inspect HO event behavior for different cell layout cases. In the simulation, user mobility feature is integrated within the 3GPP regular hexagonal cellular model wherein users moving at low speed arbitrary in random direction and at high speed on street along a defined path direction are considered. The street paths are modeled in such away that UEs cross through different HO boundaries where the radio condition and underlying coverage situation are likely impacted by the activation/deactivation of cells. Since developing the MRO algorithm itself is not within the scope of this thesis, detail information about the employed intra-RAT MRO algorithm are not presented here, please see reference [VWLA11]. Furthermore, the simulation parameters and system description are also provided in Table []. The mobility related connection failures are studied for two different cell layout cases which correspond to a more challenging and worst case scenario assumptions as they employ network-wide setups of VS=OFF and VS=ON sectorization states. The initial handover offset CIO$^{\text{int}}$ values with respect to each source-target cell-pair are set to a default setting, CIO$^{\text{int}}$ = 0 dB, and these values are optimized by MRO overtime by monitoring the local mobility failure events at each cell border during the simulation run.
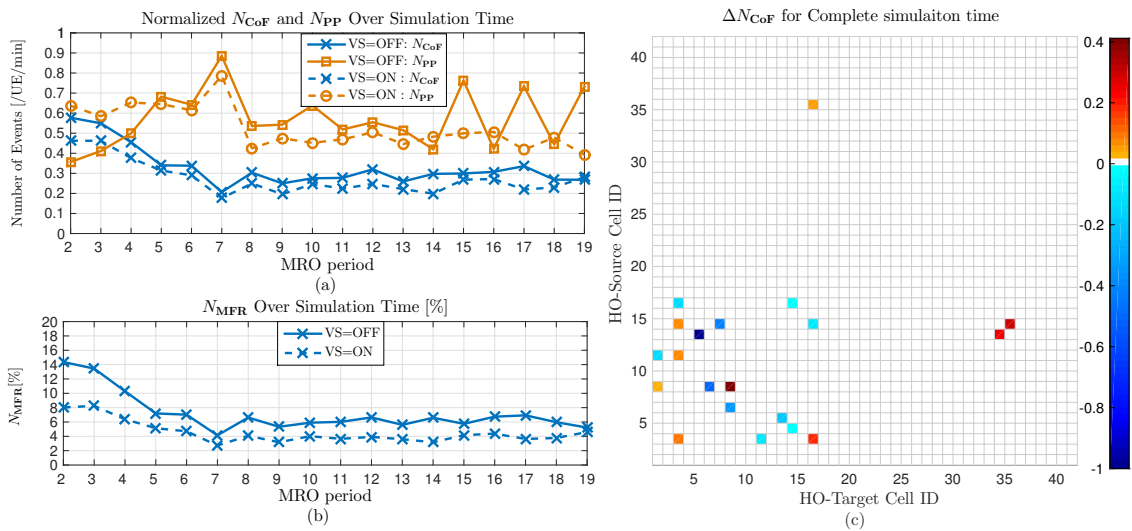

Figure 7.1. (a) Normalized number of MRO events, (b) MFR, (c) ΔN_{CoF} for cell-pair

Figure 7.1 (a) depicts the values of N_{CoF} and N_{PP} normalized to the total number

of UEs within the network and the MRO statistics collection period time in minute for VS=OFF and VS=ON cases. In addition, the corresponding values of N_{MFR} are presented in Figure 7.1 (b). As can be observed in Figure 7.1(a), MRO is able to significantly reduce the failures in both VS=OFF and VS=ON cases by over 60% and their performance stabilizes over time converging to almost same level. Despite the high number of HO events expected when VS=ON due to the increased number handover boundaries introduced by the newly activated inner cells, the total number of mobility failures over the complete network area is lower compared to what is observed when VS=OFF at each MRO period. This is attributed to the evasion of some of the RLF problems occurring during UE handover as a result of better service coverage provided with the denser cell layout with VS=ON. This is demonstrated in Figure 7.1 (b) where N_{MFR} values are substantially improved (lower) for VS=ON due to the higher number of successful HO events, N_{suc}.

The statistics of the network-wide connection failure problems are further investigated for each HO source-target cell-pairs by looking at the difference of the normalized total CoF event counts ΔN_{CoF} collected over the complete simulation time when VS=ON and VS=OFF described by $N_{\text{CoF}}^{\text{ON}}$ and $N_{\text{CoF}}^{\text{OFF}}$, respectively, i.e. $\Delta N_{\text{CoF}} = N_{\text{CoF}}^{\text{ON}} - N_{\text{CoF}}^{\text{OFF}}$. Figure 7.1 (c) illustrates the values of ΔN_{CoF} where the cell ID ranges $[1, 21]$ and $[22, 42]$ corresponds to the outer and inner cells, respectively. For VS=ON, the new additional HO events involve inner-outer and outer-inner cell borders unlike to the only outer-outer cells HO events occurring with VS=OFF. It can be demonstrated in the figure that the mobility problems attributed to the outer-outer cell HO events are significantly reduced when VS=ON over several cell boundaries for aforementioned reason. Despite additional mobility failure counts are recorded, as expected for the new inner-outer/outer-inner cell borders with VS=ON, the overall CoF statistics illustrates that the total number of these failures are lower in comparison to the reduction in the failure rate. Summarizing, the observation from Figure 7.1 evinces the situation where the cell layout change driven by the AAS-based sectorization, in particular to VS, does not always lead to mobility problems as expected. It rather enhances the HO performance by evading the RLF problems as a result of a denser and dominant service coverage by the activation of the inner cells.

Apart from the CoF, the statistics of HO events that lead to PP are evaluated as well and reported in Figure 7.1 to study their behavior with respect to the sectorization. As illustrated in the figure, for VS=OFF, MRO has been able to react on the PP effects, at the initial MRO periods, even faster than the other mobility failures. However, when both HO_{TL} and HO_{TE} problems are dominating, MRO algorithm reacts with higher priority on the cause of those connection failures instead of the PP. Hence, the PP effects are seen oscillating afterwards over time as MRO stops further reacting on

it. This is a trade-offs as both the CoF and PP problems can not be always resolved simultaneously owing to conflicting decisions in adjusting the respective cell border CIO. With the denser cell layout case, VS=ON, since most of the HO_{TL} causing RLF, which have been dominating during VS=OFF, are resolved besides PPs are see to be no longer oscillating as well where their statistics is clearly depicted stabilizing and converging together with the CoF problems.

7.2.3   Connection Failures Triggered by Cell Layout Change

This section examines more practical case scenarios where the network-wide cell layout is changed by activating/deactivating all the inner cells simultaneously while MRO is running.

In reality, cell layout change can be triggered any time and the cell activation/deactivation process might be executed in a network while MRO operation is running. The moment the cell layout change is executed, the collected MRO event statistics and the respective cell border optimized CIO settings can not be representative for the new cell layout. Hence, the MRO statistics might not be valid any longer and the CIO values become sub-optimal. These situations are well investigated, in this section, considering the worst case scenario where the cell activation/deactivation procedure is carried out suddenly while MRO is operating. In this regard, the practically challenging aspect becomes how to deal with the MRO instances and the collected HO event statistics along with the CIO configuration. Two approaches are considered to deal with those challenges. The first approach assumes no additional reaction is need, i.e. MRO statistics and CIO configurations are unchanged. In contrary, the second approach considers to reset the CIO configurations to default settings, $CIO^{int} = 0$ dB, and to restart all the MRO instances and event counter values. Henceforth, the terms NO-RESET and RESET are used to refer to the two approaches, respectively.

Assume VS=OFF state at the beginning and inner cells are activated network-wide at all sites after MRO stabilizes and the statistics of CoF are converged as illustrated in Figure 7.2 where the normalized count of mobility events are reported for both NO-RESET and RESET approaches. In contrast to the stated assumption where the CIO values might yield sub-optimal performance, the NO-RESET approach exhibits no significant additional mobility related issues rather demonstrates a stable MRO performance, see Figure 7.2. With CIO RESET approach, however, the optimized CIO configuration with respect to the handover boundaries of the existing cell borders, i.e., outer-outer cells, are reset. This potentially causes high number of mobility failures

during the next MRO period right after the cell activation, refer to the curve corresponding to CoF statistics in Figure 7.2. Nevertheless, the performance of MRO for both approaches are seen later to converge and stabilize to the same level over time. The PPs statistics are more or less showing not significant deviation from what has been reported previously in Figure 7.1(a). However, marginal variation is observed due to the trade-offs in the MRO response towards the abrupt failures in the network. Investigation of the connection failures right after the activation of the inner cells evinces the dominant mobility failure statistics, in the case of RESET approach, occur between outer-outer cells while relatively less failures are reported for the NO-RESET case.
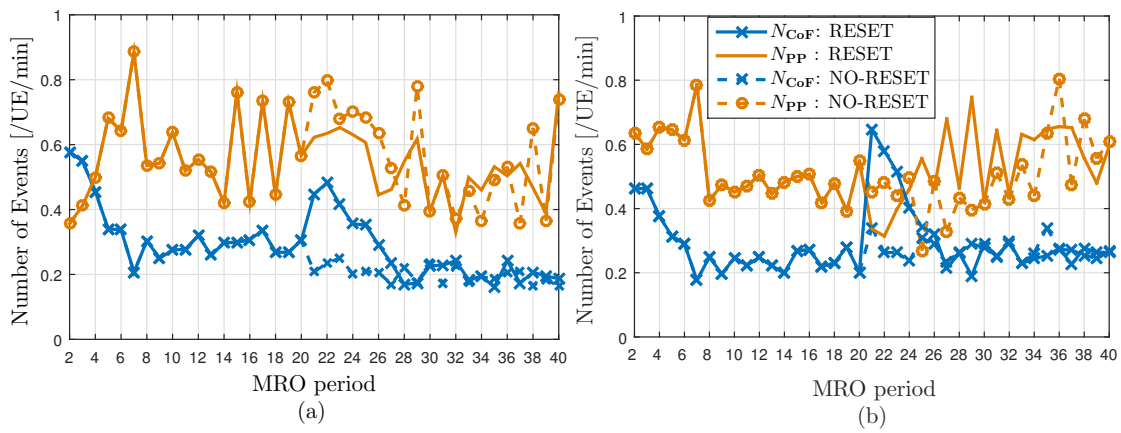
Figure 7.2. Normalized MRO Events (a) Activation, (b) Deactivation

For the deactivation case where the VS cells are merged, all the activated inner cells are turned off while MRO is actively running while in VS=ON state. With such abrupt deactivation procedure, users those have been connected to the respective inner cells are eventually be dropped, hence, suffer from RLF problem. Since the CIO values optimized while VS=ON might not be optimal, additional related handover failures are likely to occur. This explained using Figure 7.2(b) wherein the sectorization is changed from ON to OFF state at MRO period 20 applying either RESET and NO-RESET approaches. As can be observed from the figure, the statistics of COF has dramatically increased after the deactivation of the inner cells for both deactivation approaches for the aforementioned reason. In comparison to NO-RESET, the failure rate is significantly large for the RESET case due to the RLF from all inner cells' users in addition to the mobility failures occur between outer-outer cells as the corresponding optimized CIO configuration is reset to default value. It is worth noting that, the performance of MRO have demonstrated convergence overtime after being able to react and resolve the mobility problems in both RESET and NO-RESET approaches.

The simulative investigation and mobility failure statistical analysis presented so far

have demonstrated that UE mobility related problems can be resolved by the existing MRO and the failures statistics can be significantly reduced and converged over time. However, it is clearly observed that a coordinated action between the MRO and the execution of the cell layout change is essential in order to properly hand-offs users in the underlying coverage to the appropriate serving cells. The required action enables to evade unprecedented connection failure during the transition period, otherwise, many users could experience abrupt connection failures that lead to sudden service disconti- nuity which eventually deteriorate the user experience.

7.2.4 Fast Handover Parameters Reconfiguration

This section discusses a fast handover offset reconfiguration mechanism during cell activation/deactivation procedure in order to address connection failure problems and user service discontinuity caused by a sub-optimal CIO^{int} values.

Depending on how frequent and dynamic the cell activation/deactivation process is executed, relying on the MRO operation to adjust the CIO values can be sub-optimal solution as it might take time until the optimization converges to the optimal value, see Figure 7.2. Unless additional mechanism is applied, the activation/deactivation proce- dure alone can potentially impact the continuity of user services due to an intermittent radio link connection with the serving cell as depicted in Figure 7.1. This section, as a result, introduces a store-and-fetch mechanism where optimized CIO configuration values, CIO_{opt}, are stored along with additional information to describe and identify the cell layout prior to a sectorization state is changed. When the same sectorization or cell layout state is resored CIO_{opt} can be fetched to retrieve back the configura- tion values and adapt the respective cell-pair CIO concurrently with the sectorization action.

For illustration purpose, VS with the two particular sectorization states are assumed to be known as VS=OFF and VS=ON and the respective cell-pair optimal CIO values are described by CIO_{opt}^{OFF} and CIO_{opt}^{ON}, respectively. Each cell is assumed to be able to immediately adapt the MRO parameter (e.g CIO values) when the cell layout is changed via sectorization. When either of the sectorization state is executed for the first time, MRO algorithm runs to optimize the cell-pair CIOs until it finally converges as depicted in Figure 7.1. The corresponding optimal CIO values are then stored along with additional information associated to the respective sectorization state for later retrieval.By the time the same sectorization sate is executed again, these stored optimal CIO values are fetched and reconfigured immediately as initial configuration setting, i.e. $CIO^{int} = CIO_{opt}$.
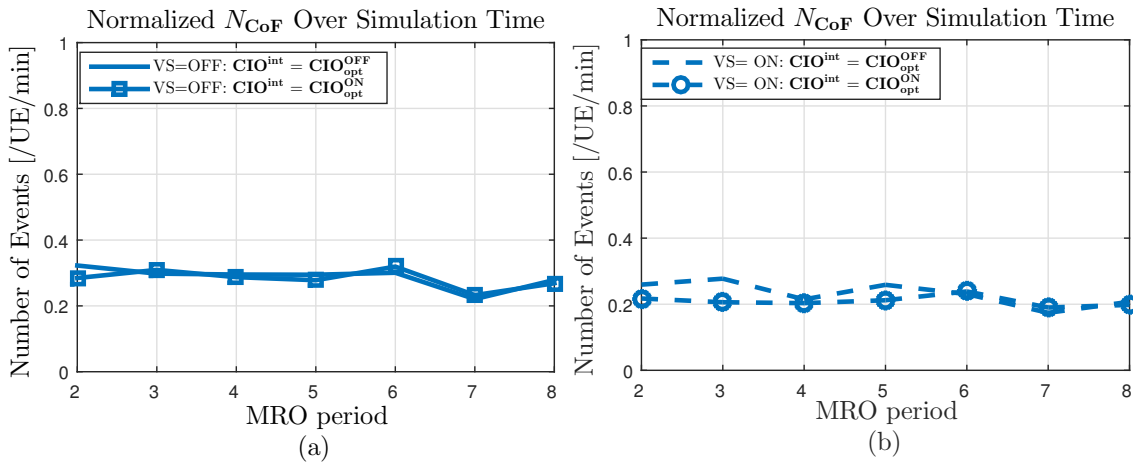
Figure 7.3. Store-and-fetch scheme for faster initial CIO reconfiguration

For each sectorizaiton scenario, in Figure 7.3, different CIO^{int} is utilized from previously optimized CIO. In both VS=OFF and VS=ON cases, the configured CIO^{int} provide a stable MRO performance where the connection failure rates remain at the value depicted in Figure 7.1. Irrespective of which initial value is set, CIO_{opt}^{OFF} or CIO_{opt}^{ON}, the performance curve have demonstrated the same behavior depicting no significant additional mobility failures. These results indicate that, unless additional cell layout change is further introduced, the store-and-fetch scheme is a viable solution for fast reconfiguration of CIO^{int}. The proposed scheme enables to sustain the performance of MRO by evading unforeseen failure of UE connection immediately after sectorizaiton procedure is executed.

7.3   Coordinated Strategies for Dynamic Cell Layout Change

7.3.1   Handling User Mobility During Sectorization

This section discusses user mobility handling mechanisms to address abrupt connection failure problems occurring during the sectorization procedure and which can not be tackled by MRO.

One of the challenging aspects of AAS-based sectorization procedure is the abrupt user connection failures and service discontinuity occurring while the underlying coverage layout is being changed. Concurrent with the activation/deactivation of new cell(s),

considerable number of UEs might need to be handed over to a HO target cell within the new cell layout. Since the existing HO procedure is designed to hand-off UEs through a step-wise and controllable process, transferring a mass number of UEs simultaneously might eventually be unsuccessful, for instance, due to Random Access Channel (RACH) congestion [HT11]. Furthermore, many UEs could suffer from immediate RLF problem during cell deactivation if the UEs' serving cell suddenly disappears. Those connection failure problems are not related to UE mobility itself rather they are attributed to the alteration of the cell layout, hence, can not be resolved by MRO. This motivates the need for additional coordinated mechanism to properly handle the HO of group of UEs to ensure seamless operation of the sectorization process.

In fact, the context of all UEs being served by the same AAS are available at the corresponding eNB irrespective of the employed type of sectorization. These information can be utilized to further coordinate the HO process. Besides, the spatial location of the UEs can be assumed to remain momentarily stationary when the the underlying cell layout is changing. Thus, the available timing advance information of each UE with respect to any of the cell associated to the same AAS used to synchronize data transmission remains valid during the sectorization process. This avoids the need for a new RACH procedure to be performed every time the activation/deactivation action takes place to align the down/up link channel of UEs with respect to a new serving cell. Moreover, a planned cell layout change and associated cell information (cell-info) are known a priori by the respective eNB, therefore, the UEs within the underlying coverage can be pre-configured and prepared in advance so that handing over the UEs can be handled concurrently with the cell activation/deactivation process.

A user hand-off mechanism that can be processed synchronously for a group of UEs without performing the normal HO procedure and free of a new RACH request is proposed as a solution. With the RACH-free approach, the group HO can be executed faster to immediately synchronize UEs with respect to the new cell layout thereby evading unforeseen connection failures. The RACH-free group HO operation is summarized and illustrated with a diagram in Figure 7.4 which depicts the major message flow and the coordination functionalities. When an eNB decides to activate/deactivate a cell, it configures the UEs residing within the coverage area it serves via broadcasting configuration update messages. The broadcast message includes relevant informations about the new cell, e.g. Cell ID to be assigned and CIO$^{\text{int}}$ that should be used for triggering measurement reports. Based on collected measurement reports, the association of the UEs to the respective best target cell is prepared at the eNB without additional procedure because both the source and the possible target cells belongs to the same eNB. The configuration of the UEs is updated with additional mobility control-info to prepare them for a timely synchronized group (synch-group) HO. Finally, the eNB

grants physical resources for the handed over UEs, e.g. Physical Downlink Control Channel (PDCCH) for the UEs, and sends out the synchronization signal immediately after the HO is completed.
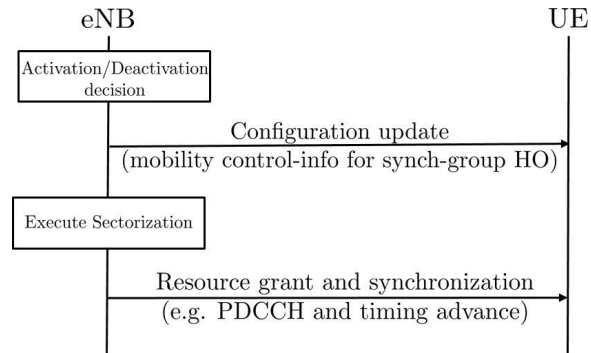
Figure 7.4. RACH-free synch-group HO in AAS-based dynamic sectorization

The presented RACH-free sync-group HO procedure enables not only to combat the connection failure problems but also provides a standardizable solution. The solution considers real network deployment aspects where AAS-enabled dynamic sectorization process is running to further ensure interoperability within vendor specific devices to address some of the related open issues discussed within the 3GPP WI [3GP14b]. Details of the proposed scheme have been contributed for discussion in the WI and the inventive concepts are filed and disclosed in [KW15].

7.3.2   Inter-eNB Notification and Information Exchange

In this section, a coordination scheme is proposed to handle the HO of an incoming/outgoing UEs to/from neighboring cells to avoid UE connection failures.

Despite the fact that the sectorization process is designed to be autonomously executed by an eNB to alter only the local coverage layout, UEs coming from/ going outwards to neighbor coverage region might be impacted by unforeseen connection failures. Moving UEs crossing an area undergoing the cell layout change could initiate a normal HO procedure targeting unstable cell that might be changed in awhile. Unless additional coordination mechanism is employed between the inter-site eNBs, those UEs might be admitted while the target cell information is changed before initiating the RACH procedure. Thus, the incoming UEs may experience a HOF or RLF and such problem can not be tackled by MRO. Furthermore, re-establishing the UEs' connection to the same target cell or any other cell found via cell search after the connection failure might

not be successfully carried out as the required cell information might not be available. This demands preparation of the UEs in advance with respect to possible target cells and configure them with the new cell lay out information.

Dealing with such connection failure issues, this section provides a synchronization scheme which relies on an inter-eNB signaling through which cell layout change information is communicated. The information can be pre- or post-notification messages that are exchanged before or after the execution of sectorization. If pre-notification message is used, the eNB planning the sectorization process informs the neighbor cells' eNBs about the upcoming cell layout change. The message includes informations like the cell-ID(s), the timing required to synchronize ongoing related activities and further instructions on how to handle any HO requests during the transition period. With the post-notification, any HO request from a neighbor eNB serving an incoming UEs can be handled in two ways. The first approach deals with re-direction of the HO request to another possible stable cell if the requested HO target cell is about to be changed. The second approach includes preparation the HO of such UE to multiple cells and synchronizing its action in time with the sectorization.
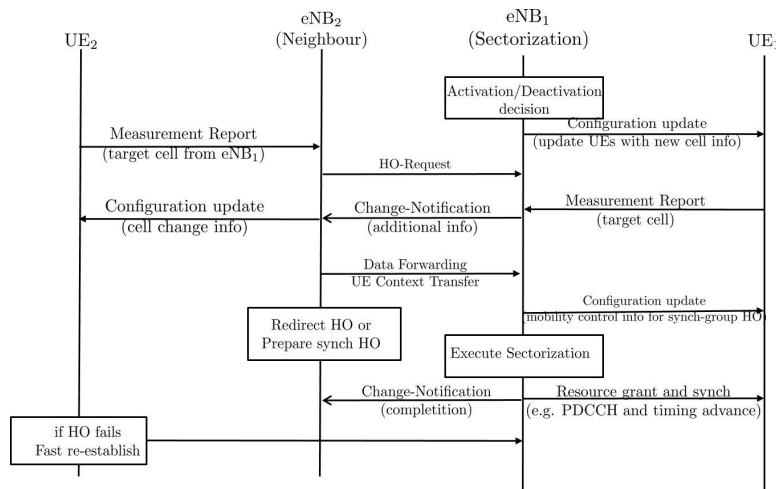
Figure 7.5. Coordination with inter-eNB notification and information exchange

A generic message flow diagram is used in Figure 7.5 to illustrate the information exchange in a typical post-notification case proposed to enable the coordination of the user mobility to handle aforementioned connection failures. The sectorization process is carried out at eNB_1 and the eNB of a neighbor cell serving moving UE UE_2 is denoted by eNB_2. When a normal HO request is sent to eNB_1, a cell layout notification message is replied back to eNB_2 indicating the status of the requested HO target cell. In the HO request reply, additional information (additional-info) and further instructions on how

to proceed with the HO process are included. The coordination scheme proposes first to redirect the requested HO target to any other possible target cell, for example, the second strongest HO target cell measured by the UE. In case the HO redirection is not possible or might not be successful, a fast connection re-establishment option is enabled by preparing the UE HO in advance with respect to multiple HO target cells. This is carried out by updating the configuration of the UEs with the additional-info about the ongoing cell change including the relevant configuration data. The diagram in Figure 7.5 describes only the general inter-eNB message exchange relevant to discuss in this section and to illustrate the intended coordination mechanism. The detail signaling of the coordination procedures developed by the author of the thesis is available and have been disclosed in a filed patent [WKKR17].

In this chapter, the impacts of the cell layout change introduced by AAS-enabled dynamic sectorization have been investigated thoroughly. The investigation mainly analyzes the impacts with respect to user mobility. Detail assessment have been carried out as well on the performance of the existing standardized automated MRO operation to identify any HO related problems and open issues that needs to be addressed to support the AAS-sectorization. The study has indicated that the AAS-sectorization process should be synchronized properly with other SON functionalities like MRO to provide a coordinated network operation. Simulative results have demonstrated that the initial handover offset configurations are crucial in evading some of the UE mobility related failures at the time of cell activation/deactivation process. This has been addressed by a store-and-fetch method that quickly adapt the handover offset configurations with previously optimized values thereby considerably reducing the failures attributed to sub-optimal CIO configurations. UE mobility handling schemes and HO coordination strategies have been proposed to address the abrupt connection failure problems experienced by UEs while sectorization is executed. The proposed schemes and strategies provides a solution to address the related open issues highlighted by 3GPP in response to the request for a potential SON enhancements that may be necessary to ensure interoperability within the existing features in Rel.12

Chapter 8

Summary and Outlook

This thesis deals with adaptive cellular layout enabled by an automated cell sectorization in a self-organizing networks. The developed SON algorithm controls the activation/deactivation of cell-beams to effectively meet dynamic network capacity demand by intelligently monitoring the spatial traffic concentrations and adapting the underlying cell coverage layout accordingly. Moreover, an adaptive enhanced inter-cell interference coordination scheme is developed to combat the inter-cell interference challenge between the co-channel operated cells. The scheme adaptively coordinates the data transmission between the co-sited cells by identifying the users which are severely impacted by the interference. The proposed SON-based cell sectorization automation mechanism provides a flexible and efficient deployment solution over the traditional fixed sectorization paradigm by properly executing the sectorization procedure only when and where it is needed, and can provide gain.

To exploit the AAS-sectorization flexibility in the elevation domain, a three-dimensional channel characterization is vital. In Chapter 3, a new tilt-dependent shadowing model is developed to address the deficiency of the existing shadowing model that considers the propagation scatter behavior only in the azimuth direction. The model characterizes the effect of the elevation domain clutter variation with respect to tilt configuration. A detailed statistical analysis is provided on tilt-specific shadowing values extracted from a ray-tracing based predicted radio propagation data that are able to reflect various clutter experience of the real-world propagation environment. The modeling considers specific scenario configuration consisting of irregular site layout and location adopted from real network planning data. The proposed model estimates a new shadowing value for a new tilt setting by including the expected shadowing variation and the desirable statistical correlation behavior compared to the reference setting. The observed performance results and statistical distribution curves have demonstrated that the proposed model is able to capture the impact of the tilt change. Being derived based on a scenario having a diversified clutter, the proposed model and the introduced variable values can be seen as valid and applicable to a wide range of case scenarios.

The system model developed for the AAS-based sectorization are presented in Chapter 4 and 5. The models are employed to carry out detail investigation on the factors which determine the sectorization performance. The sectorization models describe the complex relationship among various related system parameters to provide a basis criteria

to be used within the automated operation designed to control the sectorization procedure. Simulative based performance analysis have demonstrated the achievable gains from sectorization with respect to different specific scenarios. Accordingly, different case scenarios have been identified where and when the AAS-sectorization can bring the desirable benefit. In addition, thorough analysis has been carried out to study the resulting inter-cell interference impact that countermands the performance of AAS sectorization. To address the inter-cell interference issue, Chapter 4 provides analytical model for the proposed interference-coordination technique and the mathematical framework to be used while developing the corresponding SON mechanism.

The SON framework designed to automate the AAS-sectorization is presented in Chapter 6. The automation mechanism that mainly controls the sectorization-driven cell layout changes performs based on real time performance monitoring. Cell beam activation and deactivation procedures are triggered when the defined cell load criteria are satisfied. The performance of the proposed automation framework has been evaluated using system level simulations considering various non-homogeneous user distribution scenario in the hexagonal-cellular model. Simulation results have clearly demonstrated that the proposed scheme is able to control the activation/deactivation process thereby providing a substantial performance gain over the static over-provisioning approach where the sectorization is always activated. Further performance analysis of the automated sectorization has been carried out in a more realistic RT-scenario wherein the users are spatially distributed in a diversified manner to reflect practical situations. Chapter 6 also provides the adaptive interference-coordination technique that has been developed to tackle the impact of the co-channel interference between co-sited cells. The SON mechanism developed for the interference coordination is responsible for adapting the blanking pattern configuration. Simulation results have demonstrated that the technique is able to adapt the transmission muting pattern thereby effectively dealing with the co-channel interference problem and delivering an optimized system performance.

The impacts of the AAS-enabled dynamic sectorization on the existing SON operations is analyzed in Chapter 7. In particular, mobility related user connection failure problems and handover behavior are investigated in combination with the dynamic cell layout change mechanism. The chapter has focused on a detailed performance assessment on the existing standardized MRO operation and identifying open issues that has to be addressed within future release. The chapter proposes user mobility handling schemes and HO coordination strategies to evade unforeseen abrupt connection failure problems triggered by the cell layout change. The result analysis and proposed concepts have impacted AAS-based related work item and have contributed in the standardization work.

As a future work, the dynamic beam forming and steering capability supported by AAS can be further exploited by developing an automated sectorization that can steer cell beams in any sectorizaiton plane. The user- or group of user-specific beam steering could be more effective in distributing system capacity according to the actual traffic mix. To support such feature, a fully automated beam steering mechanism can be designed to track a specific group or user to deliver a desired service with the promised quality targets. The next-generation massive-array AAS entails further study to foresee a new dimension within the upcoming ultra-dense cellular deployment options to support the proliferation of wireless devices in future networks.

List of Acronyms

2D	2 Dimension
3D	3 Dimension
3GPP	3rd Generation Partnership Project
AAS	Active Antenna Systems
ABS	Almost Blanked Subframe
AC	Available Capacity
ACM	Adaptive Coding and Modulation
AS	Automated Sectorization
BA	Backward Attenuation
BBU	Base Band Unit
BEP	Bit Error Probability
BS	Base Station
CDF	Commutative Density Function
CIO	Cell Individual Offset
CoF	Connection Failure
CP	Cyclic Prefix
CRS	Common Reference Signal
dB	decibel
dBi	decibel relative to isotropic antenna
DPM	Dominant Path Model
eICIC	enhanced Inter Cell Interference Coordination
eNB	enhanced Node B
HO	Handover
HoF	Handover Failure

HO-TE	Handover-Too Early
HO-TL	Handover-Too Late
HO-WC	Handover-to Wrong Cell
HPBW	Half Power Beam Width
HS	Horizontal Sectorization
ISD	Inter Site Distance
LOS	Line Of Sight
LTE	Long Term Evolution
LTE-A	Long Term Evolution-Advanced
MFR	Mobility Failure Ratio
ML	Main Lobe
MRO	Mobility Robustness Optimization
MVB	Minimum Variance Beamformer
NLOS	Non Line Of Sight
NS-UE	Non Sensitive-User Equipment
OAM	Operation And Maintenance
OFDM	Orthogonal Frequency Division Multiplexing
OPEX	Operational Expenditure
PCI	Physical Cell ID
PDCCH	Physical Downlink Control Channel
PF	Proportional Fair
PL	Path Loss
PP	Ping Pong
PRB	Physical Resource Block
RACH	Random Access Channel

RAN	Radio Access Network
RAT	Radio Access Technology
RE	Resource Element
RET	Remote Electrical Tilting
RF	Radio Frequency
RLF	Radio Link Failure
RRH	Remote Radio Head
RS	Reference Signal
RSRP	Received Reference Signal Power
RT	Ray Tracing
SDM	Space Division Multiplexing
SINR	Signal to Interference plus Noise Ratio
SL	Side Lobe
SLL	Side Lobe Level
SON	Self Optimizing Network
SON-AS	Self Optimizing Network function for Automated Sectorization
S-UE	Sensitive-Use Equipment
TRX	Transmitter
TTI	Transmission Time Interval
UE	User Equipment
VS	Vertical Sectorization
VS-eICIC	eICIC for Vertical Sectorization
VS-OFF	Vertical Sectorization-enhanced Inter Cell Interference Coordination
VS-ON	Vertical Sectorization-ON

VS-S   Vertical Sectorization-Supercell

WC   Wrong Cell

WG   Working Group

List of Symbols

a	Index of sector-antenna
$A(c)$	A mapping function returns index of a sector-antenna serving cell c
$\mathcal{A}_a$	Set of users in a coverage area served by sector-antenna index a
$\mathcal{A}_\mathrm{P}$	Set of propagation prediction pixel points
$\alpha_{a,c}$	Fraction of power assigned to cell c from a sector-antenna a
b_a	Index of cell beam generated from sector-antenna a
BA_o	Backward attenuation factor
B_c	beam pattern of cell c
B_c^v	Vertical component of beam pattern of cell c in linear scale
B_c^h	Horizontal component of beam pattern of cell c in linear scale
$\widehat{B_c^\mathrm{h}}$	Vertical component of beam pattern of cell c in decible scale
$\widehat{B_c^\mathrm{v}}$	Horizontal component of beam pattern of cell c in decible scale
B-subframe	Bad SINR subframe
β_c	Transmission blanking pattern
β^step	Transmission blanking pattern adapt step size
β_int	Initial Transmission blanking pattern configuration
c	index of a cell
$\mathcal{C}$	Set of index of all cells
$d_{c,u}$	Path loss distance between user index u and cell c
d_cor	Shadowing decorrelation distance
d_Inner	Geometrical distance of Inner/Outer cell border in vertical sectorization
Δ_a	Utility difference value at sector-antenna a
η_u	Throughput gain of user u after sectorization compared to conventional sectorization
f_PL	PDF of $\widehat{L_\mathrm{T}^u}$
$F_\rho(\Delta\Theta_c^x)$	Shadowing correlation coefficient estimate function for $\Delta\Theta_c^x$
G_c^max	Maximum antenna gain in the boresight direction
G_c^u	Direction antenna gain of cell c in the direction of user u in linear scale
G-subframe	Good SINR subframe
$\widehat{G_c^u}$	Directional antenna gain of cell c in the direction of user u in dB scale
$\widehat{G_{c2,c1}^u}$	Difference of the antenna gain of cell c2 and cell c1 at user u
$\Gamma_\mathrm{opt}^\mathrm{Thr}$	Optimal sensitivity threshold for user grouping
Γ_u^a	Sensitivity of user u served by a cell from sector-antenna a

$\hat{\Gamma}_c$	Average sensitivity value of the sensitivity of all users served by cell c
γ_u	SINR of user u before sectorization
γ'_u	SINR of user u after sectorization
$\gamma'_{u(\text{VS-S})}$	SINR of user u after Super-cell sectorization
h_c^u	Total antenna propagation attenuation value
$\mathcal{H}_c$	Set of values of h_c^u of all users in the network area with respect to cell c
I_{ISD}	Site intersite distance
$\mathbb{I}'_u$	Total interference signal power received at u after sectorization
$\kappa_{c2,c1}^u$	Ratio of the power received from c2 to c1
$\kappa_{c2,c1(\text{VS-S})}^u$	Ratio of the power received from c2 to c1 with vertical sectorization
ϕ_c^u	azimuth angle of user u with respect to cell c
$\Phi_{3\text{dB}}^c$	Azimuth HPBW of cell c
Φ_c	Azimuth orientation of cell c
ϕ_c^{ML}	Azimuth angle in the main lobe region of beam pattern of cell c
Φ_c^{ML}	Set of azimuth angle in the main lobe region of beam pattern of cell c
Φ_{HS}	Azimuth angle of the overlap angle of the horizontal beams in HS
θ_c^u	Elevation angle of user u with respect to cell c
Θ_c	Elevation tilt of beam of cell c
$\Theta_{3\text{dB}}^c$	Elevation HPBW of cell c
Θ_c^o	Reference elevation tilt setting of cell c
θ_c^{ML}	Elevation angle in the main lobe region of beam pattern of cell c
Θ_{VS}	Elevation angle of the overlap angle of the vertical beams in VS
$\Delta\Theta_c^x$	Difference of elevation tilt configuration values
ϑ_c	Set of elevation angle settings of cell c
l_a	Sectorization state at sector-antenna a
L_{T}^u	total propagation loss value in linear scale
$\widehat{L_{\text{T}}^u}$	total propagation loss value in dB scale
$\mathcal{L}_c$	Average load of cell c
$\hat{\Lambda}_c(t)$	Instantaneous load of cell c at time t
Λ_c^{peak}	Configured peak load cell c
Λ^{thr}	Overload triggering threshold of cell c
Λ^{hys}	Load hysteresis at cell c
λ_a	ratio of the number of users connected either of cell at a after sectorization
μ_{s}	Vector of ones

μ_{s}	Vector of ones
$\mu_{\mathrm{S}}^{\mathrm{G}}$	Total radio resource share assigned from G-subframe to sensitive user group
$\mu_{\mathrm{NS}}^{\mathrm{G}}$	Total radio resource share assigned from G-subframe to non-sensitive user group
$\mu_{\mathrm{S}}^{\mathrm{B}}$	Total radio resource share assigned from B-subframe to sensitive user group
$\mu_{\mathrm{NS}}^{\mathrm{B}}$	Total radio resource share assigned from B-subframe to non-sensitive user group
$\tilde{\nu}$	Radiation pattern of array element
N_{Y}	Size of array element in Y direction
N_{Z}	Size of array element in Z direction
N_a	Total number of total number of cells in the network
N_{bs}	Total number of base station sites in the network
$\mathcal{N}_{\mathrm{bs}}$	Set of index of base station sites
N_{ML}	Total number of sample angle of main lobe
N_{SL}	Total number of sample angle of side lobe
Ω	Total system bandwidth
Ω_{PRB}	bandwidth of PRB
Ω_{eff}	Bandwith efficiency
$\mathbb{P}_q$	Position vector of site q
$\mathbb{P}_u$	Position vector of user u
P_c^{tx}	Total transmit power of cell c
P_{N}	Thermal noise power
ψ^u	Sum of extra interference power received at u from new activated cells
q	Base station site index
$Q(c)$	Mapping function returning site of cell c
$\mathcal{Q}_{\mathrm{bs}}$	Set of index of base stations
$\mathcal{R}_{\mathrm{S}}$	Shadowing spatial autocorrelation function
$\mathcal{R}_c$	Resource allocation set of cell c
R_u	Fraction of assigned resource to u before sectorization
R'_u	Fraction of assigned resource to u after sectorization
$RSRP_c^u$	Average RSRP of cell c received at u
$R'^{\mathrm{G}}_{u,\mathrm{NS}}$	Resource share assigned to u from G-subframe if categorized as non-sensitive
$R'^{\mathrm{B}}_{u,\mathrm{NS}}$	Resource share assigned to u from B-subframe if categorized as non-sensitive

$\rho^{\Theta_c^x, \Theta_c^o}$	Correlation coefficient of shadowing values at Θ_c^x and Θ_c^o
$s(u)$	A connection function reruns index of serving cell of u
S_u^c	Tilt dependent shadowing value with respect to user u and cell c in linear domain
$\widehat{S_c^u}$	Tilt independent shadowing value of cell c and user u in dB scale
$S_u^c(\Theta_c)$	Tilt dependent shadowing value with respect to user u and cell c in linear domain
$\widehat{S_c^u}(\Theta_c)$	Tilt dependent shadowing value of cell c and user u in dB scale
$\widehat{S_c^u}(\Theta_c^x)$	Difference of shadowing value of cell c and user u for tilt change in dB scale
SLA_o	Side lobe attenuation factor
$\mathcal{S}^c$	Set of shadowing values of cell c from all user location,(shadow map)
σ_s	Shadowing standard deviation
$\Delta\widehat{S_c^u}(\Theta_c^x)$	Change in the value of shadowing values with $\Delta\Theta_c^x$
$\sigma_{\Delta s}(\Delta\Theta_c^x)$	Standard deviation of values of $\Delta\widehat{S_c^u}(\Theta_c^x)$
$\underline{\sigma}_{\Delta s}$	Standard deviation of shadowing values extracted from ray tracing scenario
t_{ABS}	Time interval to adapt Transmission blanking pattern
$\mathcal{T}_{\mathcal{A}}$	Set of user throughput values collected from coverage area $\mathcal{A}$
$TP_{\mathcal{A}}^{\varpi\%}$	Throughput value at ϖ of CDF percent of statistics collected from coverage area $\mathcal{A}$
$TP_{\mathcal{A}}^{avg}$	Average throughput value of statistics collected from coverage area $\mathcal{A}$
$TP_{\mathcal{A}}^{HM}$	Harmonic average of throughput statistics collected from coverage area $\mathcal{A}$
Υ	Path loss offset
ϱ	Path loss exponent
$U_{(c)}$	Sum log throughput utility of cell c
β^{++}	Increment Transmission blanking pattern
$\tilde{V}_i$	Elevation component of the element response of antenna of index i
$\tilde{V}_k$	azimuth component of the element response of antenna of index k
$V_{k,i}$	Total element response antenna of with index (k,i)
$\mathbf{V}_{ML}^{v}$	matrix of array response vector of main lobe in elevation plane
$\mathbf{V}_{SL}^{(v)}$	Matrix of array response vector of side lobe in elevation plane
$\mathbf{V}_{ML}^{h}$	matrix of array response vector of main lobe in azimuth plane
$\mathbf{V}_{SL}^{(h)}$	Matrix of array response vector of side lobe in azimuth plane
$\mathbf{V}^{h}$	matrix of array response vector of antenna array in azimuth plane
$\mathbf{V}^{v}$	matrix of array response vector of antenna array in elevation plane

$w_{k,i}$	3D Beam forming weight applied to an array element at (k,i)
$\widetilde{w}_i$	Azimuth plane component of $w_{k,i}$
$\widetilde{w}_k$	Elevation plane component of $w_{k,i}$
$\mathbf{W}_c$	3D beamforming weight vector to create beam of cell c
$\mathbf{W}_c^{\mathrm{h}}$	Azimuth plane component of $\mathbf{W}_c$
$\mathbf{W}_c^{\mathrm{v}}$	Elevation plane component of $\mathbf{W}_c$
χ_u	User-specific component of the random shadowing value
χ_q	Site-specific component of the random shadowing value

List of Own Publications

[GKW+14] A. A. Gebremariam, D. W. Kifle, B. Wegmann, I. Viering, and F. Granelli, "Techniques of candidate cell selection for antenna tilt adaptation in LTE-advanced," in *20th European Wireless Conference European Wireless*, 2014.

[KFW+15] D. W. Kifle, F.B.Tesema, B. Wegmann, I. Viering, and A. Klein, "Enhancing vertical sectorization performance with eICIC in AAS based LTE-a deployment," in *IEEE 82nd Vehicular Technology Conference VTC Fall*, 2015.

[KGW+14] D. W. Kifle, L. C. Gimenez, B. Wegmann, I. Viering, and A. Klein, "Comparison and extension of existing 3d propagation models with real-world effects based on ray-tracing, a basis for network planning and optimization," *Springer Jounral of Wireless Personal Communications*, 2014.

[KWVK13a] D. W. Kifle, B. Wegmann, I. Viering, and A. Klein, "Impact of antenna tilting on propagation shadowing model," in *IEEE 77th Vehicular Technology Conference VTC Spring*, 2013.

[KWVK13b] ——, "On the potential of traffic driven tilt optimization in LTE-A networks," in *IEEE 24th International Symposium on Personal, Indoor and Mobile Radio Communications: Mobile and Wireless Networks*, 2013.

[KWVK14a] ——, "Mathematical model for vertical sectorization (VS) in AAS based LTE deployment," in *11th International Symposium on Wireless Communications Systems (ISWCS)*,, 2014.

[KWVK14b] ——, "Super-cell from inner sectors of active antenna system (AAS) - vertical sectorization," in *IEEE International Conference on Communications (ICC)*, 2014.

[KWVK15] ——, "Study on impact of vertical sectorization on mobility and existing MRO performance," in *2015 European Conference on Networks and Communications (EuCNC)*,, 2015.

[KWVK16] ——, "Self optimizing network (SON) framework for automated vertical sectorization," in *IEEE 27th International Symposium on Personal, Indoor and Mobile Radio Communications: Mobile and Wireless Networks*, 2016.

[WK15] B. Wegmann and D. W. Kifle, "User handoff mechanism for cell splitting in wireless network," WO 2015139752 A1, 2015.

[WKKR17] B. Wegmann, K.Krysztof, D. W. Kifle, and R.Waldhauser, "Determination of a re-establishment cell," WO2016150478 A1, 2017.

Bibliography

[3D09]   *Modeling of 3D Field Patterns of Downtilted Antennas and Their Impact on Cellular Systems*, 2009.

[3GP12]   3GPP TSG-RAN WG3, "Study on next generation SON for UTRA and LTE:RP-122037," 3GPP, Tech. Rep., 2012.

[3GP13a]   3GPP, "TS36.814 technical specification group radio access network: Evolved universal terrestrial radio access (E-UTRA)," 3GPP, Tech. Rep., 2013.

[3GP13b]   3GPP TSG-RAN WG3, "SON for dynamic deployment changes enabled by AAS:r3-130666," 3GPP, Tech. Rep., 2013.

[3GP14a]   3GPP, "TS36.942 technical specification group radio access network: Evolved universal terrestrial radio access (E-UTRA);," 3GPP, Tech. Rep., 2014.

[3GP14b]   3GPP TSG RAN, "SON for AAS-based deployments," 3GPP, Tech. Rep., 2014.

[3GP15a]   3GPP, "Technical specification group radio access network:evolved universal terrestrial radio access (E-UTRA) and evolved universal terrestrial radio access network (E-UTRAN)," 3GPP, Tech. Rep., 2015.

[3GP15b]   3GPP, "TR37.822 technical specification group radio access network: Study on next generation self-optimizing network (SON) for UTRAN and E-UTRAN," Tech. Rep., 2015.

[3GP10]   ——, "Lte; evolved universal terrestrial radio access network (E-UTRAN); self-configuring and self-optimizing network (son) use case and solution," 3GPP, Tech. Rep., 210.

[ADG⁺96]   S. Ariyavisitakul, T. Darcie, L. Greenstein, M. R. Phillips, and N. K. Shankaranarayanan, "Performance of simulcast wireless techniques for personal communication systems," *IEEE Journal on Selected Areas in Communications*, 1996.

[Ame11]   G. Americas. (2011) Self-optimizing networks-The benefits of SON in LTE. [Online]. Available: http://www.4gamericas.org/

[Aut16]   U. Author, "Active antennas: The next step in radio and ... - comm-scope.com," *Unknown Journal*, 2016.

[AWNO⁺12] P. Ameigeiras, Y. Wang, J. Navarro-Ortiz, P. E. Mogensen, and J. M. Lopez-Soler1, "Traffic models impact on OFDMA scheduling design," *EURASIP Journal on Wireless Communications and Networking 2*, 2012.

[AZA15a]   A.Tall, Z.Altman, and E. Altman, "Self-optimizing strategies for dynamic vertical sectorization in lte networks," in *IEEE Wireless Communications and Networking Conference (WCNC),*, 2015.

[AZA15b]   ——, "Virtual sectorization: Design and self-optimization," in *IEEE Vehicular Technology Conference (VTC Spring)*, 2015.

[Bal05]   C. A. Balanis, *Antenna Theory: Analysis and Design.*   John WIley and Sons, Inc, 2005.

[Bau14]   P. Baudin, *Wireless Transceiver Architecture: Bridging RF and Digital Communications.*   Wiley, 2014.

[CG03]   X. Cai and G. B. Giannakis, "A two-dimensional channel simulation model for shadowing processes," *IEEE TRANSACTIONS ON VEHICULAR TECHNOLOGY*, 2003.

[Cha92]   G. K. Chan, "Effects of sectorization on the spectrum efficiency of cellular radio systems," *IEEE Transactions on Vehicular Technology, Vol. 41*, 1992.

[CLW$^+$03]   D. Chizhik, J. Ling, P. W. Wolniansky, R. A. Valenzuela, N. Costa, and K. Huber, "Multiple-inputŰmultiple-output measurements and modeling in manhattan," *IEEE JOURNAL ON SELECTED AREAS IN COMMUNICATIONS*, 2003.

[CLW$^+$15]   T. Chapman, E. Larsson, P. Wrycza, E. Dahlman, S. Parkvall, and J. Skold, *HSPA Evolution: The Fundamentals for Mobile Broadband.* ELSEVIER, 2015.

[DMW$^+$11]   A. Damnjanovic, J. Montojo, Y. Wei, T. Ji, T. Luo, M. Vajapeyam, T. Yoo, O. Song, and D. Malladi, "A survey on 3GPP heterogeneous networks," *IEEE Wireless Communications*, 2011.

[E.99]   B. J. E., "Propagation prediction models (building penetration). COST telecommunications," COST Telecom Secretariat, Commission of the European Communities, Tech. Rep., 1999.

[EFL$^+$97]   V. Erceg, S. J. Fortune, J. Ling, A. J. Rustako, and R. A. Valenzuela, "Comparisons of a computer-based propagation prediction tool with experimental data collected in urban microcellular environments," *IEEE JOURNAL ON SELECTED AREAS IN COMMUNICATIONS*, 1997.

[EL00]   E.Huemer and K. Lensing, "Practical antenna guide," KATHREIN, Tech. Rep., 2000.

[FJNC]   K. Fujimoto and J. R. James, *Mobile Antenna Systems Handbook*, 2001 ARTECH HOUSE, INC.

[FWZ$^+$12]   Y. Fu, J. Wang, Z. Zhao, L. Dai, and H. Yang, "Analysis of vertical sectorization for hspa on a system level: Capacity and coverage," in *IEEE Vehicular Technology Conference (VTC Fall)*, 2012.

[G.11]   S. G., *Principles of mobile communication.*   Springer, 2011.

[Gar07]   V. K. Garg, *WIRELESS COMMUNICATIONS and NETWORKING*. Elsevier, 2007.

[GMV01]   R. Giuliano, F. Mazzenga, and F. Vatalaro, "Adaptive cell sectorization for umts third generation cdma systems," in *IEEE VTS 53rd Vehicular Technology Conference, VTC -Spring.*, 2001.

[God01]   L. C. Godara, *Handbook of Antennas in Wireless Communications*. CRC press, 2001.

[God04]   ——, *Smart Antennas*. CRC Press, 2004.

[Hay12]   A. Hayter, *Probability and Statistics for Engineers and Scientists*. CENGAGE Learning, 2012.

[HH15]   S. V. Howard Huang, Constantinos B. Papadias, *MIMO Communication for Cellular Networks*. Springer Science, 2015.

[HKS09]   O. H, K. K, and I. S, "Outdoor-to-Indoor Propagation Loss Prediction in 800-MHz to 8-GHz Band for an Urban Area," *IEEE TRANSACTIONS ON VEHICULAR TECHNOLOGY*, 2009.

[HOD+10]   H. Huang, O.Alrabadi, J. Daly, D. Samardzija, C. Tran, R. Valenzuela, and S. Walker, "Increasing throughput in cellular networks with higher-order sectorization," in *Conference Record of the Forty Fourth Asilomar Conference on Signals, Systems and Computers*, 2010.

[hp09]   X. S. hui and Z. Z. pei, "Coordinated multipoint transmission systems with the clustered super-cell structure configuration," in *5th International Conference on Wireless Communications, Networking and Mobile Computing(WiCom '09.)*, 2009.

[HQ13]   R. Q. Hu and Y. Qian, *Heterogeneous Cellular Networks*. Wiley, 2013.

[HSA98]   M. Ho, G. L. Stuber, and M. D. Austinr, "Performance of switched-beam smart antennas for cellular radio systems," *IEEE Transactions on Vehicular Technology, Vol. 47*, 1998.

[HSKH13]   H. Halbauer, S. Saur, J. Koppenborg, and C. Hoek, "3d beamforming: Performance improvement for cellular networks," *Bell Labs Technical Journal*, 2013.

[HSS12]   S. Hämälänen, H. Sanneck, and C. Sartori, *LTE Self-Organizing Networks (SON)*. Wiley, 2012.

[HT09]   H. Holma and A. Toskala, *LTE for UMTS - OFDMA and SC-FDMA Based Radio Access*. Wiley and Sons Ltd, 2009.

[HT11]   ——, *LTE for UMTS: Evolution to LTE-Advanced*. John Wiley and Sons, Ltd, 2011.

[HT12]   ——, *LTE Advanced: 3GPP Solution for IMT-Advanced*. Wiley, 2012.

[Hu16]   F. Hu, *Opportunities in 5G Networks: A Research and Development Perspective.* CRC press, 2016.

[HW16]   C. Hoymann and B. Wolz, "Adaptive space-time sectorization for interference reduction in smart antenna enhanced cellular WiMAX networks," *Unknown Journal*, 2016.

[HZ02]   J. M. Holtzman and M. Zorz, *Advances in Wireless Communications.* Kluwer Academic Publishers, 2002.

[J.C05]   J.Capon, "High-resolution frequency-wavenumber spectrum analysis," *IEEE TRANSACTIONS ON SIGNAL PROCESSING*, 2005.

[JL15]   P. S. Jian Li, *Robust Adaptive Beamforming.* John Wiley and Sons, 2015.

[JMB+16]   R. Joyce, D. Morris, S. Brown, D. Vyas, and L. Zhang, "Higher order horizontal sectorization gains for 6, 9, 12 and 15 sectored cell sites in a 3GPP/HSPA+ network," *IEEE Transactions on Vehicular Technology Vol. 65*, 2016.

[KC09]   J. Kelif and M. Coupechoux, "Cell breathing, sectorization and densification in cellular networks," in *7th International Symposium on Modeling and Optimization in Mobile, Ad Hoc, and Wireless Networks*, 2009.

[KFW+15]   D. W. Kifle, F.B.Tesema, B. Wegmann, I. Viering, and A. Klein, "Enhancing vertical sectorization performance with eICIC in AAS based LTE-a deployment," in *IEEE 82nd Vehicular Technology Conference VTC Fall*, 2015.

[KGI+99]   S.-C. Kim, B. J. Guarino, T. M. W. II, V. Erceg, S. J. Fortune, R. A. Valenzuela, L. W. Thomas, J. Ling, and d J. Don Moore, "Radio propagation measurements and prediction using three-dimensional ray tracing in urban environments at 908 mhz and 1.9 ghz," *IEEE TRANSACTIONS ON VEHICULAR TECHNOLOGY*, 1999.

[KGW+14]   D. W. Kifle, L. C. Gimenez, B. Wegmann, I. Viering, and A. Klein, "Comparison and extension of existing 3d propagation models with real-world effects based on ray-tracing, a basis for network planning and optimization," *Springer Jounral of Wireless Personal Communications*, 2014.

[KH05]   H. Kim and Y. Han, "A proportional fair scheduling for multicarrier transmission systems," *IEEE COMMUNICATIONS LETTERS*, 2005.

[KW15]   D. W. Kifle and B. Wegmann, "User handoff mechanism for cell splitting in wireless network," WO 2015139752 A1, 2015.

[KWVK13]   D. W. Kifle, B. Wegmann, I. Viering, and A. Klein, "Impact of antenna tilting on propagation shadowing model," in *IEEE 77th Vehicular Technology Conference VTC Spring*, 2013.

[KWVK14a] ——, "Mathematical model for vertical sectorization (VS) in AAS based LTE deployment," in *11th International Symposium on Wireless Communications Systems (ISWCS),*, 2014.

[KWVK14b] ——, "Super-cell from inner sectors of active antenna system (AAS) - vertical sectorization," in *IEEE International Conference on Communications (ICC)*, 2014.

[KWVK15] ——, "Study on impact of vertical sectorization on mobility and existing MRO performance," in *2015 European Conference on Networks and Communications (EuCNC),*, 2015.

[KWVK16] ——, "Self optimizing network (son) framework for automated vertical sectorization," in *IEEE 27th International Symposium on Personal, Indoor and Mobile Radio Communications: Mobile and Wireless Networks*, 2016.

[LC10] K. Linehan and R. Chandrasekaran, "White paper :active antennas: The next step in radio and antenna evolution," COMMSCOPE, Tech. Rep., 2010.

[LJLL13] Y. Li, X. J, D. Liang, and Y. Li, "Dynamic Beamforming for Three-Dimensional MIMO technique in LTE-Advanced networks," *International Journal of Antennas and Propagation*, 2013.

[LN01] B. Lindmark and M. Nilsson, "On the available diversity gain from different," *IEEE JOURNAL ON SELECTED AREAS IN COMMUNICATIONS*, 2001.

[LOp02] S. H. Lim, S. H. Oh, and J. S. park, "A new adaptive sectorization method to use maximum capacity base station in wireless networks," in *Mobile Communications, Band 7*, 2002.

[LW10] W. Liu and S. Weiss, *Wideband Beamforming: Concepts and Techniques*, 2010.

[M.91] G. M., "Correlation model for shadow fading in mobile radio systems," *Electron. Lett., vol. 27*, 1991.

[Man05] D. G. Manolakis, *Statistical and Adaptive Signal Processing.* Artech House, 2005.

[MHK16] J. D. Matyjas, F. Hu, and S. Kumar, *Wireless Network Performance Enhancement via Directional Antennas.* Tayler and Francis Group, 2016.

[Mis15] A. R. Mishra, *Cellular Technologies for Emerging Markets: 2G, 3G and Beyond.* Wiley, 2015.

[MNK+07] P. Mogensen, W. Na, I. Z. Kovács, F. Frederiksen, A. Pokhariyal, K. I. Pedersen, T. Kolding, K. Hugl, and M. Kuusela, "LTE capacity compared to the shannon bound," *VTC2007-Spring. IEEE 65th Vehicular Technology Conference*, 2007.

[MW99]   V. MADISETTI and D. Williams, *Digital Signal Processing Handbook on CD-ROM*. CRC Press LLC, 1999.

[Net]   N. Networks, "Active antenna systems: A step-change in base station site performance," Nokia Networks, Tech. Rep.

[NPK94]   A. F. Naguib, A. Paulraj, and T. Kailath, "Capacity improvement with base-station antenna arrays in cellular CDMA," *IEEE Transactions on Vehicular Technology (Volume 43)*, 1994.

[RC09]   E. Rodrigues and F. Casadevall, "Resource allocation and packet scheduling in OFDMA-based cellular networks," in *4th International Conference on Cognitive Radio Oriented Wireless Networks and Communications*, 2009.

[Rud83]   A. W. Rudge, *The Handbook of Antenna Design, Band 2*. Peter Peregrinus Ltd, 1983.

[SA00]   M. K. Simon and M. Alouini, *Digital Communication over Fading Channels(A Unified Approach to Performance Analysis)*. JOHN WILEY and SONS INC, 2000.

[SAP99]   A. Sabharwal, D. Avidor, and L. Potter, "Sector beam synthesis for cellular systems using phased antenna arrays," in *IEEE Wireless Communications and Networking Conference*, 1999.

[sem17]   (2017) Self-management for unified heterogeneous radio access networks (semafour). http://fp7-semafour.eu/en/.

[Sin15]   T. L. Singal, *Wireless Communications*. Tata McGraw Hill, 2015.

[SOC08]   SOCRATES. (2008, May) Requirements for self-organizing networks. [Online]. Available: http://www.fp7-socrates.eu

[Sta01]   P. Stavroulaki, *Third Generation Mobile Telecommunication Systems: UMTS and IMT-2000*. Springer, 2001.

[Ste09]   S. Stergiopoulos, *Advanced Signal Processing: Theory and Implementation for Sonar, Radar, and Non-Invasive Medical Diagnostic Systems*. CRC Press, 2009.

[SY01]   C. Saraydar and A. Yener, "Adaptive cell sectorization for CDMA," *IEEE Journal on Selected Areas in Communications*, 2001.

[Tür07]   U. Türke, *Efficient Methods for WCDMA Radio Network Planning and Optimization*. Deutscher Universitätsverlag, 2007.

[TZV$^+$14]   F. B. Tesema, P. Zanier, I. Viering, A. J. Fehske, and G. P. Fettweis, "Simplified scheduler model for SON algorithms of eICIC in heterogeneous networks," in *20th European Wireless Conference; Proceedings of European Wireless*, 2014.

[VDEF⁺15]   E. M. Vitucci, V. Degli-Esposti, F. Fuschini, J. S. Lu, M. Barbiroli, J. N. Wu, M. Zoli, J. J. Zhu, , and H. L. Bertoni, "Ray tracing rf field prediction: An unforgiving validation," *Hindawi International Journal of Antennas and Propagation*, 2015.

[VGL03]   S. A. Vorobyov, A. B. Gershman, and Z.-Q. Luo, "Robust adaptive beamforming using worst-case performance optimization: A solution to the signal mismatch problem," *IEEE TRANSACTIONS ON SIGNAL PROCESSING*, 2003.

[VWLA11]   I. Viering, B. Wegmann, A. Lobinger, and A. Awada, "Mobility robustness optimization beyond doppler effect and WSS assumption," in *International Symposium on Wireless Communication Systems*, 2011.

[Wah11]   R. Wahl, "An introduction to the urban dominant path prediction model," AWE Communications GmbH, Tech. Rep., 2011.

[WJ04]   J. W. Wallace and M. A. Jensen, "Mutual coupling in mimo wireless systems: A rigorous network theory analysis," *IEEE TRANSACTIONS ON WIRELESS COMMUNICATIONS*, 2004.

[WKKR17]   B. Wegmann, K.Krysztof, D. W. Kifle, and R.Waldhauser, "Determination of a re-establishment cell," WO2016150478 A1, 2017.

[WL]   G. Wölfle and F. M. Landstorfer, "Dominant paths for the field strength prediction," *Unknown Journal*.

[WLSSH99]   A. Wacker, J. Laiho-Steffens, K. Sipila, and K. Heiska, "The impact of the base station sectorisation on wcdma radio network performance," in *IEEE VTS 50th Vehicular Technology Conference (VTC - Fall).*, 1999.

[WRPW]   G. Wölfle, R.Wahl, P.Wildbolz, and P. Wertz, "Dominant path prediction model for urban scenarios."

[WSP12]   Y. Wang, B. Soret, and K. I. Pederson, "A 3D performance analysis of enhanced inter-cell interference coordination in LTE-advanced heterogeneous networks," in *IEEE 75th Vehicular Technology Conference (VTC Spring),*, 2012.

[XSKO03]   J. Xhou, S. Sasaki, H. Kikuchi, and Y. Onozato, "Cell boundary shifting with power ratio control and tilted antenna arrays in a cellular communications," *IEEE Transcations Fundamentsls*, 2003.

[YHH09]   O. N. C. Yilmaz, S. Hamalainen, and J. Hamalainen, "System level analysis of vertical sectorization for 3GPP LTE," in *6th International Symposium on Wireless Communication Systems*, 2009.

[YI15]   Z. YUN, , and M. F. ISKANDER, "Ray tracing for radio propagation modeling: Principles and applications," *IEEE Access*, 2015.

[YZXZ14] F. Yang, J. Zhang, W. Xie, and X. Zhu, "Field trial results for vertical sectorization in lte network using active antenna system," in *IEEE International Conference on Communications (ICC)*, 2014.

[Zet04] P. Zetterberg, "Performance of three, six, nine and twelve sector sites in CDMA - based on measurements," in *IEEE Eighth International Symposium on Spread Spectrum Techniques and Applications,*, 2004.

Lebenslauf

Name: Dereje Woldemedhin Kifle

Geburtsdatum: 05.12.1983

Geburtsort: Addis Ababa, Ethiopia

Schulausbildung

1996-1998	Meserete Edget, Addis Ababa, Ethiopia
1998-2002	Kolfe Comprehensive, Addis Ababa, Ethiopia

Studium

2002-2007	Bachelor of Science in Electrical Engineering an der Bahirdar University, Bahirdar, Ethiopia.
2009-2011	Masters of Science in Telecommunications Engineering an der University of Trento, Trento, Italy.

Berufstätigkeit

2011-2016	Wissenschaftliche Tätigkeit in der Radio Systems Forschungsabteilung von Bell labs Nokia Networks in München

Erklärung laut §9 der Promotionsordnung

Ich versichere hiermit, dass ich die vorliegende Dissertation allein und nur unter Verwendung der angegebenen Literatur verfasst habe. Die Arbeit hat bisher noch nicht zu Prüfungszwecken gedient.

Darmstadt, 28. November 2016,